

## REVIEW

### Physics–Dynamics Coupling in Weather, Climate, and Earth System Models: Challenges and Recent Progress

MARKUS GROSS,<sup>a</sup> HUI WAN,<sup>b</sup> PHILIP J. RASCH,<sup>b</sup> PETER M. CALDWELL,<sup>c</sup> DAVID L. WILLIAMSON,<sup>d</sup>  
 DANIEL KLOCKE,<sup>e</sup> CHRISTIANE JABLONOWSKI,<sup>f</sup> DIANA R. THATCHER,<sup>f</sup> NIGEL WOOD,<sup>g</sup> MIKE CULLEN,<sup>g</sup>  
 BOB BEARE,<sup>h</sup> MARTIN WILLET,<sup>g</sup> FLORIAN LEMARIÉ,<sup>i</sup> ERIC BLAYO,<sup>i</sup> SYLVIE MALARDEL,<sup>j</sup>  
 PIET TERMONIA,<sup>k,l</sup> ALMUT GASSMANN,<sup>m</sup> PETER H. LAURITZEN,<sup>d</sup> HANS JOHANSEN,<sup>n</sup>  
 COLIN M. ZARZYCKI,<sup>d</sup> KOICHI SAKAGUCHI,<sup>b</sup> AND RUBY LEUNG<sup>b</sup>

<sup>a</sup> *Departamento de Oceanografía Física, Centro de Investigación Científica y Educación Superior de Ensenada, Ensenada, Baja California, México*

<sup>b</sup> *Pacific Northwest National Laboratory, Richland, Washington*

<sup>c</sup> *Physical and Life Sciences Directorate, Lawrence Livermore National Laboratory, Livermore, California*

<sup>d</sup> *National Center for Atmospheric Research, Boulder, Colorado*

<sup>e</sup> *Hans Ertel Center for Weather Research, Deutscher Wetterdienst, Offenbach, Germany*

<sup>f</sup> *Department of Climate and Space Sciences and Engineering, University of Michigan, Ann Arbor, Michigan*

<sup>g</sup> *Met Office, Exeter, United Kingdom*

<sup>h</sup> *CEMPS, Exeter University, Exeter, United Kingdom*

<sup>i</sup> *INRIA, University of Grenoble–Alpes, LJK, CNRS, Grenoble, France*

<sup>j</sup> *ECMWF, Shinfield Park, Reading, United Kingdom*

<sup>k</sup> *Royal Meteorological Institute of Belgium, Brussels, Belgium*

<sup>l</sup> *Department of Physics and Astronomy, Ghent University, Ghent, Belgium*

<sup>m</sup> *IAP Kühlungsborn, Leibniz–Institut für Atmosphärenphysik e.V. an der Universität Rostock, Kühlungsborn, Germany*

<sup>n</sup> *Applied Numerical Algorithms Group, Lawrence Berkeley National Laboratory, Berkeley, California*

(Manuscript received 14 November 2017, in final form 10 August 2018)

#### ABSTRACT

Numerical weather, climate, or Earth system models involve the coupling of components. At a broad level, these components can be classified as the resolved fluid dynamics, unresolved fluid dynamical aspects (i.e., those represented by physical parameterizations such as subgrid-scale mixing), and nonfluid dynamical aspects such as radiation and microphysical processes. Typically, each component is developed, at least initially, independently. Once development is mature, the components are coupled to deliver a model of the required complexity. The implementation of the coupling can have a significant impact on the model. As the error associated with each component decreases, the errors introduced by the coupling will eventually dominate. Hence, any improvement in one of the components is unlikely to improve the performance of the overall system. The challenges associated with combining the components to create a coherent model are here termed physics–dynamics coupling. The issue goes beyond the coupling between the parameterizations and the resolved fluid dynamics. This paper highlights recent progress and some of the current challenges. It focuses on three objectives: to illustrate the phenomenology of the coupling problem with references to examples in the literature, to show how the problem can be analyzed, and to create awareness of the issue across the disciplines and specializations. The topics addressed are different ways of advancing full models in time, approaches to understanding the role of the coupling and evaluation of approaches, coupling ocean and atmosphere models, thermodynamic compatibility between model components, and emerging issues such as those that arise as model resolutions increase and/or models use variable resolutions.

#### 1. Introduction

Weather, climate, and Earth system models approximate the solutions to sets of equations that describe the relevant physics and chemistry. These equations represent, for example, balances of momentum, energy, and

---

 Denotes content that is immediately available upon publication as open access.

---

*Corresponding author:* Markus Gross, mgross@cicese.mx

DOI: 10.1175/MWR-D-17-0345.1

© 2018 American Meteorological Society. For information regarding reuse of this content and general copyright information, consult the [AMS Copyright Policy \(www.ametsoc.org/PUBSReuseLicenses\)](https://www.ametsoc.org/PUBSReuseLicenses).

mass of the appropriate system. Discrete approximations in space and time to these continuous equations are necessary to solve these equations numerically. Creating a single, coherent, and consistent discretization of an entire system of equations covering the entire range of spatial and temporal scales, even for one component such as the atmosphere, is indeed challenging, if not an impossible task. Even if it is possible, the numerical solution of such a system (spanning all possible scales) is currently beyond the reach of even the most powerful computers. Therefore, the system is separated into components that are discretized mostly independently of each other and then coupled together in some manner. These components can broadly be classified as comprising the resolved fluid dynamical aspects of the atmosphere or the ocean, unresolved fluid dynamical aspects (e.g., those represented by physical parameterizations such as subgrid-scale mixing), and nonfluid dynamical elements such as radiation and microphysical processes.

The challenges associated with bringing together all the various discretized components to create a coherent model will be referred to here as physics–dynamics coupling. The term physics–dynamics coupling has evolved from the fact that the resolved fluid dynamics components are commonly known as the dynamical cores or simply “dynamics,” and the physical parameterizations that represent the unresolved and under-resolved processes and the nonfluid dynamical processes are collectively referred to as “physics.” The weather, climate, and Earth system modeling communities have relatively recently started to make focused efforts on addressing physics–dynamics coupling in the broader sense as a topic by itself (Gross et al. 2016a).

Figure 1a schematically shows the variety of model components and the different aspects of discretizing them in both space and time, as well as the coupling between them. For simplicity, Fig. 1a includes only two component models: the atmosphere and the ocean. However, modeling systems often include a large number of other components, such as land, glacier, sea ice, atmospheric chemistry, and ocean biogeochemistry models. These components are inherently coupled to each other through the momentum, mass, and energy exchanges at their interfaces.

The parameterizations are typically organized by processes: for example, cumulus convection and cloud microphysics in the atmosphere and lateral and vertical mixing in the ocean. Some of these processes are symbolized in Fig. 1a by clip art icons. Processes reside at different locations in the time–space domain. For example, the characteristic time scales associated with cloud microphysics and planetary-scale advection are vastly different. It can also be shown that the model

performance can be improved by grouping specific parameterizations together and using predictors to adjust the input from the dynamics into the parameterizations (Wedi 1999), sampling different times on the time axis.

The wide ranges of spatial and temporal scales that are associated with the different components of weather, climate, and Earth system models have naturally resulted in different focuses in research. The continual increase of resolution means that increasing specialization is needed to address the physical processes that emerge on smaller and smaller scales as the grid size decreases. This specialization inevitably leads to the compartmentalization of the model codes and development teams. This compartmentalization and separation is necessary to understand and gain insights into the complex system and to render the model development manageable and tractable, but they are also in direct conflict with the desirability of unifying processes to allow tighter coupling and to eliminate coupling errors. This conflict is one of the most significant challenges for physics–dynamics coupling.

The compartmentalization leads to what is known as splitting, in which the impact of a process on the evolution of a model state is evaluated in isolation. Splitting assumes that the processes are either evaluated based on the same state and, hence, do not see the impact of other processes on that state, or they are evaluated sequentially (Donahue and Caldwell 2018). Both approaches are inaccurate reflections of reality. While splitting is useful and often unavoidable, it can lead to undesirable features in the numerical solutions. For example, process splitting can impact the model performance when processes compete for limited resources (such as the total water content of a parcel of air). This competition is particularly acute if processes are allowed to operate in isolation for a discrete time that is longer than their appropriate physical time scale. The modeling errors inevitably introduced by splitting are a core theme of the present paper.

Related to weather forecasting models are the examples presented below, such as the negative bias in the 24-h wind forecast noted by Beljaars et al. (2004); the accumulation of convective available potential energy (CAPE), allowing convection to initiate farther from the equator (Williamson and Olson 2003); impacts on the intertropical convergence zone (ITCZ), which may be relevant to forecasting in areas close to the equator; the coupling between the atmosphere and the ocean, which, despite the slowly changing ocean state, has been shown to be vital for forecasting on time scales of hours to weeks (Smith et al. 2018); and examples of the coupling of a weather forecasting model coupled to a regional oceanic model for a realistic simulation of a tropical

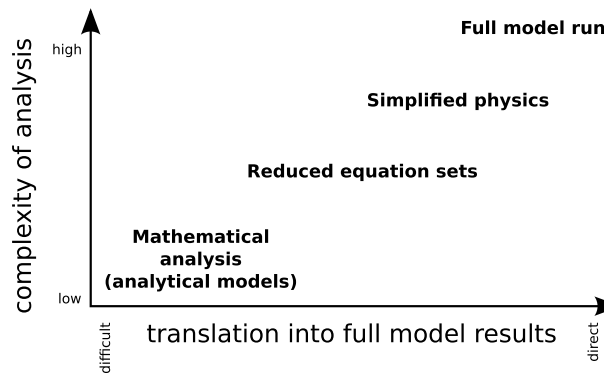
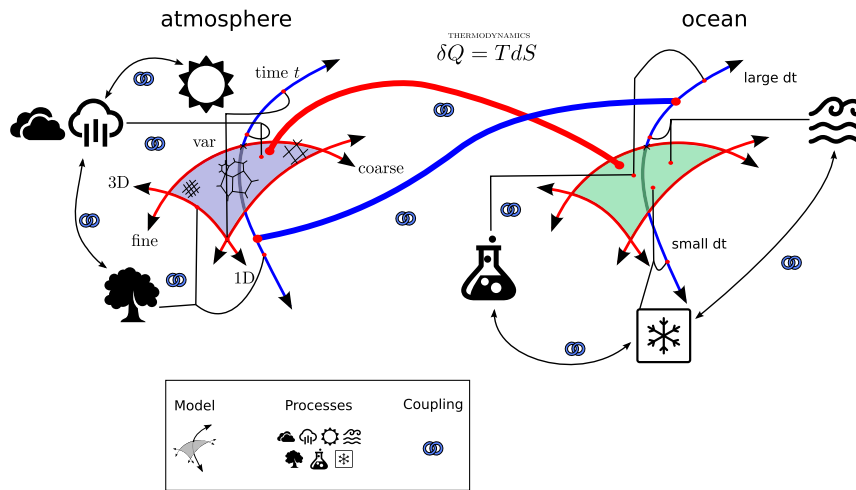


FIG. 1. Schematic representation of physics–dynamics coupling. (a) Two models: an ocean model and an atmosphere model. Both of these have spatial scales (here indicated by the plane with red lines) and temporal scales (indicated by the blue axis). These are coupled (thick lines); that means one domain in the spatial plane maps into the spatial plane of the other model (thick red line) and similarly in the temporal axis (thick blue line). In the spatial plane, aspects such as grid type, fixed vs variable resolution, one-dimensional vs three-dimensional, and fine vs coarse are shown as some of the aspects of the spatial resolution that can vary between models and do not necessarily have a straightforward mapping. Then, each of these models has its ecosystem of parameterizations (an arbitrary set of processes was chosen here for illustration only), which interact with the model and themselves via coupling. These parameterizations also occupy potentially—or almost certainly—different areas on the spatial plane and temporal axis. All of this exists in front of a background problem of thermodynamics, which ultimately governs them all (or ought to, anyhow). (b) Four-tier scheme of investigation, ranging from (by necessity) abstract analysis via reduced equation sets (with less necessity for abstraction) to simplified physics tests and finally full model runs. The complexity of the analysis increases from one to the other. The manner in which the results and conclusions from the experimentation can inform the production runs ranges from “difficult” (results are expected in the form of guidance or informing a choice that needs to be made in the design phase) to “direct” (a benefit can be demonstrated straightaway by producing an improved forecast).

cyclone. The gray zone topic features examples of grid-point storms and operational forecasting of downbursts and scale implications on the forecast error growth. The illustrations made using examples of climate models

apply directly to both the Earth system models and weather models, though the shorter forecast period may mean that some errors do not manifest themselves directly.

In early coupled climate models, such as the simulations of the global atmospheric circulation coupled to ocean processes presented in the late 1960s by Manabe and Bryan (1969), the much lower spatial resolution and much simpler model formulation were the dominant sources of model error. However, the rapid enhancement of computing capabilities has allowed for a substantial increase in model resolution as well as the incorporation of a much more comprehensive description of subgrid-scale phenomena, such as a more detailed description of microphysical processes. These advances have led to reduced errors in the individual model components. However, the benefits of this reduction in error will not be fully realized if the errors introduced by the coupling between components are not also reduced. Thus, numerical issues in coupling can be a bottleneck in the reduction of overall model error. Therefore, the formulation and implementation of the coupling—ideally, as a minimum—should

- represent correct asymptotic behavior (see sections 2 and 3);
- not introduce additional errors between different components, such as atmosphere and ocean (or at least the errors introduced should be smaller than the errors of each of the components; see section 5);
- respect the physical laws such as conservation of mass, momentum, and energy and the laws of thermodynamics (see section 6);
- represent accurately the interaction between components that represent a possibly vast range of time and space scales (see section 7);
- accommodate different types of discretization methods (e.g., spectral transform vs finite difference or finite element methods; see section 8a); and
- allow the possible use of different resolutions between components including variable and uniform resolutions (see section 8b).

Therefore, as Fig. 1a illustrates, physics–dynamics coupling is not limited only to the interaction between physics and dynamics. A key challenge is the design of time–space integration schemes for the different components that, when combined, reproduce the time–space-averaged behavior of *the whole system* being modeled.

The remainder of the paper is organized as follows. Section 2 focuses on issues related to process splitting in the time-stepping algorithm. The time–space convergence behavior of current models is also discussed. Section 3 then proceeds to illustrate convergence from the perspective of time–space averaging and the assumption of separation of scales, as well as how to accurately reproduce the asymptotic limits when subgrid transports play a crucial role. Section 4 emphasizes that

ideally, there would be a standard test procedure and established benchmark results across a whole range of models, with tests that isolate the components while still reflecting the model complexity and hence maintaining relevance. Section 5 focuses on the coupling between different models, such as atmosphere and ocean. Section 6 highlights the need for thermodynamic compatibility with the laws of thermodynamics. Sections 7 and 8 discuss the complexity of the interaction of parameterizations with increased model resolution, with that increase being either throughout the model domain or through the use of variable resolution within a model domain. Section 8 discusses new and emerging modeling strategies of separating physics and dynamics grids (section 8a) and how time stepping/process splitting (section 2) and scale awareness of deep convection (section 7) can interact and pose a challenge to models using spatially varying horizontal resolution (section 8b). The paper finishes with conclusions and an outlook (section 9).

## 2. Time-stepping errors introduced by splitting

Models rely on discretizing time and space dimensions to solve their equations numerically. These discrete time steps and grid spacings need to be relatively large to make calculations computationally affordable. Numerical errors arise from both the spatial and temporal discretizations. In this section, the focus is exclusively on time discretization by discussing model behaviors with fixed spatial resolution and different time steps.

### a. Impact of time-stepping errors

Time step size can have a substantial impact on the behavior of weather and climate models. For example, one metric of interest for future climate prediction is the change in global-mean surface temperature resulting from a doubling of carbon dioxide (CO<sub>2</sub>) concentration in the atmosphere. This temperature change was shown to vary by a factor of 2 in one version of the ECHAM5 climate model (Roeckner et al. 2003, 2006) when the model's time step size was varied between 5 and 40 min (Fig. 2). While solution sensitivity to time step size is not at all surprising from a mathematical perspective, such large discrepancies are undesirable numerical artifacts for model users who assume the models reflect the state-of-the-art understanding of the workings of the real-world system.

Sensitivity experiments like the one shown in Fig. 2 are rarely conducted with weather and climate models. Hence, the magnitude of the numerical artifacts is unclear in most models. In practice, model developers often tend to use the longest possible step size and then go through a time-consuming tuning process in which

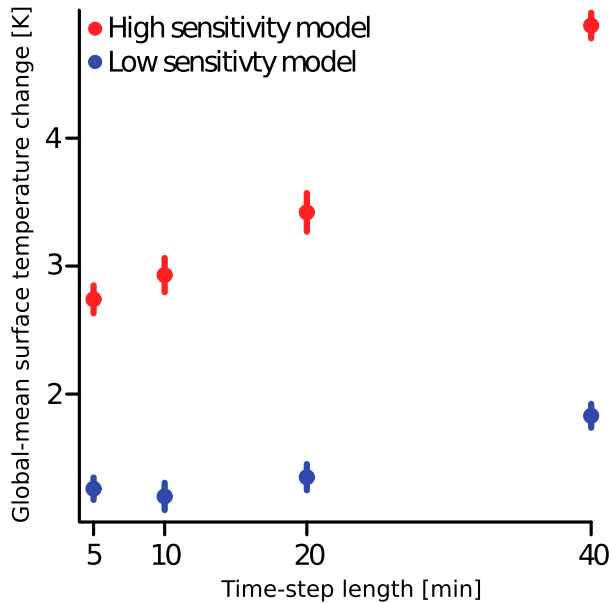


FIG. 2. Global-mean surface temperature change (K) resulting from a doubling of  $\text{CO}_2$  in simulations conducted with the ECHAM5 atmosphere model (Roeckner et al. 2003, 2006) coupled with a slab ocean. Red and blue markers indicate high- and low-sensitivity models, which differ only in a few uncertain parameters in the physics parameterizations (Klocke et al. 2011). For each time step size listed on the  $x$  axis, the global-mean surface temperature change is computed as the difference between a 10-yr present-day simulation and the last 10 years of a 50-yr simulation with doubled  $\text{CO}_2$ . The spatial resolution of the atmosphere model is T31 with 19 layers. Error bars indicate interannual variability of global- and annual-mean surface temperature.

uncertain model parameters are adjusted to match the model output with a chosen set of observations (Hourdin et al. 2017). One can argue that it might be possible to “tune away” the time step sensitivity by using different parameter values for different step sizes; however, there exists the danger that such tuning might result in error compensation that cannot be guaranteed for simulations under different forcing scenarios. Revision of the model and subsequent reduction of the time step sensitivity can provide confidence that results from the numerical models are reasonably accurate solutions of the underlying continuous physics equations, hence improving the credibility of future climate projections.

Strong sensitivities to model time step have been seen in other models as well. Wan et al. (2014) showed that when the physics time step was reduced from the default 30 to 4 min in the Community Atmosphere Model (CAM) version 5, the simulated December–February mean, globally averaged large-scale precipitation rate, liquid water path, and ice water path increased by about 10%, 20%, and 30%, respectively. Zhang et al. (2012) found that the impact of swapping aerosol nucleation

parameterizations on sulfuric acid gas and aerosol concentrations was overwhelmed by the effect of changing the time-stepping scheme used for solving the sulfuric acid gas equation in the aerosol–climate model (ECHAM-HAM). For the Integrated Forecast System (IFS), Beljaars et al. (2004) showed that the root-mean-square difference in 10-m wind speed between two 24-h weather forecasts conducted with 10- and 5-min step sizes was  $1.39 \text{ m s}^{-1}$ . They also showed that this root-mean-square difference could be reduced by about 1/2 when the numerical coupling between the dynamical core and turbulent momentum diffusion was revised to ensure a proper balance between the two processes.

Williamson (2002) mentioned that when the splitting method within the parameterization suite was modified, the National Center for Atmospheric Research (NCAR) Community Climate Model (CCM) version 3 (CCM3) produced a climate equilibrium that was substantially different from the default model in some small contiguous areas. In other areas, the climates were similar, but the balances producing them were different. Most of the studies cited above and the additional examples mentioned below indicate that *it is often the combination of coupling between processes and long time steps that cause time-stepping problems in contemporary models*. The remainder of this section is focused on coupling issues, though it is acknowledged that long time steps can cause issues within individual processes as well.

#### b. Splitting in the solution procedure

The process coupling discussed in this section includes the relationship between different parameterizations, the connection between a parameterization and the host model or between different physical phenomena within an individual parameterization. Splitting is employed to evaluate the tendency terms for each process and to combine their effects to advance the discrete solution in time.

The two most popular methods of splitting in operational models are sequential and parallel splitting. In sequential splitting, tendencies of the explicit processes are computed first and are used as input to the subsequent implicit fast process. Sequential splitting is in contrast to parallel splitting, where tendencies of all the parameterized processes are computed independently of each other, using the same fixed state from the beginning of the time step. In other words, in parallel splitting, the individual process can only react to the tendencies from the other processes in the subsequent time step.

Beljaars et al. (2004) advocate sequential splitting with processes ordered from slowest to fastest to allow processes to feed and balance each other within each

model step. The benefits of sequential splitting depend on what information from an already-calculated process is used in subsequent process calculations. The IFS uses both state information *and* tendencies from previous processes in some subsequent process calculations (hereafter referred to as sequential tendency splitting). Therefore, processes see the tendencies of some of the prior processes, but the model state is updated at the end of the time step. CAM physics uses sequential update splitting, where a process operates solely on the model state updated by the immediately preceding process. Since sequential tendency splitting shares more information than sequential update splitting or parallel splitting, it unsurprisingly performs better. More sophisticated coupling has also been shown to be beneficial for specific processes. For example, in the Semi-Lagrangian Averaging of Physical Parameterizations (SLAVEPP) algorithm of Wedi (1999), the tendencies are evaluated at both the departure and arrival points of the semi-Lagrangian trajectory and then averaged.

### c. Issues with splitting

Splitting causes an error when interacting processes are considered in isolation. The errors can be large—and the numerical solutions can depend strongly on process ordering—when splitting is used in combination with time steps on the order of, or longer than, the inherent process time scales. Two types of process interactions are commonly seen in the atmosphere: competition and compensation. Competition refers to cases where multiple processes consume the same resources (e.g., cloud water or CAPE), whereas compensation relates to cases where one process is a source for something the other process consumes. A situation for competition arises in the consumption of CAPE, which can be removed by shallow convection, deep convection, or resolved-scale motions. Williamson (2013) provides an example of competition for CAPE in a sequential update split model. Explicit stratiform condensation is considered a fast process in CAM4, and the associated latent heating is applied in a single time step as a hard adjustment, while CAM4's deep convection parameterization has a fixed time scale of 30 min for CAPE removal. When the model time step is shortened, the ability of these processes to consume convective instability is altered: the fixed time scale process does less, and the hard adjustment does more, resulting in extreme vertical motion and heavy precipitation due to the interaction between the dynamics and the parameterizations. While this might be described as a time step sensitivity, it is instead a sensitivity to the ratio of parameterization time scales, which changes with time step.

Less severe sensitivities have been observed by other investigators in scenarios of competition between processes. Mishra and Sahany (2011) found sensitivity to time step in the average tropical rainfall amount in CAM3 multiyear simulations, noting it was associated with the change in partitioning between convective and large-scale precipitation. Reed et al. (2012) showed sensitivity in the strength of idealized tropical cyclones in high-resolution CAM5 to time step, relating it to the accompanying change to the partitioning between convective and large-scale precipitation. In both studies, the time scale of the convection was not changed, and thus, the ratio of time scales changed. This issue of partitioning is a typical symptom observed in models that use spatial resolutions in the gray zone of cumulus convection (section 7). Although the examples cited above are all from models that use sequential splitting, competition for resources is also a problem for parallel splitting because it can result in unrealistically strong removal of resources. The most egregious cases of this are, for example, negative concentrations of water vapor, hydrometeors, or other tracer species. These are typically resolved by rescaling tendencies to prevent overconsumption. This approach may leave more subtle cases untreated and, where applied, results in transport that does not locally satisfy the transport equations of the model.

Another example of the competition problem was shown by Wan et al. (2013), in which the sulfuric acid condensation and aerosol nucleation acted as two sink processes in the sulfuric acid gas budget in the ECHAM-HAM model. They argued that more accurate simulations of the process rates—and consequently, more accurate near-surface concentrations of aerosol particles and cloud condensation nuclei—can be obtained when a solver handles the competing processes simultaneously without splitting.

The second type of process interaction that can cause a potential splitting problem is the cases of compensation; that is, one process acts as a *source* for something, whereas the other process acts as a *sink*. If these processes are coupled by sequential update splitting, the first process might push the quantity of interest to unreasonably high levels, while the second process might pull it to unreasonably low levels. With parallel splitting, the consuming process does not see a state immediately influenced by the source process until the following time step, by which time the excess may have been modified by some other process. An example of such a push/pull problem with sequential update splitting in CAM5 was presented by Gettelman et al. (2015), who note that macrophysics, the interplay of condensation/evaporation and cloud fraction, is the primary

source of cloud water, which is subsequently depleted by microphysical processes. By substepping macro- and microphysics together two times during the typical 5–30-min time step, they were able to obtain more realistic model behavior. [Wan et al. \(2013\)](#) describe another push/pull problem related to the sulfuric acid gas budget in ECHAM-HAM. The study compared multiple time-stepping schemes for the coupling of sulfuric acid gas production and condensation. Results show that when the discrete time step is long, compared to the characteristic condensation time scale, sequential splitting between production and condensation leads to a substantial overestimate of the condensation rate, even when the individual processes are represented with accurate solutions of the split equations. When practical to do so, the strongly interacting sources and sinks should be solved simultaneously. A third example is presented by [Beljaars et al. \(2004\)](#) for the IFS. The near-surface wind speed is mainly affected by the pressure gradient force, the Coriolis force, and the turbulent friction. Sensitivity tests showed that if the turbulent diffusion coefficients are computed after the model state variables have been updated by the dynamics-induced tendencies, positive biases in the intermediate wind speeds will lead to overestimation of turbulent friction and thus negative bias in the 24-h wind forecast. These results underline further the relevance of coupling aspects, not only for climate, but also for short- and medium-term weather forecasts.

Splitting would not cause severe problems in the cases of process competition or compensation if the model time step were sufficiently short to resolve the time scales associated with the individual processes and their interactions. In that scenario, the processes—although isolated during a single short time step—could interact indirectly with each other at the next time step via the updated model state. However, many of the parameterized processes are fast, and long model time steps are not uncommon in operational models where the time step correlates with computational cost. [Gettelman et al. \(2015\)](#) note that sequential update splitting with forward Euler time stepping in CAM5 microphysics creates negative cloud water when computed tendencies are multiplied by inappropriately long time steps. This negative cloud water then needs to be removed by schemes that are not physically motivated by the underlying transport equations, such as rescaling, as noted above. [Williamson and Olson \(2003\)](#) found that aquaplanet simulations conducted with the NCAR CCM3 model had a single narrow peak of zonal-mean precipitation at the equator when the Eulerian dynamical core was used, while simulations using the semi-Lagrangian dynamical core had a double ITCZ. A double ITCZ is characterized by a precipitation minimum at the equator and two maxima that

are straddling the equator. This sensitivity was attributed to the different time step sizes used for the physics parameterizations in the two model configurations (20 min for Eulerian, 60 min for semi-Lagrangian) rather than the dynamical cores themselves. The explanation the authors provided was that with sequential splitting, longer time steps lead to the accumulation of more CAPE, allowing convection to initiate farther from the equator. The resulting condensational heating and secondary circulation further reinforce convection away from the equator. Similar changes to ITCZ shape in aquaplanet simulations with the CAM3 model have also been reported by [Li et al. \(2011\)](#).

#### *d. Addressing the splitting problem*

Tighter coupling between processes is necessary to alleviate the splitting problems noted in [sections 2a–c](#). From the perspective of time discretization alone, three strategies have been seen in the literature. The first strategy is the use of shorter time steps to subcycle clusters of strongly interacting processes while keeping the step size of the rest of the model unchanged. Such treatment is applied to large-scale condensation and cloud macrophysics in some versions of CAM5 and its successors (e.g., [Gettelman et al. 2015](#)). The second strategy uses sequential tendency splitting to allow faster processes to better react to the effects of slower processes, like the IFS example of dynamics–turbulence coupling in weather forecasts ([Beljaars et al. 2004](#)), mentioned earlier in this section. The third strategy is the use of specially designed solvers to handle multiple processes simultaneously, such as the sulfuric acid gas equation example by [Wan et al. \(2013\)](#) discussed in [section 2c](#). Methods of the second and third strategies can be somewhat involved, and their feasibility will depend on the design of the specific parameterizations. Since it can be challenging to formulate a coherent numerical coupling for complex parameterizations that might have been designed with different concepts and use different prognostic variables, attempts to account for process interactions in the continuous or semi-discrete formulation of the equations could also be helpful. For example, thermal instability diagnosed directly from radiative heating profiles is considered in the calculation of entrainment at the top of the cloudy boundary layer in the turbulence schemes by [Lock et al. \(2000\)](#) and [Bretherton and Park \(2009\)](#), which improves the radiation–turbulence coupling from the perspective of time stepping. Some modern parameterizations are designed to handle multiple atmospheric processes in a unified way. Examples include the eddy diffusivity–mass flux (EDMF) scheme of [Siebesma et al. \(2007\)](#) and the Cloud Layers Unified by Binormals (CLUBB) scheme

of Golaz et al. (2002a), both of which combine the representations of turbulence and shallow convection. Another example is the parameterization of Park (2014) that represents both shallow and deep convection. Such unified parameterizations provide an opportunity to handle better the interactions between the processes they unify, although those parameterizations can still have strong interactions with other parameterizations, and the time stepping has to be implemented carefully. For instance, CLUBB and cloud microphysics are subcycled together in recent versions of CAM to achieve a tighter coupling.

#### *e. Assessment of time step convergence*

Complementary to the design of tighter coupling methods, an assessment of solution behavior in the regime of very short step sizes may provide information to help achieve the ultimate goal of higher accuracy at longer step sizes. In the development of time integration methods for differential equations, convergence analyses that examine whether the numerical error decreases with step size at the expected rate are one of the standard ways for verifying whether the discrete methods and code implementation lead to the intended outcome. Applications of such analysis to the physics parameterizations or full complexity models are rarely seen in the literature. The lack of interest is partly attributable to the concern that physical parameterizations are often designed to work within a particular range of time step sizes, and to use the parameterizations outside of that range may violate physical assumptions, resulting in the model state converging to an unintended or unphysical state. We argue that ideally, the physical assumptions and numerical methods should be clearly separated; the purpose of a time step convergence analysis should be the identification of issues in the numerical methods.

In the absence of analytic solutions, a “proxy ground truth” is needed in a convergence analysis. Recent studies by Teixeira et al. (2007) and Wan et al. (2015) attempted to establish a “proxy ground truth” by running the Navy Operational Global Atmospheric Prediction System (NOGAPS) and CAM5 models with small time step sizes. Wan et al. (2015, p. 216) argued that “convergence toward this proxy [ground truth] is a necessary but insufficient condition for the convergence toward the true solution.” In Teixeira et al. (2007), NOGAPS was found to converge at a first-order rate near the start of the simulations, but the chaotic nature of nonlinear dynamical systems eventually caused simulations with different step sizes to diverge into uncorrelated sequences of weather events, hence loss of convergence. Hodyss et al. (2013) demonstrated with

simplified models that when the time stepping scheme does not resolve the parameterized physical processes, the numerical solutions will behave as predicted by the theory of stochastic differential equations. The 1-h simulations that Wan et al. (2015) conducted with the CAM5 model converged at a rate of 0.4 instead of the expected value of 1.0, and the cause was unclear. Given the rare application of such analyses, the understanding of time step convergence in weather, climate, and Earth system models is very limited. Nevertheless, Wan et al. (2015) showed that convergence analysis conducted with individual components of a model could indicate which parts have stronger time step sensitivity and thus require more attention in future development.

With these real-world issues and examples in mind, the paper now proceeds into a more theoretical area, a mathematical analysis approach to the coupling, moving toward the bottom-left of the graph in Fig. 1b.

### **3. Insights from models with simplified equation sets**

In the following two examples, the resolved scale behavior is strongly dependent on the subgrid-scale dynamics. First, the interaction of convection with dynamics is examined, followed by the boundary layer with dynamics. This discussion highlights situations where the combination of resolved and subgrid terms is critical (e.g., in representing the total transport as the sum of resolved and subgrid transport). As the averaging scales such as time step and grid resolution are reduced, the subgrid contribution will diminish and be taken over by the resolved contribution.

#### *a. Interaction of convection with balanced dynamics*

In the interaction of convection with balanced dynamics, the spatial averaging scale is assumed sufficiently large, and therefore the semigeostrophic model, which is an accurate approximation to the governing equations on large scales (Cullen 2006), can be used as a proxy for the evolution of the spatially averaged equations. This analysis has the advantage that the “proxy ground truth” (section 2e) is known. The behavior of this model can then be compared with solutions of the exact governing equations with a much finer averaging scale, which consequently resolve convection explicitly. The observed behavior then has implications for the design of models with parameterized convection.

The semigeostrophic model includes the effects of large static stability variations, which are essential in considering interactions with convection. For illustration, the incompressible Boussinesq form of the equations in Cartesian geometry is used. This form uses the

ageostrophic wind equation [Eq. (A1)] with the “potential vorticity” matrix  $\mathbf{Q}$  [Eq. (A2)] and forcing  $\mathbf{H}$  [Eq. (A3)]. This forcing includes momentum and thermodynamic forcing terms.

Under semigeostrophic dynamics, the ageostrophic flow is determined diagnostically and includes subgrid as well as resolved fluxes. The ageostrophic motion thus represents a response to the dynamical and physical forcing represented in Eq. (A1). The strength of the response is determined by the eigenvalues of  $\mathbf{Q}$ , which represent the inertial and static stability of the atmospheric state. The geostrophic state would be expected to be described by the resolved flow in numerical models. However, the ageostrophic circulation required to maintain geostrophic balance would include subgrid-scale transports as well as resolved ageostrophic transport.

In the presence of moisture, the static stability is reduced by latent heating. This reduction of stability could be expressed, neglecting the condensate loading term in the buoyancy, by replacing the potential temperature  $\theta$  with the equivalent potential temperature in saturated regions. In the presence of moist instability,  $\mathbf{Q}$  would then have a negative eigenvalue. As illustrated by Holt (1989), this will generally result in convective transport rather than continuous vertical motion. The effect is that convective updrafts with any associated convective downdrafts would replace the ascending part of the ageostrophic circulation, while the compensating circulation would be a smooth transport.

The semigeostrophic formulation identifies the convective locations by a negative eigenvalue of the  $\mathbf{Q}$  matrix and generates the upward mass transport as modeled by a convection scheme. The downward branch would be determined by mass continuity and the need to maintain balance in the environment. In the tropics, this leads to spreading of the response over a wide area. This process is illustrated using a convection-permitting simulation performed as part of the Earth System Model Bias Reduction and Assessing Abrupt Climate Change project (EMBRACE; [http://cordis.europa.eu/project/rcn/99891\\_en.html](http://cordis.europa.eu/project/rcn/99891_en.html)). The simulation uses a configuration similar to that used operationally at the Met Office for the United Kingdom–area short-range weather prediction [see Holloway et al. (2012) for details] but with changes made to improve the representation of tropical convection and gravity waves. In this configuration, the model has a horizontal grid spacing of 2.2 km with an 8800 km  $\times$  5700 km domain centered on the tropical Indian Ocean and 118 vertical levels with a 78-km lid. Within its domain, the convection-permitting simulation was run freely after being initialized from the operational Met Office global model analysis valid at 0000 UTC 18 August 2011. The lateral boundary

conditions were provided every time step by a global model that was reinitialized from Met Office operational analyses every 6 h. The data presented here were taken from 0000 UTC 30 August 2011 after the convection-permitting simulation was fully spun up.

The grid points are classified as cloudy or dry, depending on the presence or not of cloud condensate: the cloudy areas are further subdivided into ascending and descending. The grid points are then aggregated onto a coarser, 24-km grid. This 24-km grid represents a typical resolution at which a convective parameterization is used. Then, for each 24-km grid point, cloudy and dry mass flux, cloudy updrafts and downdrafts, and the total large-scale mass flux are obtained by summing the vertical mass fluxes  $\rho w$  in the respectively partitioned grid points.

Figure 3 shows that for 24-km grid points that have some cloud, there is a close match between the total large-scale mass flux and the cloudy mass flux, the sum of up- and downdraft; hence, most of the vertical motion happens within the cloudy areas (section 7b). The values of the dry mass flux are unrelated to the cloudy updraft mass flux. Hence, the local compensating subsidence within the 24-km grid box does not match the net upward cloudy mass flux, as is usually assumed in convective parameterizations. The subsidence is instead spread over the whole domain. This spreading is in agreement with the idea that the ascent is represented by convective updrafts, while the subsidence is spread over a much broader region (Bretherton and Smolarkiewicz 1989). This exposition suggests that a radical rethink of convective parameterization strategy is required. An example for convection is the parameterization of Grell and Freitas (2014) or the even more radical approach of Kuell et al. (2007).

#### b. Interaction of the boundary layer with balanced dynamics

Shifting the focus from convection to the boundary layer, the effectiveness of different coupling strategies is compared using a simple model as the asymptotic limit of the full equations. A large-scale balance is defined, which should be represented in the resolved numerical solutions, while the circulation required to maintain it will be described by both resolved and subgrid-scale transports. The inclusion of the boundary layer makes a fundamental change to the large-scale balance because of the need to satisfy the no-slip boundary condition. Thus, the balance is defined by the Ekman relations

$$\frac{\partial p}{\partial x} - f v_e = \mathcal{F}_1(\mathbf{u}_e), \quad \text{and} \quad \frac{\partial p}{\partial y} + f u_e = \mathcal{F}_2(\mathbf{u}_e), \quad (1)$$

where  $\mathbf{u}_e = (u_e, v_e)$  are the components of the Ekman layer velocity, and  $\mathcal{F}_1$  and  $\mathcal{F}_2$ , subcomponents of the  $F_1$  and  $F_2$

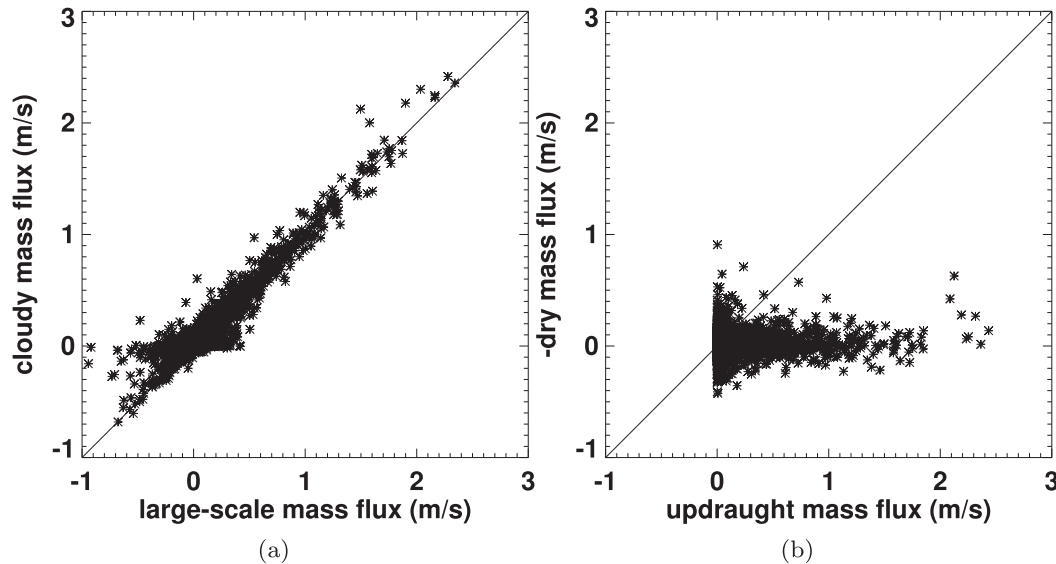


FIG. 3. (a) Scatterplots of cloudy mass flux against large-scale mass flux and (b) minus dry mass flux against cloudy updraught mass flux. The mass fluxes have been converted to velocities in units of  $\text{m s}^{-1}$  by normalization with density. The data are taken from a height of 3195 m and are averaged in the horizontal to scale of 24 km. Met Office Unified Model.

introduced above, represent the parameterized friction terms, which will depend on the horizontal momentum as indicated, as well as the thermodynamic structure. These equations can be solved for  $\mathbf{u}_e$ , given that  $\mathbf{u}_e = \mathbf{u}_g$  at the top of the boundary layer and is zero at the ground.

Beare and Cullen (2013) derive equations analogous to Eq. (A1) for the circulation required to maintain Ekman balance in time in the presence of dynamical and physical forcing. The ageostrophic circulation in semi-geostrophic theory is an accurate second-order approximation in Rossby number to the velocity in the Euler equations. However, the equivalent circulation in the boundary layer is only first-order accurate, as is the Ekman balance itself.

The effectiveness of schemes to couple the boundary layer with the balanced dynamics is demonstrated by following the method of Cullen (2007). This experiment is described in detail by Beare and Cullen (2016). A vertical slice model is used to construct a sequence of solutions of the boundary layer driven by a baroclinic wave where the Rossby number  $U/fL$ , with  $U$  and  $L$  denoting horizontal velocity and length scales, respectively, is progressively reduced. This reduction is achieved by maintaining the same initial structure in the pressure and potential temperature while simultaneously increasing the Coriolis parameter and decreasing the wind speed. The difference between the circulation predicted by the balanced Eq. (1) and the solution of the hydrostatic equations is then calculated.

The convergence behavior of the balanced solution to the solution of the hydrostatic primitive equations is as expected. The convergence is of second order outside the boundary layer and first order inside. However, the boundary layer becomes shallower as the Rossby number ( $Ro$ ) is reduced, giving an overall convergence rate of  $Ro^{1.7}$ .

Results are compared using three numerical implementations: standard implicit time stepping, the Wood et al. (2007) scheme, and the  $K$ -update scheme. The control simulation uses standard implicit time stepping, but the mixing coefficients  $\mathcal{F}_1$  and  $\mathcal{F}_2$  are evaluated only at the beginning of the time step. The Wood et al. (2007) scheme is a stable single step scheme that is unconditionally stable and second-order accurate. This stability and accuracy is achieved by assuming a polynomial dependence of  $\mathcal{F}_1, \mathcal{F}_2$  on wind speed. The  $K$ -update scheme includes the updated value of the boundary layer mixing coefficient at the new time level in each time step as described by Cullen and Salmond (2003), as well as the more accurate representation of the diffusion process in Wood et al. (2007). This inclusion allows the scheme to represent the balanced solution more accurately.

Figure 4 shows the difference between primitive equation simulations using different boundary layer time-stepping schemes and the balanced model. At smaller Rossby numbers, all primitive equation models follow the ideal  $Ro^{1.7}$  line. However, above  $Ro = 0.08$ , the primitive equation model using the implicit scheme

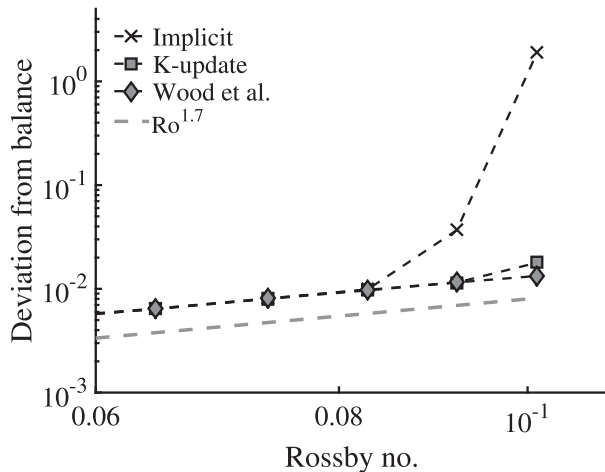


FIG. 4. Convergence to circulation required to maintain Ekman balance of the vertical slice primitive equation simulations (Beare and Cullen 2016) for different time-stepping schemes: implicit,  $K$ -update, and Wood et al. (2007).  $Ro^{1.7}$  is shown in gray for reference of the slope ( $y$ -axis intercept is arbitrary).

starts to deviate significantly above the ideal line and no longer converges at the required rate. The primitive equation model using the  $K$ -update scheme deviates slightly above the ideal line at  $Ro = 0.1$ . The hydrostatic primitive equation (HPE) model using the Wood et al. (2007) scheme follows the ideal  $Ro^{1.7}$  line for the range of  $Ro$  shown. Both the  $K$ -update and Wood et al. (2007) schemes account for the variation of the boundary layer diffusion across the time step, giving the improved convergence properties compared to the implicit scheme. The deviation from the Ekman-balanced models thus exposes differences in the numerical methods employed.

This and the previous subsection demonstrated two validation approaches of physics–dynamics coupling methods. This validation is possible even though the required averaged solution of the full equations cannot be described exactly by the solution of a set of partial differential equations. The above has shown that subgrid models can be validated by the accurate reproduction of asymptotic limits where subgrid transports are a crucial part of the limit solution.

#### 4. Analyzing the coupling of dynamical cores with a hierarchy of GCM test cases

One of the recurring questions is this: Which physics–dynamics coupling scheme is better? The answer depends crucially on the objective of the model run. Is it a climate run or a weather forecast? Is the model already severely time step restricted, such as Eulerian formulations, or are long time steps permitted, as in semi-implicit semi-Lagrangian models? Eulerian

formulations may be less susceptible to coupling errors, assuming the physics and dynamics time steps are not too disparate, due to the higher temporal resolution and less scope for splitting errors to evolve during a time step. But even when these questions have been answered, in the full model context, it is far from trivial to say which is better. Therefore, testing is essential, and, in this present publication, it is proposed that a hierarchy of idealized general circulation model (GCM) and weather model test cases facilitate an improved understanding of the coupling mechanisms, compared to analyzing outputs of full model runs.

##### a. Idealized testing of global circulation and weather models

Full model testing has been discussed above, and, for example, Wan et al. (2015) proposed various analysis techniques to better understand the impact of the physics time step on the model behavior. In their work, the numerical convergence of 1-h simulations was analyzed with fixed horizontal grid spacing. The convergence rate was derived by varying the process-coupling time step between 1800 and 1 s. The discrepancy between the expected and realized convergence rates pointed to the stratiform cloud schemes as the primary cause of slow time step convergence. The general test procedure applies to any atmospheric model and can help quantify the time stepping errors and identify the related model sensitivities. From a physics–dynamics coupling point of view, however, these results are still difficult to translate into improvements of, or to highlight deficiencies in, the coupling schemes. In an idealized framework, the parameterizations and lower boundary conditions are more constrained, which exposes the impact of physics–dynamics coupling on the simulation in a more transparent way.

##### 1) THE DIFFERENT NATURE AND SOURCES OF ERROR

As with new parameterizations, when a novel coupling scheme is implemented in a tuned model (Hourdin et al. 2017), the solution is likely to be worse for the new coupling method if the model is then not retuned, even if the new coupling scheme would lead to a superior solution in the absence of tuning. Model tuning inevitably tunes against errors that are independent of the parameters tweaked in the tuning process (i.e., compensating errors). In this case, multiple errors may exist, but the superposition of errors introduced to minimize other errors may result in “shadowing of errors” if only the final solution is taken into account during tuning processes. Remove one of these errors, and the result will be worse, despite having eliminated an error. For example, removing (or reducing) errors in the coupling of a

mature model may result in a degraded final solution for these reasons. A key challenge in physics–dynamics coupling is that no one single experiment will distinguish a superior coupling method from the inferior. The different techniques presented here have to be taken as a cohort of interrogation. Each has to be interpreted under their limitations. It should be possible to derive more explicit guidelines and understanding of the complex interactions when the experiments are combined in a logical structure, a hierarchy, with an associated analysis protocol.

## 2) THE TEST CASE HIERARCHY

Because of the interconnected sources of error illustrated above, it seems reasonable to implement and standardize an idealized testing protocol. This protocol should be idealized in such a way that the complexity of physical parameterizations is present in the forcing, but not in the implementation. The implementation has to be simplified. This simplification will come at a cost, and it will probably not verify as well with observations as a state-of-the-art parameterization would. This lack of performance, however, is not a problem here as it is meant to be a test bed, not a forecasting model. This simplification then allows a generalization, meaning that in every model where it is added, it is generally the same. This generalization then allows for direct comparisons between models. Ideally, a set of tests would be available, evenly distributed along the graph of Fig. 1b, covering all levels of complexity. Ideally, in between the two well-observed and understood boundary conditions—sea surface temperature (SST) and incoming shortwave radiation at the top of the atmosphere—as much as possible should be left to the model. Variables should be allowed to propagate freely and not be prescribed or constrained to reference profiles or background states. For the dynamical core, tests with idealized forcing exist, such as the Held–Suarez test case (Held and Suarez 1994). The Held–Suarez forcing was formulated for a dry and flat planet and includes a thermal relaxation mechanism and low-level Rayleigh friction. These mimic the effects of radiation and boundary layer mixing, respectively. However, the adjustment processes in the Held–Suarez test case are rather slow and do not challenge the physics–dynamics coupling sufficiently. A missing ingredient is moisture. The latent heat exchanges due to water phase transitions are desirable to stress the coupling mechanisms.

The “simple physics” package by Reed and Jablonowski (2012) incorporates bulk aerodynamic surface fluxes and diffusive boundary layer mixing processes of heat, moisture, and momentum, a large-scale condensation scheme based on moisture and instantaneously removed

precipitation, and uses an ocean-covered surface with prescribed SSTs as a lower boundary condition. The Fortran source code is publicly available (<https://earthsystemcog.org/projects/dcmip-2012/>), removing the uncertainty of the implementation. The suite is simplistic enough to be easily reproduced within varying model frameworks. However, the simple-physics package lacks radiation and is therefore only suitable for short-term simulations. This lack of thermal forcing was remedied by Thatcher and Jablonowski (2016), who combined the ideas of the Reed and Jablonowski (2012) simple-physics package and the Held–Suarez forcing to create a moist version of the Held–Suarez test. The resulting Moist Idealized Test Case (MITC) with Newtonian thermal relaxation mimicking “radiation” is suitable for long-term simulations and has been shown to reveal some of the intricacies of the physics–dynamics coupling, as further highlighted in section 4b. MITC can be considered a moist idealized test of intermediate complexity. The MITC Fortran routine is available as a supplement to Thatcher and Jablonowski (2016) on the publisher’s web page.

The next step in the test case hierarchy points to simplified physics formulations with a radiation scheme and unconstrained SSTs. These SSTs can, for example, be determined by a slab ocean model (also called “mixed layer” model). Frierson et al. (2006) presented a gray-radiation GCM, which possesses desirable processes such as radiation, an interactive slab ocean, large-scale precipitation, and surface/boundary layer schemes. However, the physics suite is not sufficiently documented to be easily reproducible and comparable to other models. If more realistic ocean temperatures are desired, a slab ocean scheme can also be augmented with a set of specified surface flux adjustments (commonly called “ $q$ -flux adjustments”; e.g., Russell et al. 1995; Sun and Hansen 2003; Zhang and Delworth 2005). These can be added to the slab model’s temperature tendency equation at each time step to maintain a seasonal cycle of realistic ocean temperatures.

A final step in the idealized GCM hierarchy is a long-term aquaplanet simulation on a flat and ocean-covered Earth that uses the complex physical parameterization package of a GCM. The lower boundary condition can either be based on prescribed SSTs as in Neale and Hoskins (2000) or on a slab ocean approach with predicted SSTs as in Lee et al. (2008). Aquaplanet simulations are popular for idealized climate studies, partly due to their perpetual equinox condition, which eliminates the seasonal cycle, allowing for relatively short simulations to reach equilibrium compared to full-physics climate simulations. Aquaplanet simulations can also provide insight into the delicate interplay between the physical parameterizations and the numerical

schemes of dynamical cores with their associated diffusion (section 4c).

For numerical weather prediction models in particular, further idealized tests can be analyzed, such as the Splitting Supercell Test Case (Zarzycki et al. 2018). In this test case, the horizontal scale of the convective plumes is on the order of 1 km, similar to many current weather forecast model resolutions. This test case challenges in particular nonhydrostatic dynamics.

### b. Simplified physics assessments

Figure 5 displays an example of how the MITC approach by Thatcher and Jablonowski (2016) can provide information about the physics–dynamics coupling scheme. The figure shows instantaneous, randomly selected snapshots of the 850-hPa vertical pressure velocities and precipitation rates in MITC simulations with the CAM5 model (Neale et al. 2010b). The depicted CAM5 dynamical cores are the finite volume (FV) core (Lin 2004), the spectral transform Eulerian (EUL) dynamical core, and the spectral element (SE) core (Taylor and Fournier 2010; Dennis et al. 2012). These are run at the horizontal grid spacing  $1^\circ \times 1^\circ$  ( $\approx 111$  km); the triangular truncation T85 with a quadratic Gaussian grid ( $\approx 156$  km); and in the “ne30np4” (SE) configuration, which corresponds to a grid spacing of about 111 km, respectively. All dynamical cores use the same 30 vertical levels. The vertical-level positions are documented in the appendix of Reed and Jablonowski (2012).

The three dynamical cores are coupled to the MITC physics package by Thatcher and Jablonowski (2016) and run for multiple years. Within the MITC physics package, the coupling of the various physical processes follows the sequential update approach, which is also detailed in Thatcher and Jablonowski (2016). However, the physics–dynamics coupling schemes differ. The FV dynamical core (Figs. 5a,e) with a dynamics time step of 180 s is coupled to the physics package in a time-split (sequential) way and applies the physical forcings every 1800 s (physics time step). The EUL dynamical core (Figs. 5b,f) is coupled to the physics in a process-split (parallel) way. EUL applies the physical forcings every 600 s, which is identical to EUL’s dynamics time step. The SE dynamical core (Figs. 5c,d,g,h) with a dynamics time step of 300 s is coupled to the physical parameterizations in a time-split way with a physics time step of 1800 s, as in FV. However, two coupling options exist in SE, which apply the physical forcings either as a sudden adjustment after the long 1800-s physics time step ( $se\_ftype = 1$ ) or gradually within the subcycled dynamical core ( $se\_ftype = 0$ ) every 300 s.

Figures 5c, 5d, 5g, and 5h document that the choice of the coupling scheme in CAM5-SE has a significant

impact on the simulation. Intense gridscale (or gridpoint) storms (Williamson 2013) develop along the equator in all models (seen in the precipitation rates in the right column). These storms lead to circular gravity wave ringing patterns in the 850-hPa vertical pressure velocity  $\omega$  in CAM5-SE when coupled with the long 1800-s physics time step ( $se\_ftype = 1$ ; Fig. 5c). The centers of the circular  $\omega$  patterns coincide with the positions of the strongest precipitation rates in Fig. 5g, which suggests that the intense latent heat release at these locations initiates the gravity wave noise. The gravity wave response to the impulsive physical forcing is large scale so that the explicitly applied diffusion in CAM5-SE does not filter out its propagation. Thatcher and Jablonowski (2016) found that the gravity wave noise can be remedied when changing the coupling scheme in CAM-SE. In the case of  $se\_ftype = 0$  (Figs. 5d,h), the physical forcing tendencies are gradually applied within the CAM-SE dynamical core every 300 s. The strong gridscale storms are still present in the precipitation field (Fig. 5h). However, the more gradual forcing reduces the latent heat impulses and leads to a smooth vertical pressure velocity (Fig. 5d). Similar sensitivities to the  $se\_ftype$  setting were also found in full-complexity CAM-SE climate simulations (P. Lauritzen 2015, unpublished research). Therefore, the CAM-SE  $se\_ftype$  default was switched from 1 to 0. These results show that simpler modeling frameworks help expose the causes and effects of the physics–dynamics coupling choices.

Comparing the CAM-SE characteristics to the alternative FV and EUL dynamical cores highlights crucial differences. As in SE ( $se\_ftype = 1$ ), the FV model (Figs. 5a,e) also adjusts the state variables with an 1800-s physics time step and experiences equatorial gridpoint storms of similar magnitude (Fig. 5e). However, the damping characteristics of the two dynamical cores differ (Jablonowski and Williamson 2011), and FV can more effectively damp gridscale noise due to its built-in local monotonicity constraints and explicitly applied second-order divergence damping mechanism. In contrast, SE and EUL damp the divergent part of the flow with an explicitly applied, more scale-selective fourth-order damping mechanism. Therefore, FV is inherently more damping for gravity waves that are caused by latent heat impulses. FV distributes the latent heating forcing more smoothly, which leads to a smoother distribution of its vertical pressure velocity (Fig. 5a). In contrast, the EUL model is built upon a global spectral numerical method, which is known for its difficulty representing sharp contrasts locally. Here, the latent heating impulses near the peak precipitation rates (Fig. 5f) lead to the Gibbs ringing effect (Jablonowski and Williamson 2011). The Gibbs ringing is visible in

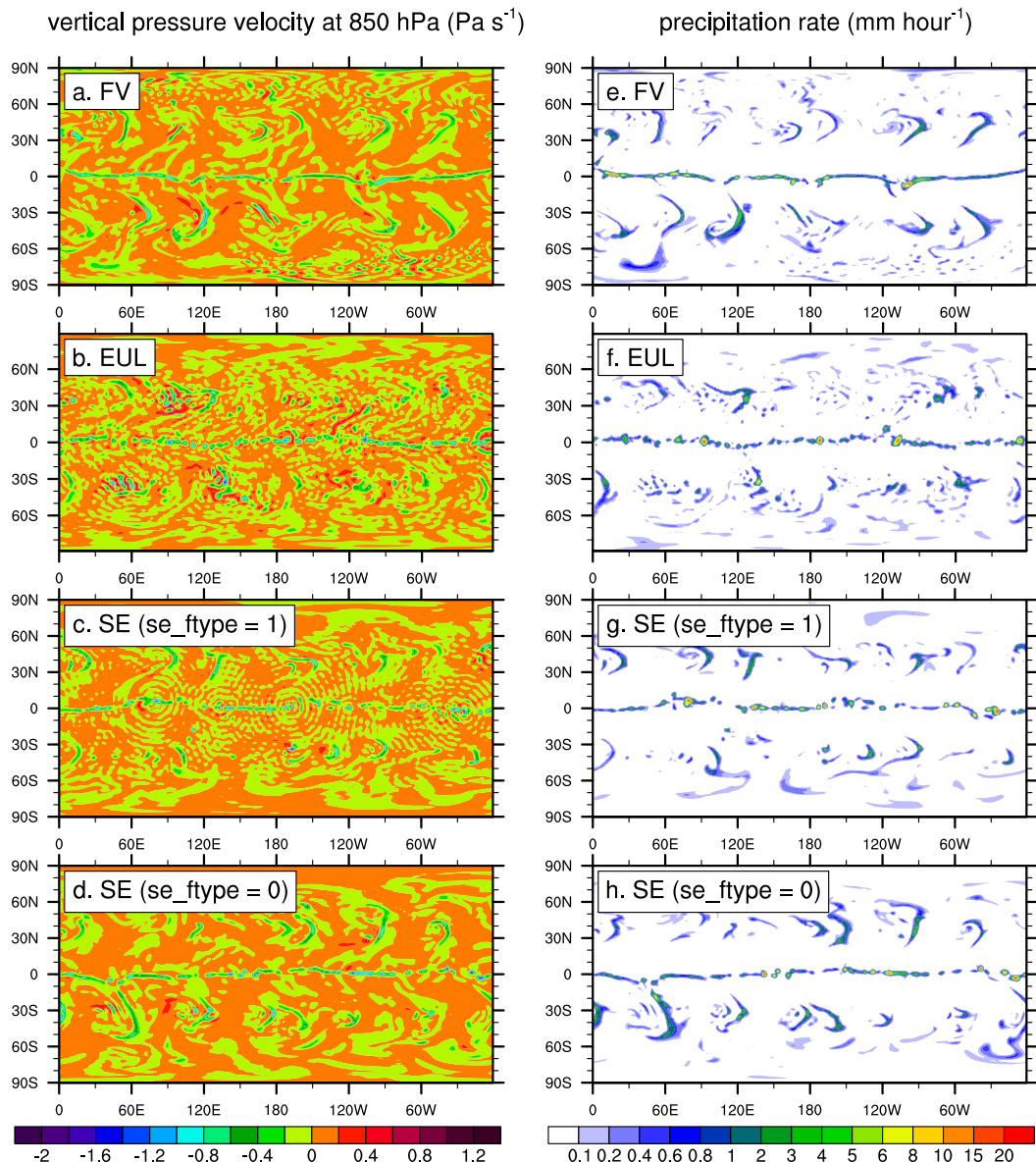


FIG. 5. Snapshots of instantaneous (left) 850-hPa vertical pressure velocities and (right) precipitation rates in MITC simulations. (a),(e) CAM-FV; (b),(f) CAM-EUL; and (c),(d),(g),(h) CAM-SE dynamical cores. (c),(g)  $se\_ftype = 1$  denotes a physics–dynamics coupling with the long physics time step; (d),(h)  $se\_ftype = 0$  couples with a subcycled, short dynamics time step. The physics time steps are 1800 (FV, SE) and 600 s (EUL); the dynamics time steps are 180 (FV), 600 (EUL), and 300 s (SE). In the case of SE with  $se\_ftype = 0$ , the forcing was gradually applied every 300 s. The EUL dynamical core is coupled to the physics in a process split (parallel) way; the SE and FV physics–dynamics coupling is time split.

EUL’s vertical pressure velocity field (Fig. 5b) and manifests itself as a noisy pattern (broken contours). The noise is even present in the midlatitudinal regions where organized precipitation bands should dominate. EUL’s shorter 600-s physics time step (in comparison to the 1800 s used in FV and SE) is not able to prevent these numerical Gibbs oscillations. In general, the smoothing mechanisms in dynamical cores need to be tuned. Overly strong damping

impacts the fluid flow in negative ways by overly smoothing strong gradients and local maxima in the moisture fields, which connects the physics and the dynamics.

### c. Aquaplanet assessments

An example of how full-physics aquaplanet simulations can give insight into the physics–dynamics interplay is shown in Figs. 6 and 7. The figures provide information

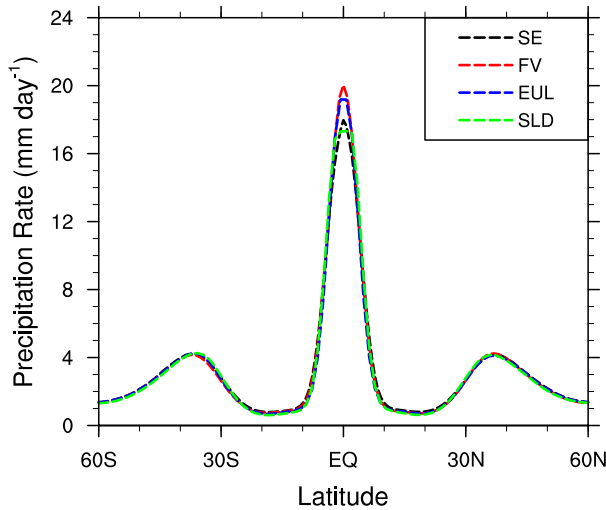


FIG. 6. The 2-yr-mean zonal-mean precipitation rate in four aquaplanet simulations with the CAM5 dynamical cores SE (111 km), FV (111 km), EUL (T85), SLD (T85), and the default CAM5 physics package.

about the shape of the ITCZ in CAM5 aquaplanet simulations with prescribed SSTs [CONTROL case in Neale and Hoskins (2000)]. As in section 4b, the CAM5 dynamical cores EUL, FV, and SE are assessed at the

resolutions T85 (EUL) and 111 km (SE, FV) with 30 levels. Also, the figures include the CAM5 spectral transform semi-Lagrangian (SLD) T85 dynamical core. All model simulations are run for 2.5 years, and the first 6 months are disregarded (spinup period). The models use the dynamics time steps 300 (SE), 180 (FV), 600 (EUL), and 1800 s (SLD), which are paired with the physics time steps 1800 (SE, FV, SLD) and 600 s (EUL).

The shape of the ITCZ in aquaplanet simulations has been a topic of debate for over a decade. Some models show a single equatorial peak of the ITCZ precipitation rate, whereas other models are characterized by a double ITCZ in the subtropics. Blackburn et al. (2013) even called the double ITCZ one of the “modern modeling mysteries.” The suggested mechanisms that govern the shape and strength of the ITCZ vary widely and are ambiguous. Williamson and Olson (2003) found dependence on the physics time step, the time stepping scheme, the dynamical core, and the strength of the horizontal diffusion. Mishra et al. (2008) discussed the ITCZ time step dependencies and physics changes. Rajendran et al. (2013) discussed the SST’s impact on the ITCZ, and Lee et al. (2003) and Möbis and Stevens (2012) investigated the role of the convection scheme. Williamson (2008) reported on the sensitivities to horizontal resolution, and Landu et al. (2014) discussed the

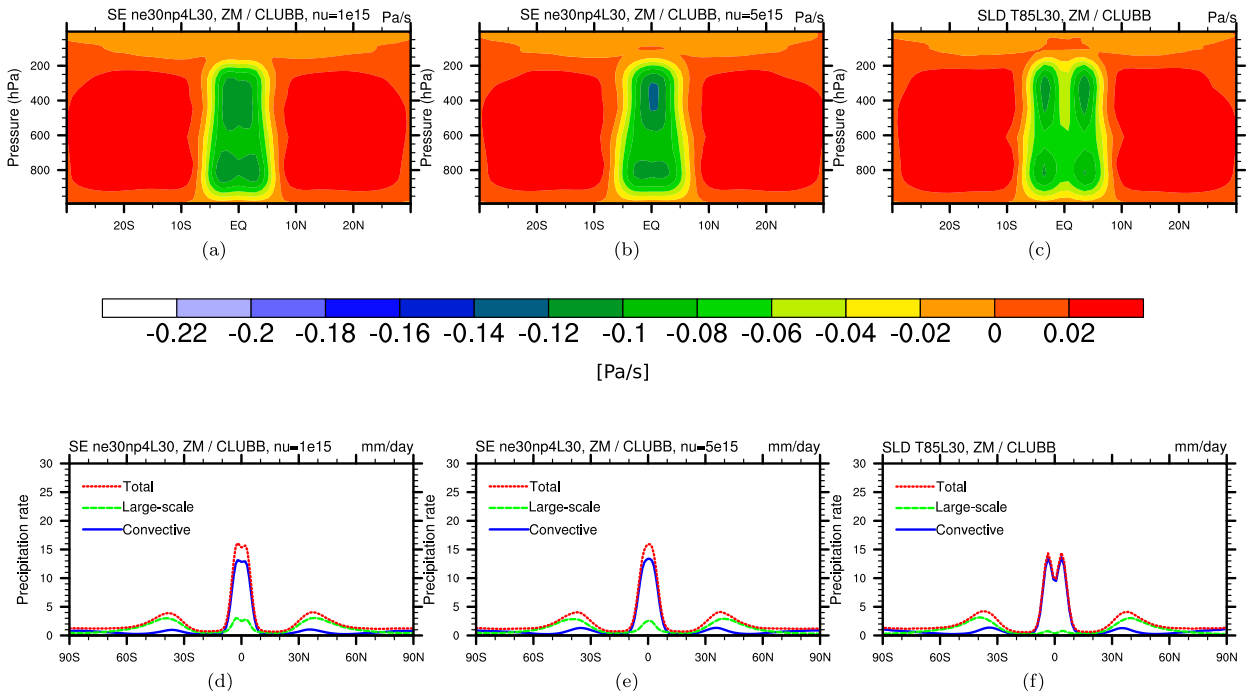


FIG. 7. Aquaplanet simulations with the alternative CLUBB PBL, macrophysics, and shallow convection schemes in CAM5. Latitude–pressure cross section of the 1-yr-mean zonal-mean vertical pressure velocity in the tropics for the dynamical cores (a) SE with  $K_4$  diffusion (hyperviscosity) coefficient  $1 \times 10^{15} \text{ m}^4 \text{ s}^{-1}$ , (b) SE with diffusion coefficient  $5 \times 10^{15} \text{ m}^4 \text{ s}^{-1}$ , and (c) SLD without explicit horizontal diffusion. (d)–(f) The 1-yr-mean zonal-mean precipitation rates of the three runs, split into total (red), large-scale (green), and convective (blue) precipitation.

ITCZ sensitivity to two dynamical cores, their resolutions, and strengths of the low-level moisture transports. More recently, [Medeiros et al. \(2015, 2016\)](#) compared the ITCZs in the aquaplanet configurations of models that participated in phase 5 of the Coupled Model Intercomparison Project (CMIP5) and provided an aquaplanet reference solution for NCAR's CAM5.3 model.

Four CAM5 dynamical core simulations were performed in aquaplanet mode that utilized the identical CAM5 physical parameterization package ([Neale et al. 2010b](#)). [Figure 6](#) shows that the time-mean (averaged over the last 2 years) zonal-mean precipitation rates in all four aquaplanet simulations are remarkably similar. They all show a single ITCZ and equatorial peaks that range between 17.5 and 20 mm day<sup>-1</sup>. This similarity is in sharp contrast to the assessments of [Blackburn et al. \(2013\)](#), who intercompared 16 different model simulations that participated in the Aquaplanet Experiment (APE; [Blackburn and Hoskins 2013](#)). The peaks in the APE models ranged from 10 to 34 mm day<sup>-1</sup> with an almost even split between single and double ITCZ models. Since the APE models are characterized by vastly different dynamical cores, resolutions, physical parameterizations, and coupling schemes, this makes it difficult to distinguish between causes and effects. Most of these differences in APE models are likely caused by different physical parameterizations. As shown in [Fig. 6](#), these effects reduce when a standardized set of parameterizations is used.

Here, a single aquaplanet framework is promoted as a “control environment” for idealized assessments of the physics–dynamics interplay. Another example is given in [Fig. 7](#), which intercompares the CAM5 SE (111 km) and SLD T85 dynamical cores with 30 levels when coupled to the alternative physical parameterization scheme CLUBB ([Golaz et al. 2002a,b](#); [Bogenschutz et al. 2012, 2013](#)). CLUBB replaces CAM5's default planetary boundary layer (PBL), macrophysics, and shallow convection schemes. The identical [Zhang and McFarlane \(1995\)](#) deep convection scheme and CAM5's microphysics scheme is still used. CAM5-SE/CLUBB is shown with two different settings of the fourth-order horizontal diffusion coefficient. [Figures 7a and 7d](#) depict the default diffusion coefficient  $1 \times 10^{15} \text{ m}^4 \text{ s}^{-1}$  for the 111-km grid spacing (labeled ne30np4). [Figures 7b and 7e](#) show the SE results with an increased diffusion coefficient of  $5 \times 10^{15} \text{ m}^4 \text{ s}^{-1}$ . The SLD T85 dynamical core ([Figs. 7c,f](#)) does not apply any explicitly added diffusion since its numerical scheme already provides sufficient implicit numerical diffusion. The simulations shown in [Fig. 7](#) are 1.5 years long, and the first 6 months are discarded (model spinup period). The physics and dynamics time steps for SE and SLD are the same as quoted before.

The top row of [Fig. 7](#) shows the latitude–pressure cross section of a 1-yr-mean zonal-mean vertical pressure velocity in the tropics for SE ([Figs. 7a,b](#)) and SLD ([Fig. 7c](#)). The bottom row presents the 1-yr-mean zonal-mean precipitation rates of the three runs, split into total, large-scale, and convective precipitation. The total precipitation rate can be directly compared to [Fig. 6](#). Two observations are striking. First, the switch to the CLUBB scheme causes the SE and SLD dynamical cores with default diffusion settings ([Figs. 7a,c,d,f](#)) to switch from the single ITCZ shown in [Fig. 6](#) to a double ITCZ structure. Second, the appearance of a weak double ITCZ structure in SE ([Figs. 7a,d](#)) is highly dependent on the choice of the horizontal diffusion coefficient. The increased diffusion coefficient in [Figs. 7b and 7e](#) impacts the moisture processes in a way that converts the weak double ITCZ in the default SE run to a single ITCZ peak. This brief assessment highlights the strength of an idealized testing framework to shed light on the physics–dynamics interactions. This approach can also be used to analyze the effects of different physics–dynamics coupling schemes.

## 5. Intramodel coupling

In this section, the focus is on intramodel coupling problems within the modeling system, where the coupling occurs via an exchange of boundary conditions that transmit fluxes through a physical interface (e.g., the ocean–atmosphere, land–atmosphere, ice–atmosphere, or ocean–sea ice interface). The land–atmosphere interaction—and in coastal areas, the ocean–atmosphere interaction—particularly affects weather models with their higher spatial resolution.

This problem is different from the scenarios discussed earlier for two main reasons. First, the coupling is between systems at different spatial locations rather than only different spatial scales at the same location. Second, the ocean and the atmosphere are usually implemented as separate submodels. Therefore, tight coupling at every step may not be practical.

Many distinct physical processes at different temporal and spatial scales, governed by different physical/conservation laws, must be simultaneously considered as a whole. This difficulty leads to intertwined physical, mathematical, and computational intricacies.

Algorithms to solve such coupled problems can be classified into two general categories:

- 1) Monolithic method: A single model representing all components to be coupled is defined. Each component has to be connected through one common space–time computational grid, which may be non-uniform, and connectivity may be established by

interpolation in space and/or time, and computational framework. The advantage is that a tightly coupled solution can be easily obtained. However, this approach is not tractable when trying to couple two individual models developed independently from each other with distinct numerical techniques, except for toy models (e.g., [Connors and Ganis 2011](#)). The monolithic approach has been used previously for land–atmosphere coupling when land surface processes were implemented as subroutines of GCMs and weather models, but it is currently abandoned to provide more modularity because of the increasing complexity of land surface models, which are now treated as external modules (e.g., [Polcher et al. 1998](#); [Ryder et al. 2016](#)).

- 2) Partitioned/split method: Analogous to operator splitting, the full problem is divided into smaller problems solved independently with boundary exchanges through their common interfaces (e.g., [Schulz et al. 2001](#); [Schmidt et al. 2004](#); [Large 2006](#)). This method is the most frequently adopted and most natural option in coupled problems arising in Earth system modeling. However, the difficulty is that this type of approach can give rise to various splitting errors and, thus, makes it difficult to recover a tightly coupled solution ([Keyes et al. 2013](#)). Analysis and attribution of these errors are not straightforward, as elaborated below. A comprehensive review of some interface-coupled multiphysics systems in a broad sense can be found in [Keyes et al. \(2013\)](#).

Coupled problems arising in Earth system modeling cover a broad range of aspects. Examples include parameterizations of turbulent boundary layers near interfaces, estimation of interfacial fluxes ([Schmidt et al. 2004](#); [Large 2006](#)), numerical space–time schemes, matching of different grids at the interface (e.g., [Best et al. 2004](#); [Balaji et al. 2007](#)), and coupling algorithms (e.g., [Lemarié et al. 2015](#); [Ryder et al. 2016](#); [Beljaars et al. 2017](#)). The complexity of software implementation is adding to the overall complexity of numerical models ([Valcke et al. 2012](#)), which are usually only considered on their own, neglecting connectivity.

In the present section, the partitioned approach is considered, and the example of the ocean–atmosphere coupling is used to illustrate the subtleties regarding physics/dynamics inconsistency inherent to intramodel coupling. The coupling between the atmosphere and the ocean is vital for forecasting on time scales of hours to weeks ([Smith et al. 2018](#)), even though, relative to the atmosphere, the ocean is changing rather slowly. Furthermore, most of the issues presented here are not only relevant to ocean–atmosphere coupling [see, e.g., [Schmidt et al. \(2004\)](#); [Ryder et al. \(2016\)](#) and references

therein for more specific details on sea ice–ocean or land surface–atmosphere coupling]. In the following, the theoretical limitations of coupling methods will be presented. Subsequently, some of the sources of error such as aliasing, synchronicity, and inconsistency are discussed in turn. This section concludes with a discussion of how the inconsistency and splitting errors can be reduced.

#### *a. Theoretical limitations of some of the current ocean–atmosphere coupling methods*

Most multiphysics coupling problems naively assume that all scales are resolved by the numerical models and that coupling is restricted to resolved scales. In the case of the ocean–atmosphere problem, the dynamical coupling is strongly influenced by physical parameterizations, which make rigorous mathematical analysis intractable.

The numerical ocean–atmosphere coupling problem is usually tackled in two different ways, as illustrated in the first two panels of [Fig. 8](#). The information flow between the two domains, atmosphere and ocean, is shown in the vertical. Time advances in the horizontal. The first method, where the exchange of instantaneous boundary data occurs at the largest time step of the two models, is referred to as synchronous coupling ([Fig. 8a](#)). The second is an exchange of averaged-in-time boundary data over a time interval  $[t_i, t_{i+1}]$ , which is much larger than the largest time step ([Fig. 8b](#)). The latter method is referred to as asynchronous coupling. Both are commonly termed loose coupling schemes (in contrast to tight coupling schemes, such as converged iterative schemes or implicit solves). These schemes correspond to only one iteration of an iterative process without reaching convergence ([Lemarié et al. 2014, 2015](#)). Hence, they do not strictly provide the solution to the ocean–atmosphere coupling problem, but an approximation of one since state variables of the two models are shifted by one time step or a sequence of time steps. The theoretical limitations of the synchronous and asynchronous methods are now explained further.

In the synchronous coupling algorithm, the following errors are observed:

- Aliasing errors: Significantly different time steps are used in each model (for the same horizontal resolution, the oceanic model is integrated with a time step approximately 10 times larger than the atmospheric model); as a consequence, aliasing problems may arise and compromise stability (e.g., [Schluter and Pitsch 2005](#)). Aliasing errors occur, for example, when an oscillatory forcing coming from one model may not be seen by the other model if the sampling is insufficient. It may be seen as a constant forcing if, for example, only the peaks are sampled.

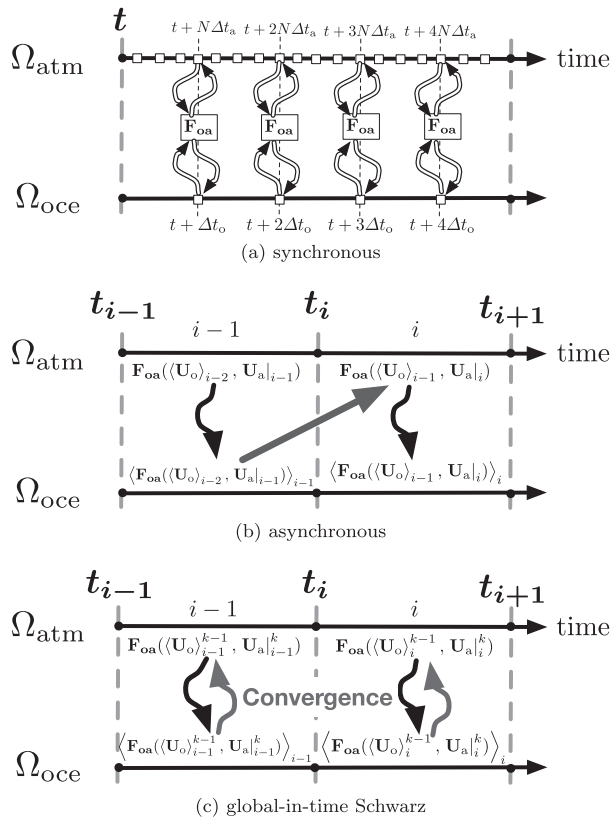


FIG. 8. Schematic view of the coupling between the computational domains of the atmosphere model  $\Omega_{\text{atm}}$  and ocean model  $\Omega_{\text{oce}}$ , with time advancing to the right. The function  $F_{\text{oa}}(\mathbf{U}_o, \mathbf{U}_a)$  represents the parameterization of air–sea fluxes with  $\mathbf{U}_o$  ( $\mathbf{U}_a$ ), the oceanic (atmospheric) state vector. Term  $\langle \cdot \rangle$  is a given time averaging operator, and  $\Delta t_o$ ,  $\Delta t_a$  the dynamical time step of the models such that  $N = \Delta t_o / \Delta t_a$ .

- **Synchronicity error:** Air–sea fluxes are used as boundary conditions for the vertical turbulent diffusion terms, which are treated implicitly in time, meaning that the fluxes at the interface are formally needed at time  $t + \Delta t$  and not  $t$  (Fig. 8a). The explicit exchange of data in the synchronous coupling leads to an additional condition for the coupling to be stable even if unconditionally stable time-stepping algorithms are used for vertical diffusion (Lemarié et al. 2015; Beljaars et al. 2017). A way to circumvent these stability issues is to consider a synchronous coupling with implicit data exchange. In practice, this approach amounts to solving the local implicit problems in the ocean and the atmosphere monolithically as one single implicit solver as often done for land surface–atmosphere coupling (Polcher et al. 1998; Ryder et al. 2016). Implicit flux coupling is so far seldom used in the context of ocean–atmosphere coupled models.
- **Physics–dynamics inconsistency error:** The uncertainties in the computation of air–sea fluxes at high

frequency through bulk formulations are huge [see discussion in section 2 of Large (2006) or Foken (2006)]. The sources of those uncertainties are numerous. Among them are the assumptions used to derive the continuous formulation of bulk formulas: for example, constant-flux layer assumption, horizontal homogeneity, quasi stationarity, and the fact that few direct measurements exist to calibrate those semiempirical formulations over the ocean. Moreover, the nonlinear problem associated with the estimation of bulk fluxes is often solved approximately. In practice, an averaging of the oceanic and atmospheric inputs to the bulk formulas should be required to minimize the uncertainty in the air–sea fluxes (Large 2006). An internally required time scale  $\Delta t_{\text{phys,req}}$  needs to be assumed for the parameterization scheme (bulk formulation) to be valid. Term  $\Delta t_{\text{phys,req}}$  is usually greater than the model dynamical time step  $\Delta t_{\text{dyn}}$ . As a result, using a synchronous method can render the model solution sensitive to the choice for the time step  $\Delta t_{\text{dyn}}$  since it is implicitly assumed that  $\Delta t_{\text{phys}} = \min(\Delta t_{\text{phys,req}}, \Delta t_{\text{dyn}})$ , which can lead to significant errors in the estimation of air–sea fluxes.

By construction, the asynchronous coupling is expected to mitigate this latter issue since boundary data averaged in time are exchanged over a time interval  $[t_i, t_{i+1}]$  usually much larger than the dynamical time step. However, the asynchronous coupling algorithm also suffers from a synchronicity issue. Indeed, the oceanic state used on  $[t_i, t_{i+1}]$  comes from the previous time window  $[t_{i-1}, t_i]$  and not the current time window. The lack of synchronicity is visible in Fig. 8b (oblique arrow). This error arises from the use of a noniterative partitioned coupling approach. The asynchronous coupling does not permit an accurate representation of transient processes on short time scales (e.g., the diurnal SST cycle), which is undesirable especially when the space–time resolution is increased. This approach is, however, still used in numerous coupled climate models, but research is currently in progress to minimize those synchronicity issues and allow correct phasing between the ocean and the atmosphere at a reasonable computational cost.

#### b. Reducing physics–dynamics inconsistency and splitting errors

Possible ways to reduce the errors mentioned above can be explored using the theoretical framework of the Schwarz-like domain decomposition methods. These methods are based on the original work of Schwarz (1870) and focus on subdividing the space domain into smaller domains. Over these domains, the equation

systems can be solved subject to particular boundary conditions [see Lemarié et al. (2013) for a recent example]. Here, the domains are not subdomains of one problem, (e.g., the heat distribution in a plate), but rather of the two different systems: ocean and atmosphere. The computational domain  $\Omega$  with  $\Omega = \Omega_{\text{oce}} \cup \Omega_{\text{atm}}$  is separated into subproblems on  $\Omega_{\text{oce}}$  and  $\Omega_{\text{atm}}$ , which can be solved separately. An iterative process is then applied to achieve convergence to the solution of the original problem. For the coupling of systems of partial differential equations (ignoring physical parameterizations), the converged solution obtained using the Schwarz algorithm is the same as the one obtained using a monolithic approach, within a given tolerance. The asynchronous coupling method corresponds to a single iteration of a global-in-time Schwarz method (Fig. 8c). In Fig. 8, only the global in time has iteration superscripts  $k$  because it is the only scheme that iterates. The prognostic variables are updated during the iteration procedure, and new fluxes are computed at each iteration. The asynchronous and synchronous schemes only exchange fluxes *once*, either at the same time (synchronous) or time offset (asynchronous). Time offset means in this specific example that the fluxes for the ocean at time  $t_i$  are computed from the atmosphere state at time  $t_i$ , and the atmosphere at time  $t_{i+1}$  sees the ocean fluxes from time  $t_i$ . Consequently, the synchronous coupling method corresponds to one single iteration of a local-in-time Schwarz method. The usual methods (e.g., synchronous and asynchronous coupling) used in the context of ocean–atmosphere coupling are thus prone to splitting errors because they correspond to only one iteration of an iterative process without reaching convergence.

So far, few studies have quantified the impact of these coupling errors on the coupled solutions. Connors and Ganis (2011) used highly simplified equations to show that a tight coupling algorithm leads to a reduced model uncertainty when compared to a loose coupling algorithm, in the sense that numerical solutions are more robust to perturbations in input parameters. This result is based on an uncertainty quantification method using stochastic input parameters for the exchange coefficients involved in the air–sea flux computation. In Lemarié et al. (2014), numerical experiments using the Weather Research and Forecasting (WRF) mesoscale atmospheric model coupled with the Regional Ocean Modeling System (ROMS) for a realistic simulation of a tropical cyclone were carried out. Ensemble simulations were designed that use perturbations of the coupling frequency and the initial conditions. One ensemble was integrated using the global-in-time Schwarz and another using the asynchronous method. The Schwarz iterative coupling method significantly reduced the ensemble

spread regarding cyclone trajectory and intensity, thus suggesting that a source of error is removed concerning the asynchronous coupling case, or some amplification mechanism (such as an instability) is reduced.

The results of Connors and Ganis (2011) and Lemarié et al. (2014) empirically emphasize a connection between the existence of splitting errors and model uncertainties. Indeed, in both studies, a tight coupling scheme provides a more reliable computation concerning perturbations (noise) in unknown input parameters, compared to a loose coupling scheme.

Physics–dynamics inconsistencies in the context of coupled problems are hard to estimate since there is a lack of idealized test cases with reference solutions including physical parameterizations. Such inconsistencies can arise from coupling algorithms or nonconformities in the space–time computational grids, but also from parameterization schemes for air–sea fluxes and turbulent boundary layers.

However, the mathematical formulation of those schemes is often devised semiempirically (i.e., by fitting independent measurements), and this can impair the smoothness, or differentiability, of the associated solutions (e.g., Burchard et al. 2005; Deleersnijder et al. 2008). This lack of smoothness and/or differentiability can then, in turn, give rise to the development and persistence of spurious oscillations in model solutions, also known as “fibrillations.”

This complexity has to be taken into account when designing mathematically consistent and efficient intramodel coupling algorithms. When an iterative coupling method is used, the coupled system of equations has to obey regularity and be well posed. If the system is not well posed and does not have regularity, then convergence is not guaranteed, and the relevance of the converged solution is questionable. For instance, the theoretical framework of the Schwarz methods could be used to derive intramodel compatibility/consistency constraints on the turbulent boundary layer parameterizations: a pair of parameterizations will be declared compatible if the associated iterative Schwarz algorithm converges. To investigate those issues, working on a simplified equation set to focus on specific problems should be encouraged.

## 6. Compatibility of parameterizations with the laws of thermodynamics

An important topic is the compatibility of the model formulation with the second law of thermodynamics (Gassmann and Herzog 2015). Goody (2000), Pauluis and Held (2002), Romps (2008), Bannon (2015), and Bannon and Lee (2017) raise the question of entropy

production in the classical sense for a numerically modeled atmosphere. This transfer can only be a reasonable endeavor if the model formulation reflects the second law of thermodynamics correctly. The compatibility of the model formulation with the first and second laws of thermodynamics is discussed in the following paragraphs, first for a dry atmosphere and then for a moist atmosphere.

### a. Dry atmosphere

For a dry atmosphere without radiation effects, the total energy, as the summation of all subenergies [Eqs. (B1)–(B4)], may only change by energy flux divergences. The resolved total energy of the model does not include turbulent kinetic energy (TKE). Therefore, the TKE, as a subgrid-scale energy, has to be counted as internal energy. The source terms of the TKE equation must be distributed to the other subenergy equations. The TKE dissipation term  $-\varepsilon_{\text{tke}}$  must appear in the internal energy equation and cancel with its counterterm.

The energy transfer due to shear production, often neglected in weather forecast models such as WRF, has only one logical route. A loss of resolved kinetic energy must be added in the role of frictional heating to the internal energy equation [Eq. (B1)]. For the buoyancy production or loss term  $\pm c_p \overline{\rho w'' \theta''} \cdot \nabla \Pi$ , this is not the case. Two alternative routes exist. The buoyancy production may be distributed to either the resolved kinetic energy or the internal energy equation. For the second law of thermodynamics to hold, energy has to be dissipated. Hence, energy should always be converted to internal energy. Therefore, for positive buoyancy production, energy is converted into internal energy, with a corresponding buoyancy loss term [Eq. (B10)] appearing in the resolved kinetic energy [Eq. (B3)]. Negative buoyancy production, in turn, is lost from the internal energy to unresolved turbulent eddies. In consequence, the buoyancy loss term must be transferred to the internal energy [Eq. (B1)]. This implementation then results in a scheme where dissipation means that energy ends up in the internal subenergy budget, which comprises both the original internal energy and the turbulent kinetic energy of the subscale eddies.

For unstable stratification [Eq. (B5)] and stable stratification [Eq. (B7)], the internal energy equations differ [cf. Eqs. (B6) and (B8)]. The associated entropy budget equations for unstable and stable stratification [Eqs. (B11) and (B12), respectively] contain different internal entropy production terms. These internal entropy production terms have to be independently positive definite (de Groot and Mazur 1984). This independence is required for formal compatibility with the second law of

thermodynamics (Zdunkowski and Bott 2004, p. 104). Turbulent fluxes computed from fluctuations are fundamentally different than subgrid-scale fluxes. Subgrid-scale fluxes must obey the second law (Gassmann and Herzog 2015). The subgrid-scale shear production term must be positive, and the form of the friction tensor is required such that  $-\overline{\rho \mathbf{v}'' \mathbf{v}''} : \nabla \hat{\mathbf{v}} > 0$ . This requirement is fulfilled by a momentum flux tensor built up from shear and strain deformations. For the buoyancy flux terms to yield positive-definite entropy production rates, they must be formulated as downgradient fluxes proportional to  $-\nabla \hat{T}$  in (B11) and  $-\nabla \hat{\theta}$  in (B12).

For unstable stratification,  $\partial_z \hat{T}$  and  $\partial_z \hat{\theta}$  have the same direction; both are decreasing with height. The internal entropy production term in (B11) is positive for a downgradient potential temperature flux. The vertical buoyancy flux might be counter to the local gradient of potential temperature in the upper part of a convective boundary layer. The energy supply for upward mixing originates from the subgrid-scale eddies losing their buoyancy. A flux formulation according to  $c_p \overline{\Pi \rho w'' \theta''} = -c_p \overline{\Pi K^\theta} (\partial_z \hat{\theta} - \gamma)$  is then adequate. For a given  $K^\theta$  and  $\gamma$  from an arbitrary parameterization, the second law of thermodynamics requires  $K^T$  to be positive. This requirement can be derived from the relation  $-c_p \hat{\rho} K^T \partial_z \hat{T} = -c_p \overline{\Pi K^\theta} (\partial_z \hat{\theta} - \gamma)$ . The countergradient flux is therefore not violating the second law at the top of a convective boundary layer.

A consequence of (B6) for stable stratification is a corresponding work term in the resolved kinetic energy [Eq. (B9)]. Hence, the vertical velocity equation gains an additional subgrid-scale term:

$$\partial_t \hat{w}|_{\text{sub}} = -c_p \frac{\overline{\rho w'' \theta''}}{\hat{\rho} \hat{w}} \partial_z \Pi \approx -\frac{K^\theta N^2}{\hat{w}}, \quad (2)$$

which becomes formally singular for  $\hat{w} = 0$ . In this limit, the kinetic energy of vertical motions is zero, and hence there is no conversion into internal energy. Therefore, the diffusion coefficient  $K^\theta$  must be defined such that it vanishes for vanishing vertical wind, leading to the approach  $K^\theta \propto \hat{w}^2$  and the appearance of a Rayleigh damping term in the vertical velocity equation

$$\partial_t \hat{w}|_{\text{sub}} = -K^\theta N^2 / \hat{w}. \quad (3)$$

The task of the parameterization is then to determine the diffusion coefficients. The momentum diffusion coefficients  $K^m$  and  $K^\theta$  are no longer connected via a Prandtl number  $P_r$  of  $\mathcal{O}(1)$ .

Idealized 2D numerical experiments have been performed with the ICON-IAP model (Gassmann 2013) to contrast the second-law-compliant and second-law-violating

formulations. In these, breaking gravity waves were simulated at a critical layer in the mesosphere. The undulation of the isentropes for breaking gravity waves is always such that their trough positions coincide with vanishing vertical wind. Hence, at such a trough position, the diffusive buoyancy flux is zero, and the isentropes are no longer pushed down as would be the case if the conventional approach [Eq. (B6)] were used with  $P_r = K^m/K^\theta = \mathcal{O}(1)$ . Breaking waves may not be amplified as would be the case in a conventional parameterization. Figures 7a and 7b in Gassmann (2018) demonstrate that a classical, second-law-violating parameterization can lead to wave amplification and manifestation. The waves are visibly stronger and smaller in the horizontal scale. The second-law-compliant parameterization, in turn, leads to wave attenuation.

### b. The inclusion of moisture-related quantities

The first law of thermodynamics defines the governing equations for a moist atmosphere (Bannon 2002; Zdunkowski and Bott 2003; Wacker and Herbert 2003; Wacker et al. 2006; Catry et al. 2007; Gassmann and Herzog 2015). Thermodynamic properties such as density, the gas constant, or the specific heat of the air–cloud–precipitation mixture may no longer be approximated by the properties of dry air. Also, the barycentric velocity  $\mathbf{v} = \sum_i \mathbf{v}_i \rho_i / \rho$ , where  $i =$  denotes dry air, water vapor, rain, snow, and other species, may differ from the velocity of dry air when a significant amount of condensate is present. Such details contribute to the variability of predicted extreme regional events, such as heavy precipitation. Geleyn and Marquet (2011) and Bacmeister et al. (2012) have demonstrated this for the degree of approximation of the gas constant for moist air. In the governing equations, a constant temperature is assumed throughout the air parcel, which means falling precipitation has the same temperature as its environment. Bannon (2002) discussed and estimated the small and negligible spurious heating of the atmosphere due to this assumption.

The energetically consistent equations for a moist atmosphere lead to a modification of the entropy budget [Eq. (B11) or (B12)]. Virtual potential temperature replaces potential temperature, and more dissipative processes with corresponding internal entropy production rates are present. Gassmann and Herzog (2015) follow de Groot and Mazur (1984) and find those additional entropy production rates as

$$\partial_t(\bar{\rho}\hat{s}) = \dots - \sum_i \mathbf{J}_i \cdot \nabla \hat{\mu}_i |_{\hat{T}} / \hat{T} - \sum_i I_i \hat{\mu}_i / \hat{T}, \quad (4)$$

where  $\mathbf{J}_i$  with  $\sum_i \mathbf{J}_i = 0$  are the turbulent and diffusive fluxes,  $I_i$  are the source terms for a constituent  $i$  originating from phase transitions, and  $\mu_i$  is the chemical potential of constituent  $i$ . The first term on the rhs of

Eq. (4) describes irreversible mixing, and the second describes irreversible phase transitions.

The turbulent mixing of dry air and water vapor comprises opposite fluxes of dry air and water vapor  $\mathbf{J}_v^t = -\mathbf{J}_d^t$ . Consequently, the internal entropy production term reads  $\mathbf{J}_v^t \cdot (\nabla \hat{\mu}_d |_{\hat{T}} - \nabla \hat{\mu}_v |_{\hat{T}}) > 0$ . The gradient of the chemical potential of a constituent at constant temperature is proportional to the gradient of its partial pressure  $\bar{\rho} q_i \nabla \hat{\mu}_i |_{\hat{T}} = \nabla \bar{p}_i$ . Positive entropy production can only be guaranteed with a turbulent water vapor flux formulated as

$$\mathbf{J}_v^t = -\bar{\rho} K^v (\hat{q}_d \nabla \hat{p}_v - \hat{q}_v \nabla \bar{p}_d) / \bar{p} \neq -\bar{\rho} K^v \nabla \hat{q}_v. \quad (5)$$

The inequality on the rhs with  $\nabla \hat{q}_v$  turns into equality if it is assumed that water vapor and dry air have the same gas constant. Not including the additional entropy production rates detailed above would only be compatible with the second law of thermodynamics if the water vapor were treated as a passive tracer with the same gas constant as dry air.

The mixing entropy also reveals internal entropy production due to liquid or frozen precipitation. Liquid and frozen constituents have  $\nabla \hat{\mu}_i |_{\hat{T}} = 0$ . The flux control condition  $\sum_i \mathbf{J}_i^d = 0$  requires upward fluxes of the nonsedimenting air constituents (i.e., dry air and moisture) with a speed  $w^{\text{ns}}$ . The fluxes of nonsedimenting constituents lead thus to the internal entropy source of

$$\begin{aligned} \partial_t(\bar{\rho}\hat{s}) &= \dots - (\mathbf{J}_d^d \cdot \nabla \hat{\mu}_d |_{\hat{T}} + \mathbf{J}_v^d \cdot \nabla \hat{\mu}_v |_{\hat{T}}) / \hat{T} \\ &= -w^{\text{ns}} \partial_z \bar{p} / \hat{T} = w^{\text{ns}} \bar{\rho} g / \hat{T} > 0. \end{aligned} \quad (6)$$

The importance of the existence of the vertical diffusive fluxes of nonsedimenting constituents in the governing equations becomes obvious. A consistent entropy budget equation cannot be formulated without them.

The internal entropy production due to phase changes is given by

$$\partial_t(\bar{\rho}\hat{s}) = \dots - I_{lf} (\hat{\mu}_{lf} - \hat{\mu}_v) / \hat{T}, \quad (7)$$

where  $I_{lf}$  is the source of the liquid/frozen component. The differences between the chemical potentials are found to be  $\hat{\mu}_{lf} - \hat{\mu}_v = -R_v \hat{T} \ln \mathcal{H}$ , where  $\mathcal{H}$  is the relative humidity concerning water/ice saturation. Entropy is produced if water evaporates at subsaturation or if water vapor condenses at supersaturation. For a quasi-static process at saturation  $\mathcal{H} = 1$ , the entropy production is zero, and the process is reversible. A saturation adjustment scheme in a numerical model removes sub- or supersaturations *immediately*. This numerical approximation to a quasi-static process yields a slightly positive nonzero entropy production.

All subscale terms produce entropy, and their entropy sources may be diagnosed. The requirement of positive internal entropy production specifies the direction of the diverse fluxes, but not their amount. The latter is the task of the physics parameterization. Parameterizations of convection are in fact a combination of heat fluxes, constituent fluxes, and phase changes. Each of these fluxes on its own contributes to entropy production.

## 7. The gray zone

As the resolution of geophysical models increases, the separation between the scales that are resolved by the model and the scales of the subgrid processes that are parameterized, approximately 1–10 km for convective and a few to several hundred meters for the PBL/turbulence parameterization, vanishes. When a subgrid process that is targeted by parameterizations at a lower resolution becomes partially resolved at a higher resolution, the model runs at a resolution in what is called the *gray zone* of this process: the explicit and the parameterized representations of a process are in “competition” in the numerical model. The result of this competition may be double counting or no counting at all. The gray zone is a particularly timely problem for weather models, which currently operate at a resolution precisely in this regime.

### a. Examples in current model configurations

The continuous resolution increase over the last 50 years has brought global models close to the gray zone of convection. Limited area models for numerical weather prediction (NWP) have already jumped across the gray zone of convection, and they are now on the verge of the gray zone of turbulence (Wyngaard 2004; Boutle et al. 2014; Honnert and Masson 2014).

In the gray zone of a process, it is not accurately represented by its subgrid representation in a parameterization or the explicit representation through the gridscale model variables. In practice, modelers employ a combination of three corrections. The first is to tune the existing parameterizations to extend their usage out of the range of validity of their fundamental hypotheses. The second is to switch off the parameterizations, even if the process is not yet well resolved but only “permitted” by the resolution. Third, modelers apply ad hoc numerical filters, if necessary, to control the intensity of the process.

A recent example in the operational ECMWF model showed the difficulty of balancing the explicit and the parameterized representations of deep convection, even at a grid spacing of about 16 km, which is not typically considered to be in the gray zone. When the convection scheme was modified to improve the daily cycle of convection (Bechtold et al. 2014), explicit convective

clouds at isolated single grid points were diagnosed in calm conditions near mountainous and moist areas, leading locally to unrealistic precipitation (Fig. 9a). This new version of the convection scheme then delayed the onset of the parameterized convection toward the evening. The CAPE accumulated such that in a region with weak orographic forcing of moist air in a low-shear environment, an explicit convective cloud is permitted at a single grid point before the convection scheme is triggered. In the IFS, such single-gridpoint structures are then pathologically amplified by the semi-Lagrangian advection scheme of the IFS dynamics (Malardel and Ricard 2015). The resulting unrealistic explicit deep convective clouds may last for several hours, leading to spurious high precipitation rates at some grid points. Similar gridpoint storms have been reported in the literature for other global models: for example, Williamson (2013) in CAM4, with T340 spectral truncation and a 5-min time step (section 2) or in mesoscale limited-area models at resolutions in the 3–5-km range (Malardel and Ricard 2015). This example shows that explicit deep convective circulations are permitted at resolutions that are far too coarse to sample individual convective ascents in circumstances where the convection scheme is not triggered soon enough to release the CAPE. On the other hand, with the old version of the convection scheme, the parameterization was triggered earlier, and the onset of the convection in the tropics was systematically too early. Finding the right balance between the explicit and the parameterized representations of convection everywhere around the globe becomes even more difficult in the gray zone of convection.

### b. Model limitations in the gray zones

The prognostic equations that are solved by a discrete numerical model are the result of time and space filtering. This filtering creates an artificial cutoff in the continuous atmospheric spectrum between the processes that are represented by the gridscale variables, which constitute a time–space mean, and the processes that are supposed to be subgrid and whose effect on the larger scales is parameterized.

This cutoff scale is partly defined by the time–space resolution of the model and partly by the characteristics of the numerical schemes and physical parameterizations. In most numerical schemes, the largest errors are expected to happen at the cutoff scale, especially in regions of large gradients. Weaknesses of the numerical schemes such as substantial explicit diffusion, large phase shift, or nonconservation then directly affect the energy-containing circulation near this cutoff scale. Thus, as discussed by Lander and Hoskins (1997), physical parameterization should not force and should

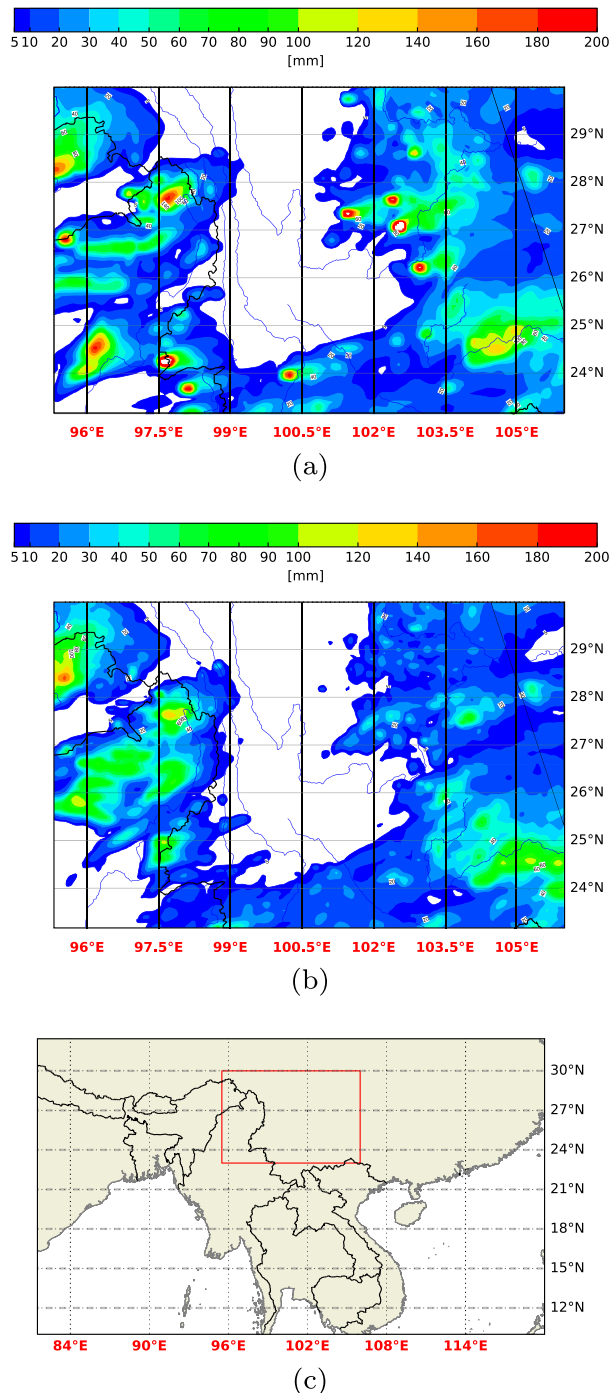


FIG. 9. Operational ECMWF forecast with a spectral truncation T1279 (a) 16- and (b) 9-km reduced Gaussian grid. Three-day accumulated surface large-scale precipitation for forecasts starting at 0000 UTC 20 May 2015 valid at 0000 UTC 23 May 2015. (c) Study area marked with red square.

not be forced by the gridscale model variables containing variance at the grid scale. The test case shown in Fig. 9 illustrates this statement. With the horizontal resolution upgrade at the beginning of 2016, the IFS

moved from a linear grid to a cubic grid, keeping the same spectral truncation T1279. With the cubic grid, the smallest wavelength of the truncation is now represented by four points instead of two with the linear grid. Such a pairing between the spectral representation of the IFS and the model grid improves the scale separation between the gridscale prognostic model variables and the subgrid effect computed in the physics package. In the linear grid, the separation between resolved scales and parameterized scales is two grid lengths. In the cubic grid, this separation is now increased to four grid lengths. The cubic grid also ensures that the marginally resolved scales are handled sufficiently accurately. In particular, ascents that are resolved by a single grid column do not occur anymore with a cubic grid. The development of gridpoint storms is then eliminated from the IFS forecast (Fig. 9b).

Indeed, the formulation of most physical parameterizations is based on the scale separation, both in time and space, between a resolved environment and the parameterized processes, which are treated as perturbations of the environment. The formulations are derived from a statistical evaluation of the impact of a large population of perturbations on the resolved flow, sometimes simplified by a bulk representation of the process: for example, in many convection schemes, a single convective cloud replaces a population of smaller cloud ascents. But, when the resolution increases, the grid becomes too small for a population of deep convective circulations to develop inside a grid box. In the gray zone of convection, the updrafts could cover a large fraction of the gridbox area, and then the mean gridbox properties that are carried by the gridscale variables of the model should depart substantially from the updraft environment. The detrained material from the updrafts should also not be confined in the same grid column, but should be distributed over several grid columns (section 3a; Fig. 3). However, the Reynolds decomposition that is used to derive the eddy diffusivity formulation for 1D turbulence or the mass flux formulation of most convection schemes does not allow any net mass transport by the perturbations in a grid box. Here, updraft and downdraft have to cancel in the same grid box, rendering the problem of extending the detrainment to neighboring cells challenging to generalize (section 3a).

The equilibrium hypothesis (Arakawa and Schubert 1974) resulting from the hypothesis of the scale separation in time also starts to collapse when the time step of the model decreases. With an increase of resolution in time, the variability of the model variables becomes faster than the characteristic convective time scales (Gerard and Geleyn 2005). If the closure of the convection scheme is too simple, spurious explicit convective storms are

more likely to develop at high resolution (section 2c; see also Williamson 2013; Gerard 2015).

### c. Toward scale-aware parameterizations

Efforts to create scale-aware convective parameterization started in the limited-area model community more than 10 years ago (Gerard and Geleyn 2005) and are now shared by a much larger community (Kuell and Bott 2008; Arakawa and Wu 2013; Gustafson et al. 2013; Grell and Freitas 2014; Siebesma 2015). The following paragraphs will illustrate the transition from cloud-system-resolving models (CSRMs) to scale-aware parameterizations of convection. Parallels can be drawn to the problem of large-eddy simulation and turbulence parameterization. This transition would be of particular interest for high-resolution limited-area models (e.g., in an NWP context) who, due to their high resolution, already allow convection.

One of the main issues for the parameterization of deep convection in the gray zone is that when the resolution of the model increases, some of the condensates can be detrained across the grid box; the ensuing compensating subsidence should take place within a set of grid boxes, and the convective updraft grid box may not necessarily be part of that set. With the time step organization of NWP codes, the horizontal transport across the grid boxes can only be handled by the advection of the dynamical core.

Piriou et al. (2007) observed that the advantage of CSRMs with respect to parameterized budget equations is that the source terms for the convection can be separated into transport terms and microphysics terms, and they argued that the two types could be treated independently. Moreover, if the condensation (and the cloudy evaporation) terms in cloud budgets are computed by a microphysics scheme and provided as source terms to the environment, then the system can be closed, leading to CSRM-type equations that still do not contain explicit detrainment terms. In that case, there is no need to rely on the budget equations to close the system directly.

However, to go from CSRM to gridbox parameterizations, it is necessary to partition the grid box into a convective and a nonconvective part. Gerard et al. (2009) used the cloud scheme of Smith (1990) and Xu and Randall (1996) to introduce protection of the cloud condensates in the convective part to prevent their evaporation by the cloud microphysics scheme. Additionally, Gerard et al. (2009) used a prognostic formulation of the convective mesh fraction of the updraft and a prognostic equation for the updraft vertical velocity proposed in Gerard and Geleyn (2005). The result is a CSRM-type set of equations without any explicit

presence of detrainment terms. In other words, it interacts with the dynamics in the same manner as a CSRM-type model does.

One can argue that bulk parameterizations should converge in their behavior to the behavior of CSRM in the cloud-resolving limiting resolutions. If the prognostic equations of the mesh fraction and the updraft vertical velocity scale correctly, then the equations should converge to the equations of a CSRM. This prognostic formulation yields a mechanism to control this convergence and to formulate a scale-aware parameterization of deep convection.

This approach was implemented in a scheme called the Modular Multiscale Microphysics and Transport scheme (3MT), and it formed the basis of the so-called ALARO-0 configuration of the ARPEGE-Aire Limitée Adaptation Dynamique Développement International (ALADIN) system. Gerard et al. (2009) showed satisfactory results of this scheme with resolution ranging from the mesoscale down to 4 km (their Fig. 11). In that figure, it can be seen that without 3MT, the model did not resolve the organized convection satisfactorily. Only a few small intense gridpoint storms were resolved.

Recently, good results were found with an updated version of the scheme up to a grid spacing of about 1 km. De Meutter et al. (2015) tested a version of the 3MT scheme that included the parameterization of unsaturated downdrafts. They found downdraft mass fluxes that are sufficiently realistic so that they can be used operationally to forecast downbursts. De Troch et al. (2013) demonstrated that the ALARO model has an improved multiscale character, compared with the former ALADIN configurations (Termonia et al. 2018).

These efforts still need to be generalized for global NWP. The different types of convective circulations, deep and shallow convection, in the tropics and at higher latitudes, have to be well represented for medium-range weather forecasting. Recent results with variable resolution grids (Müller 2014) also show the need for scale-aware physics across the problematic range between 1 and 10 km.

Limited-area models with subkilometer resolutions do not use any parameterization of deep convection, but the parameterization of eddies in the boundary layer is still needed. A blending between a 3D turbulence parameterization designed for large-eddy simulation and a 1D boundary layer parameterization suitable for coarser grid resolution has been shown to be beneficial to the representation of clear or stratocumulus-topped boundary layers by Boutle et al. (2014). In this case, the transition laws developed by Honnert and Masson (2014) are used. The transition law defines a threshold for the required dimensionality of the turbulence scheme depending on

the wind shear, the resolution normalized by the boundary layer height, and the depth of the cloud layer. This law then drives the transition from unresolved to resolved turbulence seamlessly. But more efforts are needed to generalize this approach to any regime in the boundary layer.

Malardel and Wedi (2016) identify the influence of subgrid-scale parameterizations for the shape of the kinetic energy spectra, as well as for the nonlinear spectral fluxes at all scales. The artificial scale separation between resolved and subgrid processes modifies the natural turbulent energy cascade. When the processes are parameterized, the circulation that is responsible for the average effect of the subgrid mixing is neither part of the resolved kinetic energy spectra nor part of the nonlinear spectral transfer, thus effectively disabling any energy cascade. Subgrid-scale circulations are not involved in the resolved energy cascade due to nonlinear interaction between scales. Hence, the parameterization directly feeds the large scales, bypassing the natural cascade.

The temptation to enable the natural cascade by eliminating a particular parameterization too early in a gray zone is, however, risky as the model balances change at all scales as a result. Such practice may also have implications on the forecast error growth, as the predictability time of a  $k^{-3}$  system can be much longer than that of a  $k^{-5/3}$  system (Rotunno and Snyder 2008; Palmer et al. 2014). However, it is unclear if a growing error is merely replaced by a much larger error injected at multiple scales when the process is parameterized.

## 8. Emerging challenges

The ecosystem of models is continuously evolving, and new methods become available and feasible, replacing older and often somewhat simpler technologies. Currently, the advent of high-order finite element methods offers many more choices to the coupling than a gridpoint model would. Likewise, spatially varying resolution and/or adaptive refinement is used more and more often, partly due to the availability of mimetic methods that support this sort of models. The spatially varying resolution, however, is not without challenges to the coupling of the multiple scales now present in the model.

### *a. Spatial physics–dynamics coupling with element-based high-order Galerkin methods*

Numerical methods using element-based high-order Galerkin discretization (e.g., Durran 2010) have reached a level of maturity in which they are being considered for next-generation weather and/or climate models. For example, the spectral-element dynamical core in NCAR's CAM (Neale et al. 2010b), referred to as CAM-SE (Taylor

et al. 2008; Taylor and Fournier 2010; Dennis et al. 2012), is currently being used for high-resolution climate modeling (e.g., Small et al. 2014; Giraldo and Restelli 2008; Nair et al. 2009; Brdar et al. 2013). In principle, the discussion applies to any element-based high-order Galerkin method. In the following, the focus is on CAM-SE.

Element-based high-order Galerkin methods typically apply quadrature rules to integrate basis functions over a reference element to advance the solution to the equations of motion in time. The choice of quadrature rule is application dependent and can have consequences for the properties of the final algorithm, in particular, algorithm efficiency. In CAM-SE, Gauss–Lobatto–Legendre (GLL) quadrature is used, which accurately integrates Lagrange polynomials up to degree  $2p - 1$ , where  $p + 1$  is the number of quadrature points. For an introductory discussion on emerging Galerkin methods in the context of atmosphere modeling, see Nair et al. (2011).

Irrespective of the choice of quadrature rule, the quadrature points for higher-order methods are not equally spaced over the sphere and reference element. The higher the order, the more the quadrature points tend to cluster near the sides and, in particular, the corners of the elements. As far as the authors are aware, current dynamical cores employing element-based high-order Galerkin methods use the quadrature point values for the state of the atmosphere passed to subgrid-scale physical parameterizations. This approach follows the traditional model setup where physics and dynamics grids coincide. One may question if that is an appropriate choice for the element-based high-order Galerkin methods. Physical parameterizations expect a state of the atmosphere representative of the area for which it should compute tendencies (e.g., a gridcell-averaged state of the atmosphere). The quadrature point values are representative of the state of the atmosphere at the quadrature point and in the vicinity of the quadrature point, but what area is associated with the quadrature point value? An irregular grid results if the areas around the quadrature points are defined, such that the spherical area exactly matches the GLL quadrature point weight times the metric factor. Hence, the state of the atmosphere passed to physics is sampled anisotropically and inhomogeneously in space.

Assuming that physics should be given a gridcell average value, it may be more consistent to integrate the basis functions within each element over quasi-equal-area control volumes. From an implementation point of view, it is convenient to have the control volumes subdivide the element so that no control volume spans part of the neighboring elements. Note that the basis functions are  $C^\infty$ , infinitesimally differentiable, within each

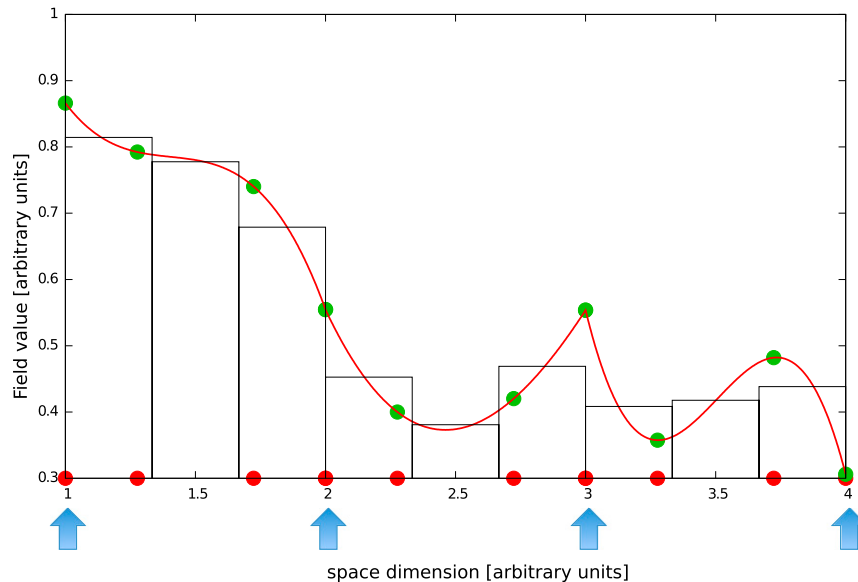


FIG. 10. Element polynomials in one dimension. The figure shows three elements. The edges of the elements are marked with blue arrows. The red curves are the degree 3 polynomials in each element, and, following the CAM-SE algorithm, the polynomial values from each side of an element boundary are averaged. The filled green circles show the GLL quadrature point values, and the red filled circles are the locations of the GLL quadrature points in each element for  $np = 3$ . The histogram bar shows the cell-averaged values on an  $nc = 3$  physics grid (each element has been divided into three equal-sized control volumes) obtained by integrating the Lagrange basis functions over the control volumes.

element but only  $C^0$ , which may be discontinuous, at the element boundaries. If there is a strong gridscale forcing at the element boundary, the physics grid value may be more representative than the extrema value. Figure 10 shows such an example where the boundary edge values are large. However, the physics-grid-averaged value is not. Hence, the boundary edge values are outliers. It would not seem reasonable to force the dynamics with the edge value (at the third blue arrow from the left) as it is not an accurate representation of the overall forcing. This configuration, where physics and dynamics grids are separated, is referred to as *physgrid*. Care must be taken when mapping variables to and from dynamics and physics grids so that conservation properties are not violated. For CAM-SE, the arbitrary high-order, conservative, and consistent remapping algorithm of Ullrich and Taylor (2015) is used. The algorithm consists of matrices that can be precomputed: for mapping from the dynamics to the physics grid, it consists of one matrix that performs a shape-preserving, but low-order, remap and another matrix that is not shape preserving but is high order. The algorithm has been modified such that the two matrices in each element are optimally combined linearly so that the method is shape preserving and, where possible, high order. For mapping the tendencies back to the GLL quadrature grid, a low-order

conservative and shape-preserving method is used. The mapping algorithm accommodates any order of basis functions. Ideally, the map should be reversible and shape preserving at the same time. That, however, seems unattainable.

The next step is the choice of physics grid spacing. Three options exist. The grid spacing can be the same in dynamics and physics; it can be smaller or larger in the physics. Lander and Hoskins (1997) argued, in the context of a spectral transform model, that the physical parameterizations should only be given what they termed “believable,” well-resolved scales. From linear theory, it is well known that numerical methods used in the dynamical core do not resolve the shortest wavelengths (e.g., the  $2\Delta x$  wave) accurately. Physical parameterizations should not be passed scales that, from linear theory, are not accurately represented. On the other hand, computing physics tendencies on a higher-resolution grid compared to the dynamical core may provide a better sampling of the atmospheric state, somewhat similar to the subcolumns concept (Pincus et al. 2003; Barker et al. 2008; Thayer-Calder et al. 2015).

In this section, the consequences of separating physics and dynamics grids in CAM-SE, as described above, are explored. The 1° version of CAM-SE is used in the ne30np4 configuration ( $30 \times 30$  elements in each panel,

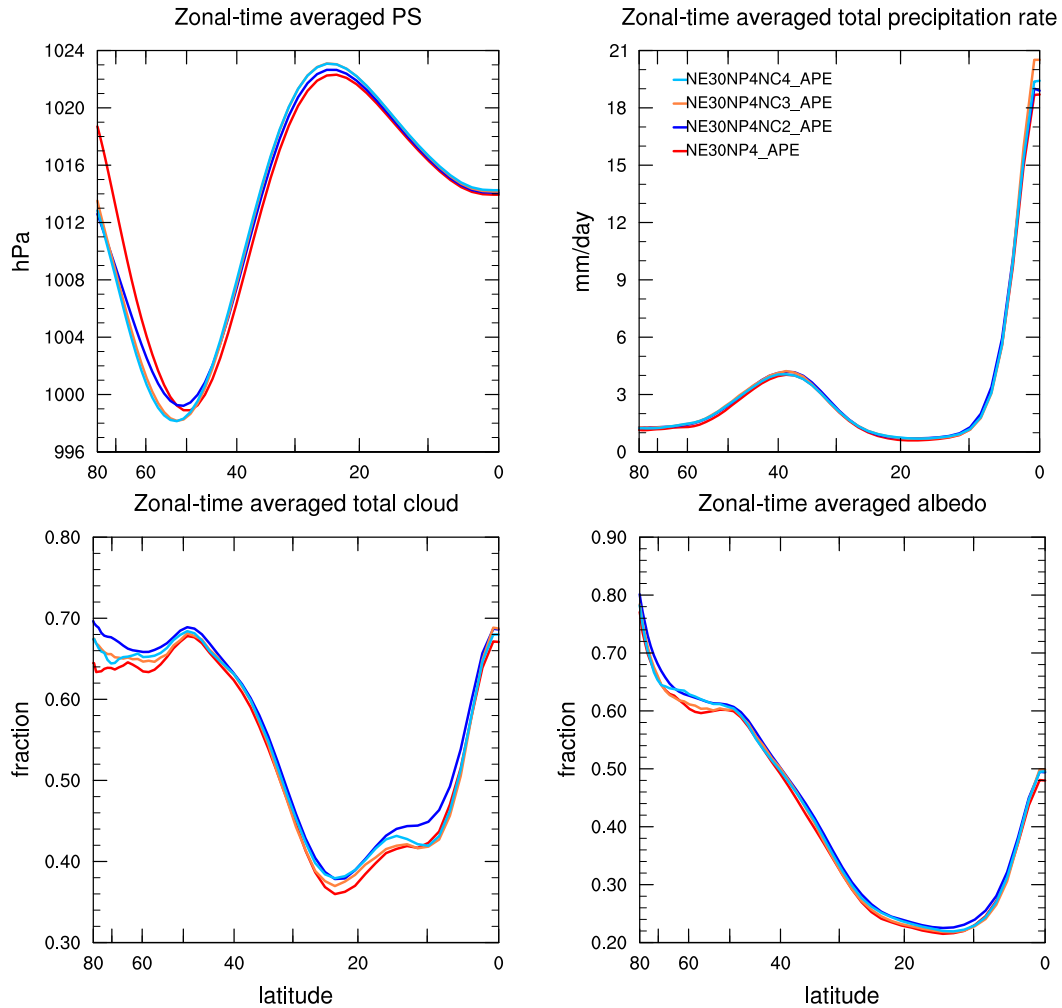


FIG. 11. Zonal-time average (top left) surface pressure, (top right) total precipitation rate, (bottom left) total cloud fraction, and (bottom right) albedo as a function of latitude (from the equator to 80°N) for the different configurations of CAM-SE. Temporal averaging over a period of 24 months and mapping to a  $1.5^\circ \times 1.5^\circ$  regular latitude-longitude grid was applied for analysis.

$n_e = 30$ , and  $4 \times 4$  quadrature point,  $n_p = 4$ , in each element). The physics tendencies are computed on the GLL grid (the grid of the dynamical core), a coarser ( $1.5^\circ$ ) physgrid, a same-resolution ( $1^\circ$ ) physgrid, and a finer-resolution ( $0.75^\circ$ ) physgrid. The four configurations are referred to as ne30np4, ne30np4nc2, ne30np4nc3, and ne30np4nc4, respectively, where nc2 refers to a  $2 \times 2$ , nc3 to a  $3 \times 3$ , and nc4 to a  $4 \times 4$  quasi-equal-area physics grid in each element. Note that the GLL grid is the grid on which the dynamical core operates. Aquaplanet simulations (Neale and Hoskins 2000) are performed with CAM4 physics (Neale et al. 2010a), and the physics time step is the default 1800 s. The reasoning behind choosing CAM4 physics instead of the newer CAM5 physics is that CAM4 physics is more resolution dependent (e.g., Bacmeister et al. 2014; Zarzycki et al. 2014b). CAM4

physics is therefore expected to produce more physgrid resolution dependence than CAM5. Simulation length is 30 months, and only the last 24 months are used for analysis. The code base used is revision 65448 of <https://svn-ccsm-models.cgd.ucar.edu/cam1/branches/physgrid>. Standard out-of-the-box namelist settings for the spectral element dynamical core were used.

Figure 11 shows the zonal-time average of surface pressure, total precipitation rate, total cloud fraction, and albedo as a function of latitude (from the equator to 80°N) for the different model configurations. The surface pressure field follows a slight decrease with increased physics grid resolution north of approximately 55°N. In the simulations presented in Williamson's (2008) Fig. 4, the surface pressure exhibited the same behavior when the model resolution was increased.

Precipitation rates show relatively little dependence on physics grid resolution, except at the equator. For total cloud fraction, [Williamson \(2008\)](#) observed that the fraction decreased with increasing resolution. This decrease is noted for the physgrid  $nc = 2$  and  $nc = 3$  simulations. For  $nc = 4$ , the cloud fractions are mostly bounded between the  $nc = 2$  and  $nc = 3$  cloud fraction values. The same is observed for albedo. So for the zonal-time-averaged fields, there seems to be little dependence on physics grid resolution.

In all, the physgrid configuration of CAM-SE has been demonstrated to produce aquaplanet results that are similar to the baseline (no physgrid) version. The dependence on physics grid resolution is different for different fields. The aquaplanet setup does not have a stationary gridscale forcing and is only suitable for analyzing the free modes in the atmosphere. The next step is to investigate the effect of a physics grid on applications with stationary gridscale forcing (e.g., orography). CAM-SE had been found to produce some noise if the orography is not sufficiently smoothed ([Lauritzen et al. 2015a](#)). The physgrid configuration has shown promise in alleviating spurious gridscale precipitation near steep orography due to the averaging over control volumes (especially near the edges of the elements). Similarly, the physgrid may improve simulations of other fields exposed to strong gridscale forcing, such as photolysis-driven tracers. An idealized test to investigate this has recently been developed ([Lauritzen et al. 2015b](#)). A newer version of the physics grid configuration of CAM-SE has been developed and is described by [Herrington et al. \(2018, manuscript submitted to \*Mon. Wea. Rev.\*\)](#).

#### *b. Emerging challenges in physics–dynamics coupling with multiscale models*

The grid lines of latitude–longitude grids converge at the poles by construction. This means that at the poles, the grid spacing is orders of magnitudes smaller than at the midlatitudes. This has two main disadvantages. First, the permissible time step is severely restricted, and for the sake of computational efficiency, this restriction is often violated at the poles. Second, waves excited at these small grid lengths are not supported elsewhere on the grid, leading to aliasing problems. This is commonly termed the pole problem. Atmospheric dynamical cores on quasi-uniform grids, which do not suffer from the pole problem, have been developed during the last decade ([Williamson 2007](#)).

Their development is also driven by the need to improve scalability on massively parallel computers and by diverse model applications from weather prediction to atmospheric chemistry and climate projections. For these applications, the dynamical cores ideally should

satisfy several properties, such as conservation, compatible or mimetic properties, and accurate representation of global-to-mesoscale flows ([Taylor and Fournier 2010](#); [Ringler et al. 2010](#); [Skamarock 2011](#); [Staniforth and Thuburn 2012](#)). These numerical techniques, along with progress in grid generation ([Tomita et al. 2002](#); [Anderson et al. 2009](#); [Ju et al. 2011](#); [Walko and Avissar 2011](#)), make it possible to increase grid resolution locally while maintaining a quasi-uniform resolution outside the refined domain. The associated grids are often described as unstructured because each cell is identified by a unique index and its connectivity to the neighboring cells, due to nonrectangular cell shapes and/or local coordinate system used in the numerical scheme. [Ju et al. \(2011\)](#) present examples of unstructured grids in quasi-uniform and variable-resolution configurations.

Local grid refinement is also possible by stretched-grid methods on structured grids that are continuously and conformally transformed to achieve higher gridcell density over a specified region ([Schmidt 1977](#); [Staniforth and Mitchell 1978](#)); general reviews can be found in [Fox-Rabinovitz et al. \(2006\)](#) and [McGregor \(2013\)](#). In this technique, the number of the grid points remains the same after the transformation, so the increase in resolution over one region must be compensated by the decrease in resolution in the rest of the model domain. Recently, the stretched-grid method has been extended to unstructured grids by [Uchida et al. \(2016\)](#). Here, all approaches that refine the horizontal resolutions over one or more regions on a global grid are referred to as the variable resolution (VR) approach.

With global VR models, higher horizontal resolutions can be achieved in the area(s) of interest, while the computational burden is reduced relative to global high-resolution simulations due to a coarser resolution over the remainder of the globe. The VR approach can avoid some of the known issues in limited-area models, such as the treatment of lateral boundaries, consistency between the global and regional models, and lack of two-way interactions between the regional simulations and their driving global simulations ([Wang et al. 2004](#)). Idealized testing demonstrates that properly designed numerical schemes on VR grids can provide additional finescale information at the regional scale without decreasing the accuracy of the global solution ([Ringler et al. 2011](#); [Ullrich and Jablonowski 2011](#); [Guba et al. 2014](#)).

The advantages and challenges of VR weather and climate modeling have been actively studied. The consensus is that VR models can provide the benefits of high-resolution simulation inside or even outside the refined domain. The benefits include improved orographic precipitation and snow cover ([Rhoades et al. 2016](#)), tropical

cyclones (Zarzycki and Jablonowski 2014, 2015; Zarzycki et al. 2014a), land-cover representation (Medvigy et al. 2011), remote influence from high-resolution regions (Medvigy et al. 2013; Sakaguchi et al. 2016), and overall regional climate metrics (Medvigy et al. 2010; Harris and Lin 2014; Harris et al. 2016; Sakaguchi et al. 2015; Zarzycki et al. 2015; Huang et al. 2016). Boundary effects have also been evaluated, finding few artifacts in propagating waves throughout the variable-resolution domain (Harris and Lin 2013; Hagos et al. 2013; Park et al. 2014; Zarzycki et al. 2015). So far the most challenging issue for VR models is related to unphysical sensitivity of physics parameterizations to spatial and temporal resolutions, although there are other potential challenges such as optimum orography smoothing on VR grids (e.g., Zarzycki et al. 2015).

Sections 2 and 7 illustrated several examples of undesirable sensitivities of weather and climate models to temporal and spatial resolutions. Specifically, section 2 discussed the mismatch between the predefined physical process time scales and the model time steps and how the mismatch affects the interaction among convection, cloud microphysics, and resolved dynamics in the sequential update time-splitting scheme. Similar sensitivities could negatively affect VR simulations that feature multiple resolutions within a single simulation. For example, a striking difference in precipitation appears inside and outside the high-resolution domains in aquaplanet VR simulations using the CAM-SE dynamical core (Zarzycki et al. 2014b) or the MPAS-A dynamical core (Hagos et al. 2013; Rauscher et al. 2013; Zhao et al. 2016). In the following, the effects of physics-dynamics coupling on the model sensitivity to spatial resolution in VR modeling are briefly explored.

Aquaplanet experiments were conducted using Model for Prediction across Scales-Atmosphere (MPAS-A) with the CAM4 physics as in Williamson (2013), who used the Eulerian spectral model with the same CAM4 physics. The version of MPAS-A used is the hydrostatic model described by Park et al. (2013) and Rauscher et al. (2013). The model was configured with three different grids: quasi-uniform (QU) 240 km, QU 120 km, and a VR grid with 30-km grid spacing at the center of the refined domain over the equator transitioning to 240-km grid spacing on the rest of the globe. The same configuration of the parameterization suite was used in all simulations, except for the numerical diffusion coefficient, which was adjusted based on the gridcell size (Rauscher et al. 2013). The same dynamics time step of 100 s was used in all simulations and for each grid cell in the VR simulations. The physics time step was defined independently of the dynamics time step. For each resolution, simulations with three different ratios  $R$  of the physics time step  $\Delta t$  to the

convective relaxation time scale  $\tau$  were run:  $R = 1/6$  ( $\Delta t = 600$  and  $\tau = 3600$  s),  $R = 1/2$  ( $\Delta t = 1800$  and  $\tau = 3600$  s), and  $R = 1$  ( $\Delta t = 600$  and  $\tau = 600$  s).

Reduced sensitivity to grid spacing of the total (convective + large scale) precipitation (Fig. 12a) is observed as  $R$  approaches unity in the QU simulations (Fig. 12a). The sensitivity of convective fraction to grid spacing is also reduced (Fig. 12b). This dependence of the resolution sensitivity on  $R$  has a visible impact on the VR simulations. For  $R = 1/6$ , the zonal anomaly (relative to the zonal mean) of precipitation appears on the western or downwind side of the refinement (Fig. 12c), and the attendant latent heating excites a Gill-type circulation apparent in the 200-hPa velocity potential as shown in Fig. 12e and Hagos et al. (2013), Rauscher et al. (2013), and Zarzycki et al. (2014b). Theoretically, the zonal anomaly should be nearly random spatially because there are no longitude-dependent forcings in the aquaplanet configuration. The model precipitation exhibits a substantially weaker sensitivity to the change of resolution with  $R = 1$  (Fig. 12d). When making  $\tau$  comparable to  $\Delta t$ , convection is more active in removing the instability created by the resolved dynamics (Williamson 2013). However, the zonal anomaly is still visible, and the undesirable Gill-type circulation is not eliminated (Fig. 12f).

A more physical behavior may be expected if  $\tau$  is allowed to vary with the grid spacing as opposed to using a constant value across the globe. Ma et al. (2014) and Gustafson et al. (2014) suggested a simple formulation of  $\tau$  as a linear function of grid spacing. This function is plotted in Fig. 13a. Fowler et al. (2016) tested another simple method to achieve scale-aware representation of convection in VR MPAS-A simulations. They used the Grell and Freitas (2014) convection scheme, which follows the approach originally suggested by Arakawa et al. (2011) and Arakawa and Wu (2013). In Fowler et al. (2016), the cloud-base mass flux  $M_b$  is scaled by a quadratic function of the convective cloud cover. With this grid-size-dependent scaling, convective precipitation is mostly parameterized with  $\geq 40$ -km grid spacing, but the fraction of parameterized convection rapidly decreases over the 5–30-km range, and most convection is allowed with  $< 5$ -km grid spacing (Fig. 13b). A heuristic, idealized analysis can be made to compare the resolution sensitivity in the context of VR modeling and the time scale mismatch (Williamson 2013).

With the modification following Grell and Freitas–Fowler (red line in Fig. 13c),  $M_b$  gradually decreases with reduced grid spacing, reaching a minimum value that is specific to the implementation of Fowler et al. (2016). This curve mimics the behavior of convection reported in their study. The Ma et al. (2014) approach

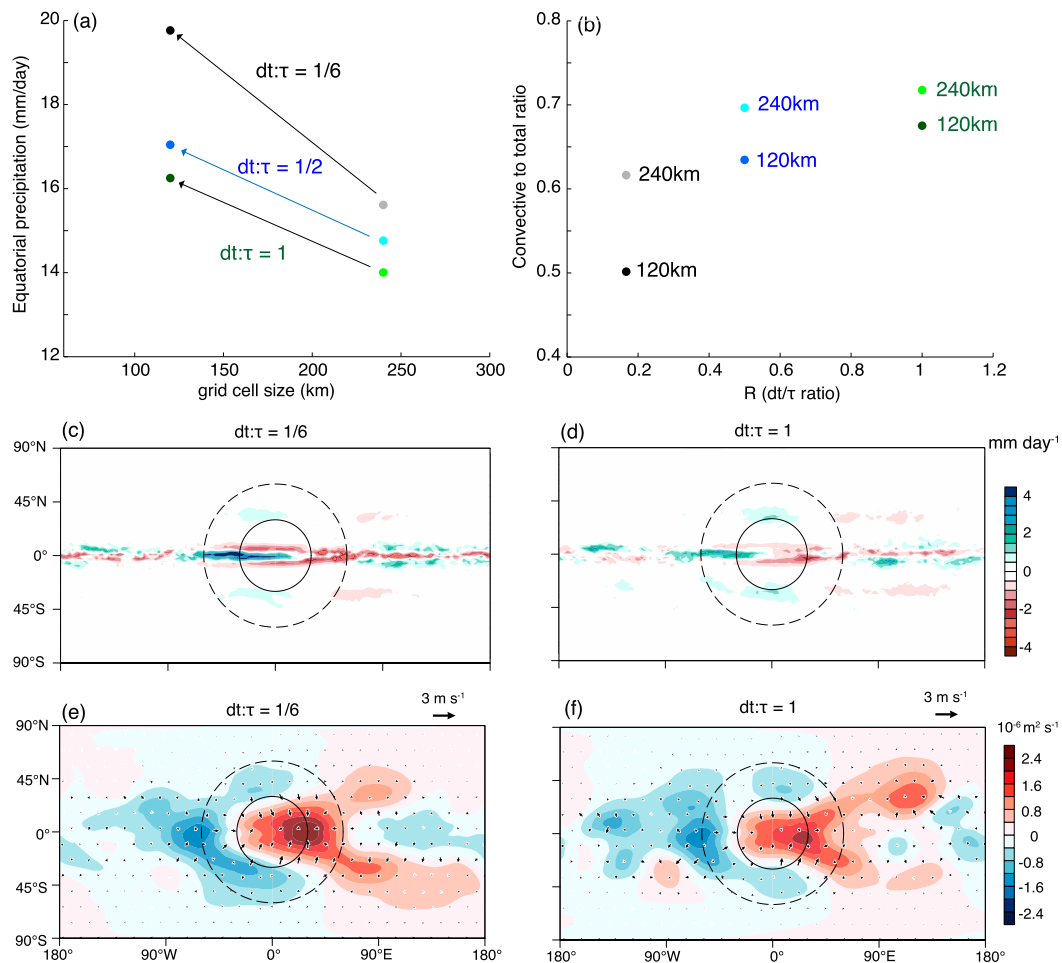


FIG. 12. Influence of  $R = \Delta t / \tau$  on the resolution sensitivity of the CAM4 physics (precipitation) to QU and VRs using MPAS-A. (a) Sensitivity of equatorial ( $\pm 2^\circ$  latitude) precipitation to gridcell size ( $x$  axis) in different values of  $R$  as represented by three arrows. (b) Fraction of convective precipitation as a function of  $R$  ( $x$  axis) and gridcell size (240 vs 120 km). (c) Zonal anomaly of precipitation in a VR simulation with  $R = 1/6$ . (d) As in (c), but a VR simulation with  $R = 1$ . (e) Zonal anomaly of velocity potential (shading) and divergent component of wind (arrows) with  $R = 1/6$ . (f) As in (e), but for  $R = 1$ . The solid and dashed circles in (c)–(f) represent the boundaries enclosing the domain with 30-km grid and the transition to 240-km grid domain, respectively.

exhibits a different behavior (blue line), with  $M_b$  increasing with decreasing grid spacing and reaching a maximum value at a grid size that depends on the tunable parameter. A simple combination of the two is also shown (green line).

A different picture emerges when  $M_b$  is multiplied by  $\Delta t$  to obtain the mass increment over one time step, which is an important quantity as it represents the effectiveness of deep convection to remove instability generated over one time step. Figure 13d shows the mass increment, assuming that  $\Delta t$  changes with  $\Delta x$  [e.g., by considering the Courant–Friedrichs–Lewy (CFL) stability criteria]. For simplicity,  $\Delta t$  is set to  $6 \times \Delta x$ , with  $\Delta x$  in km. The Ma et al. (2014) approach maintains a constant mass increment independent of grid spacing for grid cells larger than the

gray zone. By doing so, this approach allows deep convection to be active even as  $\Delta x$  (and  $\Delta t$ ) becomes smaller, thereby reducing the time step sensitivity elucidated by Williamson (2013). The  $R = 1$  case in Figs. 12a and 12b is another demonstration of the same principle of allowing deep convection to be active by making  $\tau$  and  $\Delta t$  comparable. On the other hand, the Grell and Freitas–Fowler approach produces a mass increment equal to or less than the default case. Therefore, the Grell and Freitas–Fowler approach will likely generate the same positive feedback and truncation-scale storms at high resolution as described by Williamson (2013) if it is implemented in CAM with the Zhang–McFarlane scheme. This problem may be avoided by combining the Grell and Freitas–Fowler formulation of mass flux with the linear equation for  $\tau$

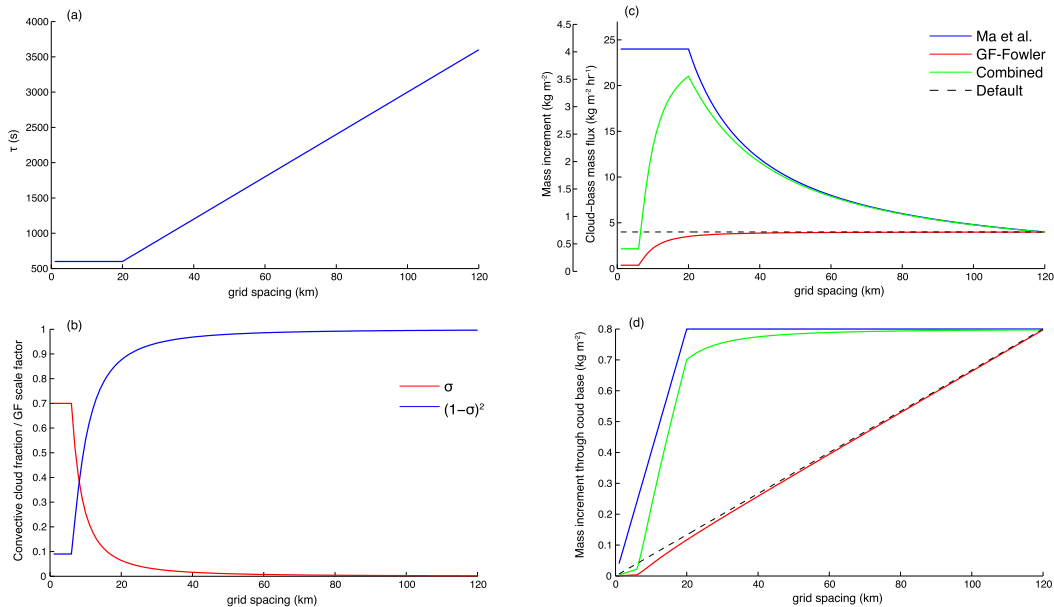


FIG. 13. Illustration of the Ma et al. (2014) and Fowler et al. (2016) approaches for scale-aware convection using the Zhang–McFarlane closure. (a) Term  $\tau$  from Ma et al. (2014) as a function of grid spacing. (b) The fractional convective cloud cover ( $\sigma$ ; red line) and scaling factor for cloud-base mass flux used in Fowler et al. (2016). (c) The cloud-base mass flux (inside y axis) based on the Zhang–McFarlane closure with  $\text{CAPE} = 1000 \text{ J kg}^{-1}$  and  $F = 250 \text{ J m}^2 \text{ kg}^{-2}$  and different modifications. Dashed line is the default with  $\tau = 3600 \text{ s}$  (Default); blue line is  $\tau$  following Ma et al. (2014); red line is  $\tau = 3600 \text{ s}$  (Grell and Freitas–Fowler); and green line is combined. The outside y axis in (c) shows the mass increment through the cloud base for  $\Delta t = 600 \text{ s}$  (i.e., multiply each curve by 600). (d) Mass increment through the cloud base is shown for the same cases in (c), using  $\Delta t = 6 \times \Delta x$ .

(Ma et al. 2014; Gustafson et al. 2014) (green line). Note that the closure assumption in the Grell and Freitas scheme is different from that in the Zhang–McFarlane scheme. It does not include a predefined convection time scale of Eq. (19) in Grell and Freitas, and both Gustafson et al. (2014) and Fowler et al. (2016) use the parallel split approach, in which tendencies from the convection scheme do not directly affect the behavior of the cloud microphysics within a time step. Therefore, the resolution sensitivity described here is for illustrative purpose and is not directly applicable to their simulations.

In VR models, it is common to use a constant dynamics time step that satisfies the stability criteria of the smallest grid cell for all the grid points in the global domain. Generally, the physics time step ( $\Delta t$ ) is also fixed to the dynamics time step. In this case, the mass increment over  $\Delta t$  behaves in the same way as  $M_b$  (as shown in Fig. 13c) because  $M_b$  is multiplied by the same constant  $\Delta t$ , regardless of the grid spacing. Based on this plot, the behavior of the Grell and Freitas–Fowler approach seems to be more desirable for VR models with a constant  $\Delta t$ , the CAM’s sequential update splitting, and Zhang–McFarlane convection. The modification by Ma et al. (2014) (and the result in Figs. 12d and 12f with  $R = 1$ ) would introduce a larger mass increment from the parameterized convection

for smaller grid spacing even beyond the gray zone, which is asymptotically erroneous. This artifact arises from the implicit assumption that  $\Delta t$  and  $\Delta x$  vary together, but this assumption breaks down in VR models. This simple analysis illustrates the dependence of scale-aware convection representation on the physics–dynamics coupling, such as the time-splitting method or the covariation between  $\Delta t$  and  $\Delta x$ , which has not been elucidated in the VR modeling framework.

Global simulations using the newer CAM5 parameterization suite show improvement in some of these aspects, particularly with respect to cloud fraction and precipitation scaling in VR simulations (Zarzycki et al. 2014b, 2015; Zhao et al. 2016). O’Brien et al. (2013) postulated that the large improvement in cloud fraction scaling is dominated by CAM5’s new microphysical parameterization (Morrison and Gettelman 2008). These results underscore the need to understand the complex relationships between the multitudes of components within parameterization suites that continue to grow in complexity.

## 9. Conclusions and outlook

Model resolutions, model complexity, and the accuracy of individual model components are all likely to

continue to increase. As they do, the errors due to what has here been referred to as physics–dynamics coupling will become increasingly important. This paper has presented some examples of the impacts of physics–dynamics coupling, such as those on climate sensitivity, clouds, and precipitation. For example, the RMS error of 10-m wind speeds has been reported to double under particular configurations of the dynamics–physics coupling. Also, issues with the convergence of the coupling between an atmosphere and an ocean model have been shown to dominate the overall coupled model error.

There is a large variety of approaches to understanding and addressing the challenges of physics–dynamics coupling. These range from full model runs using a range of time step sizes to gain insight (section 2); to the use of simplified equation sets such that an exact solution can be obtained and the coupling schemes analyzed against this reference solution (section 3); to the use of a hierarchy of models from simplified physics, through simplified forcing (aquaplanet model) to complete models (section 4).

Section 2 reviewed the splitting problem. Experience shows that a realistic atmospheric state is needed for the derivation of the highly nonlinear quantities used in parameterizations. This experience would argue for parallel splitting. However, it is also known that each parameterization needs to know about the increments being produced by the others. Sequential splitting allows this in a one-way sense. This “need to know” calls for fully implicit procedures following Cullen and Salmond (2003).

A common challenge is determining the “ground truth.” As has been discussed above on several occasions, it is not always clear how this can be defined. The issues of using a short time step solution for full model runs have been discussed in section 2. In section 3, the problem was approached from a different angle: the underlying equation set was simplified such that an exact solution could be obtained, and the coupling schemes were evaluated against this reference. In section 4, a hierarchy of model complexity, and hence a hierarchy of proxy ground truths, was used to unravel the complexity of physics–dynamics coupling. It is essential to design the model hierarchy to ensure that the experiment (and its proxy ground truth) has a realistic, albeit approximated, sensitivity. Then, provided the results are interpreted with full appreciation of the limitations of the imperfect proxy ground truths, physically relevant conclusions can be drawn.

The issues exposed by these various methods have quite distinct causes. Section 8 discusses the problems that arise due to the coupling of different numerical representations of the physical processes. One example

is the coupling of a finite difference scheme to a finite element scheme. Another is the coupling of a physical parameterization on one grid to a dynamical core on another grid. Equally though, issues also can arise at the continuous level. Because of different formulations and sometimes pragmatic attitudes toward the representation of the physics and the coupling between model components, consistency with the laws of thermodynamics might not be as strict as would be desirable. An example is given in section 6, which discusses the consequences of violating the second law of thermodynamics. Another issue that has emerged as model resolutions have increased is the problem of how to accurately represent aspects of a model that are partially resolved by the discrete system yet remain partially represented by a parameterization scheme. This problem is known as the gray zone problem, discussed in section 7, and requires the development of scale-aware parameterizations. As elaborated upon in section 8, this problem is perhaps most evident when variable-resolution grids are used, since for given computer power, these models can use smaller grids than would otherwise be the case. The coexistence of different resolutions in the same model means that the parameterization does not only need to be scale aware, but it also needs to be able to switch across and between resolutions seamlessly.

Physics–dynamics coupling is an important, complex, and pervasive modeling problem. Decisions in the development of new models and improvements to current ones demand guidance based on objective and systematic investigation and understanding of the physics–dynamics coupling issue. Generating this guidance is a challenging activity and one that impacts all of the modeling community, from developers to users. Because of its complexity, it has to be tackled by the community as a whole. The authors hope that this article helps to seed this development and provides a basis for this decision-making process. The PDC workshop series (2014 in Ensenada, Baja California, Mexico; 2016 in Richland, Washington; and 2018 in Reading, United Kingdom—refer to <http://pdc.cicese.mx> for the latest information and material from the previous workshops) will provide a platform for this.

*Acknowledgments.* The authors thank the small army of anonymous referees and editors, in particular Prof. David M. Schultz, who have tirelessly suggested numerous changes and corrections to the manuscript that have significantly improved the manuscript from its previous incarnations (Gross et al. 2016b, 2017). In particular, the authors thank Hillary Weller and John

Thuburn for their insightful suggestions, corrections, and moral support, without which this publication would not have been published in this way. No data intrinsic to this publication were used. Further information on the illustrative results presented here can be found in the references cited correspondingly. The National Center for Atmospheric Research is sponsored by the National Science Foundation. Peter Hjort Lauritzen (NCAR) would like to acknowledge the many discussions on high-order methods with Ram D. Nair (NCAR) and thank Paul A. Ullrich (UC Davis) for help on implementing his remapping method. The physgrid work would not have been possible without the support of Steve Goldhaber (NCAR) and Mark A. Taylor (SNL), who were partially funded by the Department of Energy Office of Biological and Environmental Research, work package 12-015334 (Multiscale Methods for Accurate, Efficient, and Scale-Aware Models of the Earth System). Peter Caldwell's work was performed under the auspices of the U.S. Department of Energy by Lawrence Livermore National Laboratory under Contract DE-AC52-07NA27344. Hui Wan was partially supported by the Linus Pauling Distinguished Postdoctoral Fellowship of the Pacific Northwest National Laboratory (PNNL) through the Laboratory Directed Research and Development Program. Hui Wan, Peter Caldwell, and Phil Rasch acknowledge support from the DOE Office of Science as part of the Scientific Discovery through Advanced Computing (SciDAC) Program. Christiane Jablonowski and Diana Thatcher (University of Michigan) were supported by the DOE Office of Science Grants DE-SC0006684 and DE-SC0003990. Koichi Sakaguchi and L. Ruby Leung were supported by the U.S. Department of Energy Office of Science Biological and Environmental Research as part of the Regional and Global Climate Modeling program, and they used the computational resources from the National Energy Research Scientific Computing Center (NERSC), a DOE User Facility supported by the Office of Science under Contract DE-AC02-05CH11231, and the PNNL Institutional Computing. Koichi Sakaguchi would like to thank Drs. Sara Rauscher (University of Delaware), Chun Zhao (PNNL), and Jin-Ho Yoon (PNNL) for their help on the MPAS simulations and Samson Hagos (PNNL) for helpful discussions. PNNL is operated for DOE by Battelle Memorial Institute under Contract DE-AC05-76RL01830. F. Lemarié and E. Blayo appreciate support from the French national research agency through Contract ANR-14-CE23-0010 (HEAT). The authors acknowledge the contribution to the field made by Jean-François Geleyn during his lifetime. The references to his work just in this paper are a clear testament to his broad and in-depth contributions. Unfortunately, health concerns prohibited him from delivering his keynote lecture at PDC14. Memoratus in aeternum. \*1950 †8 January 2015.

## APPENDIX A

### The Semigeostrophic Model

The ageostrophic wind equation (Cullen and Salmond 2003) with the “potential vorticity” matrix  $\mathbf{Q}$  is defined by

$$\mathbf{Q}\mathbf{u}_{\text{ag}} + \frac{\partial}{\partial t}\nabla p = \mathbf{H}, \quad (\text{A1})$$

with

$$\mathbf{Q} = \begin{pmatrix} fv_{gx} + f^2 & fv_{gy} & fv_{gz} \\ -fu_{gx} & f^2 - fu_{gy} & -fu_{gz} \\ g\theta_x/\theta_0 & g\theta_y/\theta_0 & g\theta_z/\theta_0 \end{pmatrix}, \quad \text{and} \quad (\text{A2})$$

$$\mathbf{H} = \begin{pmatrix} -f\mathbf{u}_g \cdot \nabla \mathbf{v}_g + F_1 \\ f\mathbf{u}_g \cdot \nabla \mathbf{u}_g + F_2 \\ -g\mathbf{u}_g \cdot \nabla \theta/\theta_0 + S \end{pmatrix}, \quad (\text{A3})$$

where  $\mathbf{u} = (u, v, w)$  is the velocity, with suffix  $g$  indicating geostrophic values;  $f$  is the Coriolis parameter;  $g$  is the acceleration due to gravity;  $\theta$  is the potential temperature with reference value  $\theta_0$ ; and  $F_1$ ,  $F_2$ , and  $S$  are momentum and thermodynamic forcing terms, respectively.

## APPENDIX B

### Compatibility of Parameterizations with the Laws of Thermodynamics

In the following equations, the overbar denotes Reynolds averaging, and the hat denotes mass-weighted averaging. For a generic variable  $\Phi$ , this is  $\Phi = \overline{\Phi} + \Phi'$  and  $\hat{\Phi} = \overline{\Phi} + \Phi'' = \overline{\rho\Phi}/\overline{\rho} + \Phi''$ , respectively. Parameter  $\rho$  denotes density;  $T$  is temperature;  $\mathbf{v}$  is the velocity vector with its components  $u$ ,  $v$ , and  $w$ ;  $p$  is pressure;  $\Pi$  is Exner pressure;  $\cdot\cdot$  is the double dot product, sometimes also written  $\cdot\cdot$ ;  $c_p$  and  $c_v$  are the specific heat at constant pressure and volume, respectively;  $\theta$  is potential temperature;  $g$  is gravitational acceleration;  $K^m$ ,  $K^\theta$ , and  $K^T$  are the diffusion coefficients for momentum, potential temperature, and temperature;  $\gamma$  is the countergradient term;  $N$  is Brunt–Väisälä frequency;  $\partial_z$  and  $\partial_t$  are the partial derivative with respect to the vertical coordinate axis and time, respectively; and  $s$  is entropy.

#### a. Dry atmosphere

For a dry atmosphere without radiation effects, the subenergy equations for internal energy  $c_v\hat{T}$ , TKE  $k_e$ , resolved kinetic energy  $\hat{\mathbf{v}}^2/2$ , and potential energy  $\Phi$  are

$$\begin{aligned} \partial_t(c_v \bar{\rho} \hat{T}) &= -\nabla \cdot (c_v \bar{\rho} \hat{\mathbf{v}} \hat{T}) - \nabla \cdot (\overline{c_v \rho \mathbf{v}'' T''}) - \bar{p} \nabla \cdot \mathbf{v} + \varepsilon_{\text{tke}} - c_p \overline{\rho \mathbf{v}'' \theta''} \cdot \nabla \bar{\Pi} \\ &= -\nabla \cdot [c_p \bar{\Pi} (\bar{\rho} \hat{\mathbf{v}} \hat{\theta} + \overline{\rho \mathbf{v}'' \theta''})] + c_p \bar{\rho} \hat{\mathbf{v}} \hat{\theta} \cdot \nabla \bar{\Pi} \\ &\quad + c_p \overline{\rho \mathbf{v}'' \theta''} \cdot \nabla \bar{\Pi} + \varepsilon_{\text{tke}}, \end{aligned} \quad (\text{B1})$$

$$\begin{aligned} \partial_t(\bar{\rho} k_e) &= -\nabla \cdot (\bar{\rho} \hat{\mathbf{v}} k_e + \overline{\rho \mathbf{v}'' k_e''}) - c_p \overline{\rho \mathbf{v}'' \theta''} \cdot \nabla \bar{\Pi} \\ &\quad - \overline{\rho \mathbf{v}'' \mathbf{v}''} : \nabla \hat{\mathbf{v}} - \varepsilon_{\text{tke}}, \end{aligned} \quad (\text{B2})$$

$$\begin{aligned} \partial_t(\bar{\rho} \hat{\mathbf{v}}^2/2) &= -\nabla \cdot [\bar{\rho} \hat{\mathbf{v}} (\hat{\mathbf{v}}^2/2) + \overline{\rho \mathbf{v}'' \mathbf{v}''} : \hat{\mathbf{v}}] - \bar{\rho} \hat{\mathbf{v}} \cdot \nabla \Phi \\ &\quad - c_p \bar{\rho} \hat{\mathbf{v}} \hat{\theta} \cdot \nabla \bar{\Pi} + \overline{\rho \mathbf{v}'' \mathbf{v}''} : \nabla \hat{\mathbf{v}}, \end{aligned} \quad (\text{B3})$$

$$\partial_t(\bar{\rho} \Phi) = -\nabla \cdot (\bar{\rho} \hat{\mathbf{v}} \Phi) + \bar{\rho} \hat{\mathbf{v}} \cdot \nabla \Phi. \quad (\text{B4})$$

The internal energy equation must be formulated with the turbulence averaging also applied to the work term. Combining the work term and the internal energy transport term yields the second form with Exner pressure  $\bar{\Pi}$  and potential temperature  $\theta$ , which is more convenient for the following discussion.

#### b. Stable and unstable stratification

For unstable stratification,

$$c_p \overline{\rho \mathbf{v}'' \theta''} \cdot \nabla \bar{\Pi} \approx c_p \overline{\rho w'' \theta''} \partial_z \bar{\Pi} \approx g \bar{\rho} K^\theta \partial_z \hat{\theta} / \hat{\theta} = \bar{\rho} K^\theta N^2 < 0, \quad (\text{B5})$$

and the internal energy equation reads

$$\begin{aligned} \partial_t(c_v \bar{\rho} \hat{T}) &= -\nabla \cdot (c_p \bar{\Pi} \bar{\rho} \hat{\mathbf{v}} \hat{\theta}) + c_p \bar{\rho} \hat{\mathbf{v}} \hat{\theta} \cdot \nabla \bar{\Pi} - \overline{\rho \mathbf{v}'' \mathbf{v}''} : \nabla \hat{\mathbf{v}} \\ &\quad - \nabla \cdot (c_p \bar{\Pi} \overline{\rho \mathbf{v}'' \theta''}). \end{aligned} \quad (\text{B6})$$

For stable stratification,

$$c_p \overline{\rho \mathbf{v}'' \theta''} \cdot \nabla \bar{\Pi} \approx c_p \overline{\rho w'' \theta''} \partial_z \bar{\Pi} \approx g \bar{\rho} K^\theta \partial_z \hat{\theta} / \hat{\theta} = \bar{\rho} K^\theta N^2 > 0, \quad (\text{B7})$$

and the internal energy equation reads

$$\begin{aligned} \partial_t(c_v \bar{\rho} \hat{T}) &= -\nabla \cdot (c_p \bar{\Pi} \bar{\rho} \hat{\mathbf{v}} \hat{\theta}) + c_p \bar{\rho} \hat{\mathbf{v}} \hat{\theta} \cdot \nabla \bar{\Pi} - \overline{\rho \mathbf{v}'' \mathbf{v}''} : \nabla \hat{\mathbf{v}} \\ &\quad - c_p \bar{\Pi} \nabla \cdot (\overline{\rho \mathbf{v}'' \theta''}). \end{aligned} \quad (\text{B8})$$

The resolved kinetic energy equation in the case of stable stratification is

$$\begin{aligned} \partial_t(\bar{\rho} \hat{\mathbf{v}}^2/2) &= -\nabla \cdot [\bar{\rho} \hat{\mathbf{v}} (\hat{\mathbf{v}}^2/2) + \overline{\rho \mathbf{v}'' \mathbf{v}''} : \hat{\mathbf{v}}] - \bar{\rho} \hat{\mathbf{v}} \cdot \nabla \Phi \\ &\quad - c_p \bar{\rho} \hat{\mathbf{v}} \hat{\theta} \cdot \nabla \bar{\Pi} + \overline{\rho \mathbf{v}'' \mathbf{v}''} : \nabla \hat{\mathbf{v}} - c_p \overline{\rho \mathbf{v}'' \theta''} \cdot \nabla \bar{\Pi}, \end{aligned} \quad (\text{B9})$$

where the last term

describes the work that must be performed to push isentropes down at stable stratification.

The associated entropy budget equations are

$$\begin{aligned} \partial_t(\bar{\rho} \hat{s}) &= -\nabla \cdot (\bar{\rho} \hat{\mathbf{v}} \hat{s}) - \nabla \cdot \left( \frac{c_p \overline{\rho \mathbf{v}'' \theta''}}{\hat{\theta}} \right) - \frac{c_p \bar{\Pi} \overline{\rho \mathbf{v}'' \theta''}}{\hat{T}^2} \cdot \nabla \hat{T} \\ &\quad - \frac{\overline{\rho \mathbf{v}'' \mathbf{v}''} : \nabla \hat{\mathbf{v}}}{\hat{T}}, \end{aligned} \quad (\text{B11})$$

and

$$\begin{aligned} \partial_t(\bar{\rho} \hat{s}) &= -\nabla \cdot (\bar{\rho} \hat{\mathbf{v}} \hat{s}) - \nabla \cdot \left( \frac{c_p \overline{\rho \mathbf{v}'' \theta''}}{\hat{\theta}} \right) - \frac{c_p \overline{\rho \mathbf{v}'' \theta''}}{\hat{\theta}^2} \cdot \nabla \hat{\theta} \\ &\quad - \frac{\overline{\rho \mathbf{v}'' \mathbf{v}''} : \nabla \hat{\mathbf{v}}}{\hat{T}}, \end{aligned} \quad (\text{B12})$$

for unstable stratification and stable stratification, respectively. The two last terms are the internal entropy production terms.

#### REFERENCES

- Anderson, B. D., S. E. Benzley, and S. J. Owen, 2009: Automatic all quadrilateral mesh adaption through refinement and coarsening. *Proc. 18th Int. Meshing Roundtable*, Sandia National Laboratories, Salt Lake City, UT, 557–574, [https://doi.org/10.1007/978-3-642-04319-2\\_32](https://doi.org/10.1007/978-3-642-04319-2_32).
- Arakawa, A., and W. H. Schubert, 1974: Interaction of a cumulus cloud ensemble with the large-scale environment. Part I. *J. Atmos. Sci.*, **31**, 674–701, [https://doi.org/10.1175/1520-0469\(1974\)031<0674:IOACCE>2.0.CO;2](https://doi.org/10.1175/1520-0469(1974)031<0674:IOACCE>2.0.CO;2).
- , and C. Wu, 2013: A unified representation of deep moist convection in numerical modeling of the atmosphere. Part I. *J. Atmos. Sci.*, **70**, 1977–1992, <https://doi.org/10.1175/JAS-D-12-0330.1>.
- , J.-H. Jung, and C.-M. Wu, 2011: Toward unification of the multiscale modeling of the atmosphere. *Atmos. Chem. Phys.*, **11**, 3731–3742, <https://doi.org/10.5194/acp-11-3731-2011>.
- Bacmeister, J. T., P. Lauritzen, A. Dai, and J. Truesdale, 2012: Assessing possible dynamical effects of condensate in high resolution climate models. *Geophys. Res. Lett.*, **39**, L04806, <https://doi.org/10.1029/2011GL050533>.
- , M. F. Wehner, R. B. Neale, A. Gettelman, C. Hannay, P. H. Lauritzen, J. M. Caron, and J. E. Truesdale, 2014: Exploratory high-resolution climate simulations using the Community Atmosphere Model (CAM). *J. Climate*, **27**, 3073–3099, <https://doi.org/10.1175/JCLI-D-13-00387.1>.
- Balaji, V., J. Anderson, I. Held, M. Winton, S. Malyshev, and R. Stouffer, 2007: The FMS exchange grid: A mechanism for data exchange between Earth system components on independent grids. *Proc. 2005 Int. Conf. on Parallel Computational Fluid Dynamics*, College Park, MD, NOAA/GFDL, 18 pp.
- Bannon, P. R., 2002: Theoretical foundations for models of moist convection. *J. Atmos. Sci.*, **59**, 1967–1982, [https://doi.org/10.1175/1520-0469\(2002\)059<1967:TFFMOM>2.0.CO;2](https://doi.org/10.1175/1520-0469(2002)059<1967:TFFMOM>2.0.CO;2).

- , 2015: Entropy production and climate efficiency. *J. Atmos. Sci.*, **72**, 3268–3280, <https://doi.org/10.1175/JAS-D-14-0361.1>.
- , and S. Lee, 2017: Toward quantifying the climate heat engine: Solar absorption and terrestrial emission temperatures and material entropy production. *J. Atmos. Sci.*, **74**, 1721–1734, <https://doi.org/10.1175/JAS-D-16-0240.1>.
- Barker, H. W., J. N. S. Cole, J.-J. Morcrette, R. Pincus, P. Räisänen, K. von Salzen, and P. A. Vaillancourt, 2008: The Monte Carlo independent column approximation: An assessment using several global atmospheric models. *Quart. J. Roy. Meteor. Soc.*, **134**, 1463–1478, <https://doi.org/10.1002/qj.303>.
- Beare, R. J., and M. J. P. Cullen, 2013: Diagnosis of boundary-layer circulations. *Philos. Trans. Roy. Soc. London*, **371A**, 20110474, <https://doi.org/10.1098/rsta.2011.0474>.
- , and —, 2016: Validating weather and climate models at small Rossby numbers: Including a boundary layer. *Quart. J. Roy. Meteor. Soc.*, **142**, 2636–2645, <https://doi.org/10.1002/qj.2852>.
- Bechtold, P., N. Semane, P. Lopez, J.-P. Chaboureau, A. Beljaars, and N. Bormann, 2014: Representing equilibrium and non-equilibrium convection in large-scale models. *J. Atmos. Sci.*, **71**, 734–753, <https://doi.org/10.1175/JAS-D-13-0163.1>.
- Beljaars, A., P. Bechtold, M. Köhler, J. J. Morcrette, A. Tompkins, P. Viterbo, and N. Wedi, 2004: The numerics of physical parameterization. *Proc. ECMWF Workshop on Recent Developments in Numerical Methods for Atmosphere and Ocean Modelling*, Shinfield Park, Reading, United Kingdom, ECMWF, 113–135.
- , E. Dutra, G. Balsamo, and F. Lemarié, 2017: On the numerical stability of surface–atmosphere coupling in weather and climate models. *Geosci. Model Dev.*, **10**, 977–989, <https://doi.org/10.5194/gmd-10-977-2017>.
- Best, M. J., A. Beljaars, J. Polcher, and P. Viterbo, 2004: A proposed structure for coupling tiled surfaces with the planetary boundary layer. *J. Hydrometeorol.*, **5**, 1271–1278, <https://doi.org/10.1175/JHM-382.1>.
- Blackburn, M., and B. J. Hoskins, 2013: Context and aims of the Aqua-Planet Experiment. *J. Meteor. Soc. Japan*, **91A**, 1–15, <https://doi.org/10.2151/jmsj.2013-A01>.
- , and Coauthors, 2013: The Aqua-Planet Experiment (APE): Control SST simulation. *J. Meteor. Soc. Japan*, **91A**, 17–56, <https://doi.org/10.2151/jmsj.2013-A02>.
- Bogenschütz, P. A., A. Gettelman, H. Morrison, V. E. Larson, D. P. Schanen, N. R. Meyer, and C. Craig, 2012: Unified parameterization of the planetary boundary layer and shallow convection with a higher-order turbulence closure in the Community Atmosphere Model: Single-column experiments. *Geosci. Model Dev.*, **5**, 1407–1423, <https://doi.org/10.5194/gmd-5-1407-2012>.
- , —, —, C. Craig, and D. P. Schanen, 2013: Higher-order turbulence closure and its impact on climate simulations in the Community Atmosphere Model. *J. Climate*, **26**, 9655–9676, <https://doi.org/10.1175/JCLI-D-13-00075.1>.
- Boutle, I. A., J. E. J. Eyre, and A. P. Lock, 2014: Seamless stratocumulus simulation across the turbulent gray zone. *Mon. Wea. Rev.*, **142**, 1655–1668, <https://doi.org/10.1175/MWR-D-13-00229.1>.
- Brdar, S., M. Baldauf, A. Dedner, and R. Klöforn, 2013: Comparison of dynamical cores for NWP models: Comparison of COSMO and Dune. *Theor. Comput. Fluid Dyn.*, **27**, 453–472, <https://doi.org/10.1007/s00162-012-0264-z>.
- Bretherton, C. S., and P. K. Smolarkiewicz, 1989: Gravity waves, compensating subsidence and detrainment around cumulus clouds. *J. Atmos. Sci.*, **46**, 740–759, [https://doi.org/10.1175/1520-0469\(1989\)046<0740:GWCSAD>2.0.CO;2](https://doi.org/10.1175/1520-0469(1989)046<0740:GWCSAD>2.0.CO;2).
- , and S. Park, 2009: A new moist turbulence parameterization in the Community Atmosphere Model. *J. Climate*, **22**, 3422–3448, <https://doi.org/10.1175/2008JCLI2556.1>.
- Burchard, H., E. Deleersnijder, and G. Stoyan, 2005: Some numerical aspects of turbulence-closure models. *Marine Turbulence: Theories, Observations and Models*, H. Baumert, J. Simpson, and J. Sündermann, Eds., Cambridge University Press, 197–206.
- Catry, B., J.-F. Geleyn, M. Tudor, P. Bénard, and A. Trojáková, 2007: Flux-conservative thermodynamic equations in a mass-weighted framework. *Tellus*, **59A**, 71–79, <https://doi.org/10.1111/j.1600-0870.2006.00212.x>.
- Connors, J., and B. Ganis, 2011: Stability of algorithms for a two domain natural convection problem and observed model uncertainty. *Comput. Geosci.*, **15**, 509–527, <https://doi.org/10.1007/s10596-010-9219-x>.
- Cullen, M. J. P., 2006: *A Mathematical Theory of Large-Scale Atmosphere/Ocean Flow*. Imperial College Press, 259 pp.
- , 2007: Modelling atmospheric flows. *Acta Numer.*, **16**, 67–154, <https://doi.org/10.1017/S0962492906290019>.
- , and D. J. Salmond, 2003: On the use of a predictor-corrector scheme to couple the dynamics with the physical parameterizations in the ECMWF model. *Quart. J. Roy. Meteor. Soc.*, **129**, 1217–1236, <https://doi.org/10.1256/qj.02.12>.
- de Groot, S. R., and P. Mazur, 1984: *Non-Equilibrium Thermodynamics*. Courier Corporation, 510 pp.
- Deleersnijder, E., E. Hanert, H. Burchard, and H. Dijkstra, 2008: On the mathematical stability of stratified flow models with local turbulence closure schemes. *Ocean Dyn.*, **58**, 237–246, <https://doi.org/10.1007/s10236-008-0145-6>.
- De Meutter, P., L. Gerard, G. Smet, K. Hamid, R. Hamdi, D. Degrauwe, and P. Termonia, 2015: Predicting small-scale, short-lived downbursts: Case study with the NWP limited-area ALARO model for the Pukkelpop thunderstorm. *Mon. Wea. Rev.*, **143**, 742–756, <https://doi.org/10.1175/MWR-D-14-00290.1>.
- Dennis, J., and Coauthors, 2012: CAM-SE: A scalable spectral element dynamical core for the Community Atmosphere Model. *Int. J. High Perform. Comput. Appl.*, **26**, 74–89, <https://doi.org/10.1177/1094342011428142>.
- De Troch, R., R. Hamdi, H. Van de Vyver, J.-F. Geleyn, and P. Termonia, 2013: Multiscale performance of the ALARO-0 model for simulating extreme summer precipitation climatology in Belgium. *J. Climate*, **26**, 8895–8915, <https://doi.org/10.1175/JCLI-D-12-00844.1>.
- Donahue, A. S., and P. M. Caldwell, 2018: Impact of physics parameterization ordering in a global atmosphere model. *J. Adv. Model. Earth Syst.*, **10**, 481–499, <https://doi.org/10.1002/2017MS001067>.
- Durrant, D., 2010: *Numerical Methods for Fluid Dynamics: With Applications to Geophysics*. 2nd ed. Texts in Applied Mathematics, Vol. 32, Springer, 516 pp.
- Foken, T., 2006: 50 years of the Monin–Obukhov similarity theory. *Bound.-Layer Meteorol.*, **119**, 431–447, <https://doi.org/10.1007/s10546-006-9048-6>.
- Fowler, L. D., W. C. Skamarock, G. A. Grell, S. R. Freitas, and M. G. Duda, 2016: Analyzing the Grell–Freitas convection scheme from hydrostatic to nonhydrostatic scales within a global model. *Mon. Wea. Rev.*, **144**, 2285–2306, <https://doi.org/10.1175/MWR-D-15-0311.1>.
- Fox-Rabinovitz, M. S., J. Côté, B. Dugas, M. Déqué, and J. L. McGregor, 2006: Variable resolution general circulation models: Stretched-grid model intercomparison project (SGMIP). *J. Geophys. Res.*, **111**, D16104, <https://doi.org/10.1029/2005JD006520>.

- Frierson, D. M. W., I. M. Held, and P. Zurita-Gotor, 2006: A gray-radiation aquaplanet moist GCM. Part I: Static stability and eddy scale. *J. Atmos. Sci.*, **63**, 2548–2566, <https://doi.org/10.1175/JAS3753.1>.
- Gassmann, A., 2013: A global hexagonal C-grid non-hydrostatic dynamical core (ICON-IAP) designed for energetic consistency. *Quart. J. Roy. Meteor. Soc.*, **139**, 152–175, <https://doi.org/10.1002/qj.1960>.
- , 2018: Entropy production due to subgrid-scale thermal fluxes with application to breaking gravity waves. *Quart. J. Roy. Meteor. Soc.*, **144**, 499–510, <https://doi.org/10.1002/qj.3221>.
- , and H.-J. Herzog, 2015: How is local material entropy production represented in a numerical model? *Quart. J. Roy. Meteor. Soc.*, **141**, 854–869, <https://doi.org/10.1002/qj.2404>.
- Geleyn, J.-F., and P. Marquet, 2011: Moist thermodynamics and moist turbulence for modelling at the non-hydrostatic scales. *Proc. ECMWF Workshop on Non-Hydrostatic Modelling*, Shinfield Park, Reading, United Kingdom, ECMWF, 55–66.
- Gerard, L., 2015: Bulk mass-flux perturbation formulation for a unified approach of deep convection at high resolution. *Mon. Wea. Rev.*, **143**, 4038–4063, <https://doi.org/10.1175/MWR-D-15-0030.1>.
- , and J.-F. Geleyn, 2005: Evolution of a subgrid deep convection parametrization in a limited-area model with increasing resolution. *Quart. J. Roy. Meteor. Soc.*, **131**, 2293–2312, <https://doi.org/10.1256/qj.04.72>.
- , J.-M. Piriou, R. Brožková, J.-F. Geleyn, and D. Banciu, 2009: Cloud and precipitation parametrization in a meso-gamma-scale operational weather prediction model. *Mon. Wea. Rev.*, **137**, 3960–3977, <https://doi.org/10.1175/2009MWR2750.1>.
- Gottelman, A., H. Morrison, S. Santos, P. Bogenschütz, and P. M. Caldwell, 2015: Advanced two-moment bulk microphysics for global models. Part II: Global model solutions and aerosol–cloud interactions. *J. Climate*, **28**, 1288–1307, <https://doi.org/10.1175/JCLI-D-14-00103.1>.
- Giraldo, F., and M. Restelli, 2008: A study of spectral element and discontinuous Galerkin methods for the Navier–Stokes equations in nonhydrostatic mesoscale atmospheric modeling: Equation sets and test cases. *J. Comput. Phys.*, **227**, 3849–3877, <https://doi.org/10.1016/j.jcp.2007.12.009>.
- Golaz, J.-C., V. E. Larson, and W. R. Cotton, 2002a: A PDF-based model for boundary layer clouds. Part I: Method and model description. *J. Atmos. Sci.*, **59**, 3540–3551, [https://doi.org/10.1175/1520-0469\(2002\)059<3540:APBMFB>2.0.CO;2](https://doi.org/10.1175/1520-0469(2002)059<3540:APBMFB>2.0.CO;2).
- , —, and —, 2002b: A PDF-based model for boundary layer clouds. Part II: Model results. *J. Atmos. Sci.*, **59**, 3552–3571, [https://doi.org/10.1175/1520-0469\(2002\)059<3552:APBMFB>2.0.CO;2](https://doi.org/10.1175/1520-0469(2002)059<3552:APBMFB>2.0.CO;2).
- Goody, R., 2000: Sources and sinks of climate entropy. *Quart. J. Roy. Meteor. Soc.*, **126**, 1953–1970, <https://doi.org/10.1002/qj.49712656619>.
- Grell, G. A., and S. R. Freitas, 2014: A scale and aerosol aware stochastic convective parameterization for weather and air quality modeling. *Atmos. Chem. Phys.*, **14**, 5233–5250, <https://doi.org/10.5194/acp-14-5233-2014>.
- Gross, M., S. Malardel, C. Jablonowski, and N. Wood, 2016a: Bridging the (knowledge) gap between physics and dynamics. *Bull. Amer. Meteor. Soc.*, **97**, 137–142, <https://doi.org/10.1175/BAMS-D-15-00103.1>.
- , and Coauthors, 2016b: Recent progress and review of physics dynamics coupling in geophysical models. [arXiv.org](https://arxiv.org/abs/1605.06480v1), 30 pp., <https://arxiv.org/abs/1605.06480v1>.
- , and Coauthors, 2017: Recent progress and review of issues related to physics dynamics coupling in geophysical models. [arXiv.org](https://arxiv.org/abs/1605.06480v2), 61 pp., <https://arxiv.org/abs/1605.06480v2>.
- Guba, O., M. A. Taylor, P. A. Ullrich, J. R. Overfelt, and M. N. Levy, 2014: The spectral element method (SEM) on variable-resolution grids: Evaluating grid sensitivity and resolution-aware numerical viscosity. *Geosci. Model Dev.*, **7**, 2803–2816, <https://doi.org/10.5194/gmd-7-2803-2014>.
- Gustafson, W. I., P.-L. Ma, H. Xiao, B. Singh, P. J. Rasch, and J. D. Fast, 2013: The Separate Physics and Dynamics Experiment (SPADE) framework for determining resolution awareness: A case study of microphysics. *J. Geophys. Res. Atmos.*, **118**, 9258–9276, <https://doi.org/10.1002/jgrd.50711>.
- , —, and B. Singh, 2014: Precipitation characteristics of CAM5 physics at mesoscale resolution during MC3E and the impact of convective timescale choice. *J. Adv. Model. Earth Syst.*, **6**, 1271–1287, <https://doi.org/10.1002/2014MS000334>.
- Hagos, S., R. Leung, S. A. Rauscher, and T. Ringler, 2013: Error characteristics of two grid refinement approaches in aquaplanet simulations: MPAS-A and WRF. *Mon. Wea. Rev.*, **141**, 3022–3036, <https://doi.org/10.1175/MWR-D-12-00338.1>.
- Harris, L. M., and S.-J. Lin, 2013: A two-way nested global-regional dynamical core on the cubed-sphere grid. *Mon. Wea. Rev.*, **141**, 283–306, <https://doi.org/10.1175/MWR-D-11-00201.1>.
- , and —, 2014: Global-to-regional nested grid climate simulations in the GFDL High Resolution Atmospheric Model. *J. Climate*, **27**, 4890–4910, <https://doi.org/10.1175/JCLI-D-13-00596.1>.
- , —, and C. Y. Tu, 2016: High-resolution climate simulations using GFDL HiRAM with a stretched global grid. *J. Climate*, **29**, 4293–4314, <https://doi.org/10.1175/JCLI-D-15-0389.1>.
- Held, I. M., and M. J. Suarez, 1994: A proposal for the intercomparison of dynamical cores of atmospheric general circulation models. *Bull. Amer. Meteor. Soc.*, **75**, 1825–1830, [https://doi.org/10.1175/1520-0477\(1994\)075<1825:APFTIO>2.0.CO;2](https://doi.org/10.1175/1520-0477(1994)075<1825:APFTIO>2.0.CO;2).
- Hodyss, D., K. C. Viner, A. Reinecke, and J. A. Hansen, 2013: The impact of noisy physics on the stability and accuracy of physics–dynamics coupling. *Mon. Wea. Rev.*, **141**, 4470–4486, <https://doi.org/10.1175/MWR-D-13-00035.1>.
- Holloway, C. E., S. J. Woolnough, and G. M. S. Lister, 2012: Precipitation distributions for explicit versus parametrized convection in a large-domain high-resolution tropical case study. *Quart. J. Roy. Meteor. Soc.*, **138**, 1692–1708, <https://doi.org/10.1002/qj.1903>.
- Holt, M. W., 1989: Semigeostrophic moist frontogenesis in a Lagrangian model. *Dyn. Atmos. Oceans*, **14**, 463–481, [https://doi.org/10.1016/0377-0265\(89\)90073-0](https://doi.org/10.1016/0377-0265(89)90073-0).
- Honnert, R., and V. Masson, 2014: What is the smallest physically acceptable scale for 1D turbulence schemes? *Front. Earth Sci.*, **2**, 27, <https://doi.org/10.3389/feart.2014.00027>.
- Hourdin, F., and Coauthors, 2017: The art and science of climate model tuning. *Bull. Amer. Meteor. Soc.*, **98**, 589–602, <https://doi.org/10.1175/BAMS-D-15-00135.1>.
- Huang, X., A. M. Rhoades, P. A. Ullrich, and C. M. Zarzycki, 2016: An evaluation of the variable-resolution CESM for modeling California’s climate. *J. Adv. Model. Earth Syst.*, **8**, 345–369, <https://doi.org/10.1002/2015MS000559>.
- Jablonowski, C., and D. L. Williamson, 2011: The pros and cons of diffusion, filters and fixers in atmospheric general circulation models. *Numerical Techniques for Global Atmospheric Models*, P. H. Lauritzen et al., Eds., Lecture Notes in Computational Science and Engineering, Vol. 80, Springer, 381–493, [https://doi.org/10.1007/978-3-642-11640-7\\_13](https://doi.org/10.1007/978-3-642-11640-7_13).
- Ju, L., T. Ringler, and M. Gunzburger, 2011: Voronoi tessellations and their application to climate and global modeling. *Numerical Techniques for Global Atmospheric Models*, P. H. Lauritzen et al., Eds., Lecture Notes in Computational

- Science and Engineering, Vol. 80, Springer, 313–342, [https://doi.org/10.1007/978-3-642-11640-7\\_10](https://doi.org/10.1007/978-3-642-11640-7_10).
- Keyes, D. E., and Coauthors, 2013: Multiphysics simulations: Challenges and opportunities. *Int. J. High Perform. Comput. Appl.*, **27**, 4–83, <https://doi.org/10.1177/1094342012468181>.
- Klocke, D., R. Pincus, and J. Quaas, 2011: On constraining estimates of climate sensitivity with present-day observations through model weighting. *J. Climate*, **24**, 6092–6099, <https://doi.org/10.1175/2011JCLI4193.1>.
- Kuell, V., and A. Bott, 2008: A hybrid convection scheme for use in non-hydrostatic numerical weather prediction models. *Meteor. Z.*, **17**, 775–783, <https://doi.org/10.1127/0941-2948/2008/0342>.
- , A. Gassmann, and A. Bott, 2007: Towards a new hybrid cumulus parametrization scheme for use in non-hydrostatic weather prediction models. *Quart. J. Roy. Meteor. Soc.*, **133**, 479–490, <https://doi.org/10.1002/qj.28>.
- Lander, J., and B. J. Hoskins, 1997: Believable scales and parametrizations in a spectral transform model. *Mon. Wea. Rev.*, **125**, 292–303, [https://doi.org/10.1175/1520-0493\(1997\)125<0292:BSAPIA>2.0.CO;2](https://doi.org/10.1175/1520-0493(1997)125<0292:BSAPIA>2.0.CO;2).
- Landu, K., L. R. Leung, S. Hagos, V. Vinoj, S. A. Rauscher, T. Ringler, and M. Taylor, 2014: The dependence of ITCZ structure on model resolution and dynamical core in aquaplanet simulations. *J. Climate*, **27**, 2375–2385, <https://doi.org/10.1175/JCLI-D-13-00269.1>.
- Large, W. G., 2006: Surface fluxes for practitioners of global ocean data assimilation. *Ocean Weather Forecasting: An Integrated View of Oceanography*, E. Chassignet and J. Verron, Eds., Springer, 229–270, [https://doi.org/10.1007/1-4020-4028-8\\_9](https://doi.org/10.1007/1-4020-4028-8_9).
- Lauritzen, P. H., J. T. Bacmeister, P. F. Callaghan, and M. A. Taylor, 2015a: NCAR\_Topo (v1.0): NCAR global model topography generation software for unstructured grids. *Geosci. Model Dev.*, **8**, 3975–3986, <https://doi.org/10.5194/gmd-8-3975-2015>.
- , A. J. Conley, J.-F. Lamarque, F. Vitt, and M. A. Taylor, 2015b: The terminator “toy” chemistry test: A simple tool to assess errors in transport schemes. *Geosci. Model Dev.*, **8**, 1299–1313, <https://doi.org/10.5194/gmd-8-1299-2015>.
- Lee, M.-I., I. Kang, and B. E. Mapes, 2003: Impacts of cumulus convection parameterization on aqua-planet AGCM simulations of tropical intraseasonal variability. *J. Meteor. Soc. Japan*, **81**, 963–992, <https://doi.org/10.2151/jmsj.81.963>.
- , M. J. Suarez, I.-S. Kang, I. M. Held, and D. Kim, 2008: A moist benchmark calculation for atmospheric general circulation models. *J. Climate*, **21**, 4934–4954, <https://doi.org/10.1175/2008JCLI1891.1>.
- Lemarié, F., L. Debreu, and E. Blayo, 2013: Toward an optimized global-in-time Schwarz algorithm for diffusion equations with discontinuous and spatially variable coefficients. Part 2: The variable coefficients case. *Electron. Trans. Numer. Anal.*, **40**, 170–186.
- , P. Marchesiello, L. Debreu, and E. Blayo, 2014: Sensitivity of ocean–atmosphere coupled models to the coupling method: Example of Tropical Cyclone Erica. INRIA Grenoble Research Rep. RR-8651, 32 pp., <https://hal.inria.fr/hal-00872496>.
- , E. Blayo, and L. Debreu, 2015: Analysis of ocean–atmosphere coupling algorithms: Consistency and stability. *Proc. Comput. Sci.*, **51**, 2066–2075, <https://doi.org/10.1016/j.procs.2015.05.473>.
- Li, F., W. Collins, M. Wehner, D. Williamson, J. Olson, and C. Algieri, 2011: Impact of horizontal resolution on simulation of precipitation extremes in an aqua-planet version of Community Atmospheric Model (CAM3). *Tellus*, **63A**, 884–892, <https://doi.org/10.1111/j.1600-0870.2011.00544.x>.
- Lin, S.-J., 2004: A “vertically Lagrangian” finite-volume dynamical core for global models. *Mon. Wea. Rev.*, **132**, 2293–2307, [https://doi.org/10.1175/1520-0493\(2004\)132<2293:AVLFDC>2.0.CO;2](https://doi.org/10.1175/1520-0493(2004)132<2293:AVLFDC>2.0.CO;2).
- Lock, A. P., A. R. Brown, M. R. Bush, G. M. Martin, and R. N. B. Smith, 2000: A new boundary layer mixing scheme. Part I: Scheme description and single-column model tests. *Mon. Wea. Rev.*, **128**, 3187–3199, [https://doi.org/10.1175/1520-0493\(2000\)128<3187:ANBLMS>2.0.CO;2](https://doi.org/10.1175/1520-0493(2000)128<3187:ANBLMS>2.0.CO;2).
- Ma, P.-L., P. J. Rasch, J. D. Fast, R. C. Easter, W. I. Gustafson Jr., X. Liu, S. J. Ghan, and B. Singh, 2014: Assessing the CAM5 physics suite in the WRF-Chem model: Implementation, resolution sensitivity, and a first evaluation for a regional case study. *Geosci. Model Dev.*, **7**, 755–778, <https://doi.org/10.5194/gmd-7-755-2014>.
- Malardel, S., and D. Ricard, 2015: An alternative cell-averaged departure point reconstruction for pointwise semi-Lagrangian transport schemes. *Quart. J. Roy. Meteor. Soc.*, **141**, 2114–2126, <https://doi.org/10.1002/qj.2509>.
- , and N. P. Wedi, 2016: How does subgrid-scale parametrization influence nonlinear spectral energy fluxes in global NWP models? *J. Geophys. Res. Atmos.*, **121**, 5395–5410, <https://doi.org/10.1002/2015JD023970>.
- Manabe, S., and K. Bryan, 1969: Climate calculations with a combined ocean–atmosphere model. *J. Atmos. Sci.*, **26**, 786–789, [https://doi.org/10.1175/1520-0469\(1969\)026<0786:CCWACO>2.0.CO;2](https://doi.org/10.1175/1520-0469(1969)026<0786:CCWACO>2.0.CO;2).
- McGregor, J. L., 2013: Recent developments in variable-resolution global climate modelling. *Climatic Change*, **129**, 369–380, <https://doi.org/10.1007/s10584-013-0866-5>.
- Medeiros, B., B. Stevens, and S. Bony, 2015: Using aquaplanets to understand the robust responses of comprehensive climate models to forcing. *Climate Dyn.*, **44**, 1957–1977, <https://doi.org/10.1007/s00382-014-2138-0>.
- , D. L. Williamson, and J. G. Olson, 2016: Reference aquaplanet climate in the Community Atmosphere Model, version 5. *J. Adv. Model. Earth Syst.*, **8**, 406–424, <https://doi.org/10.1002/2015MS000593>.
- Medvigy, D., R. L. Walko, M. J. Otte, and R. Avissar, 2010: The Ocean–Land–Atmosphere Model: Optimization and evaluation of simulated radiative fluxes and precipitation. *Mon. Wea. Rev.*, **138**, 1923–1939, <https://doi.org/10.1175/2009MWR3131.1>.
- , —, and R. Avissar, 2011: Effects of deforestation on spatiotemporal distributions of precipitation in South America. *J. Climate*, **24**, 2147–2163, <https://doi.org/10.1175/2010JCLI3882.1>.
- , —, M. J. Otte, and R. Avissar, 2013: Simulated changes in northwest U.S. climate in response to Amazon deforestation. *J. Climate*, **26**, 9115–9136, <https://doi.org/10.1175/JCLI-D-12-00775.1>.
- Mishra, S. K., and S. Sahany, 2011: Effects of time step size on the simulation of tropical climate in NCAR-CAM3. *Climate Dyn.*, **37**, 689–704, <https://doi.org/10.1007/s00382-011-0994-4>.
- , J. Srinivasan, and R. S. Nanjundiah, 2008: The impact of the time step on the intensity of ITCZ in an aquaplanet GCM. *Mon. Wea. Rev.*, **136**, 4077–4091, <https://doi.org/10.1175/2008MWR2478.1>.
- Möbis, B., and B. Stevens, 2012: Factors controlling the position of the intertropical convergence zone on an aquaplanet. *J. Adv. Model. Earth Syst.*, **4**, M00A04, <https://doi.org/10.1029/2012MS000199>.
- Morrison, H., and A. Gettelman, 2008: A new two-moment bulk stratiform cloud microphysics scheme in the Community Atmosphere Model, version 3 (CAM3). Part I: Description and numerical tests. *J. Climate*, **21**, 3642–3659, <https://doi.org/10.1175/2008JCLI2105.1>.

- Müller, A., 2014: Does high order and dynamic adaptive refinement improve the efficiency of atmospheric simulation? *Physics Dynamics Coupling in Geophysical Models—Bridging the Gap* (PDC14), Ensenada, Baja California, Mexico, CICESE, [http://pdc.cicese.mx/index\\_php/pdc14/](http://pdc.cicese.mx/index_php/pdc14/).
- Nair, R. D., H.-W. Choi, and H. Tufo, 2009: Computational aspects of a scalable high-order discontinuous Galerkin atmospheric dynamical core. *Comput. Fluids*, **38**, 309–319, <https://doi.org/10.1016/j.compfluid.2008.04.006>.
- , M. N. Levy, and P. H. Lauritzen, 2011: Emerging numerical methods for atmospheric modeling. *Numerical Techniques for Global Atmospheric Models*, P. Lauritzen et al., Eds., Lecture Notes in Computational Science and Engineering, Vol. 80, Springer, 251–311, [https://doi.org/10.1007/978-3-642-11640-7\\_9](https://doi.org/10.1007/978-3-642-11640-7_9).
- Neale, R. B., and B. J. Hoskins, 2000: A standard test for AGCMs including their physical parameterizations. I: The proposal. *Atmos. Sci. Lett.*, **1**, 101–107, <https://doi.org/10.1006/asle.2000.0022>.
- , and Coauthors, 2010a: Description of the NCAR Community Atmosphere Model (CAM 4.0). NCAR Tech. Note NCAR/TN-485+STR, 224 pp., [http://www.cesm.ucar.edu/models/ccsm4.0/cam/docs/description/cam4\\_desc.pdf](http://www.cesm.ucar.edu/models/ccsm4.0/cam/docs/description/cam4_desc.pdf).
- , and Coauthors, 2010b: Description of the NCAR Community Atmosphere Model (CAM 5.0). NCAR Tech. Note NCAR/TN-486+STR, 289 pp., [http://www.cesm.ucar.edu/models/ccsm1.0/cam/docs/description/cam5\\_desc.pdf](http://www.cesm.ucar.edu/models/ccsm1.0/cam/docs/description/cam5_desc.pdf).
- O'Brien, T. A., F. Li, W. D. Collins, S. A. Rauscher, T. D. Ringler, M. A. Taylor, S. M. Hagos, and R. L. Leung, 2013: Observed scaling in clouds and precipitation and scale incognizance in regional to global atmospheric models. *J. Climate*, **26**, 9313–9333, <https://doi.org/10.1175/JCLI-D-13-00005.1>.
- Palmer, T. N., A. Döring, and G. Seregin, 2014: The real butterfly effect. *Nonlinearity*, **27**, R123, <https://doi.org/10.1088/0951-7715/27/9/R123>.
- Park, S.-H., 2014: A unified convection scheme (UNICON). Part I: Formulation. *J. Atmos. Sci.*, **71**, 3902–3930, <https://doi.org/10.1175/JAS-D-13-0233.1>.
- , W. C. Skamarock, J. B. Klemp, L. D. Fowler, and M. G. Duda, 2013: Evaluation of global atmospheric solvers using extensions of the Jablonowski and Williamson baroclinic wave test case. *Mon. Wea. Rev.*, **141**, 3116–3129, <https://doi.org/10.1175/MWR-D-12-00096.1>.
- , J. B. Klemp, and W. C. Skamarock, 2014: A comparison of mesh refinement in the global MPAS-A and WRF Models using an idealized normal-mode baroclinic wave simulation. *Mon. Wea. Rev.*, **142**, 3614–3634, <https://doi.org/10.1175/MWR-D-14-00004.1>.
- Pauluis, O., and I. M. Held, 2002: Entropy budget of an atmosphere in radiative–convective equilibrium. Part I: Maximum work and frictional dissipation. *J. Atmos. Sci.*, **59**, 125–139, [https://doi.org/10.1175/1520-0469\(2002\)059<0125:EBOAAI>2.0.CO;2](https://doi.org/10.1175/1520-0469(2002)059<0125:EBOAAI>2.0.CO;2).
- Pincus, R., H. W. Barker, and J.-J. Morcrette, 2003: A fast, flexible, approximate technique for computing radiative transfer in inhomogeneous cloud fields. *J. Geophys. Res.*, **108**, 4376, <https://doi.org/10.1029/2002JD003322>.
- Piriou, J.-M., J.-L. Redelsperger, J.-F. Geleyn, J.-P. Lafore, and F. Guichard, 2007: An approach for convective parameterization with memory: Separating microphysics and transport in grid-scale equations. *J. Atmos. Sci.*, **64**, 4127–4139, <https://doi.org/10.1175/2007JAS2144.1>.
- Polcher, J., and Coauthors, 1998: A proposal for a general interface between land surface schemes and general circulation models. *Global Planet. Change*, **19**, 261–276, [https://doi.org/10.1016/S0921-8181\(98\)00052-6](https://doi.org/10.1016/S0921-8181(98)00052-6).
- Rajendran, K., A. Kitoh, and J. Srinivasan, 2013: Effect of SST variation on ITCZ in APE simulations. *J. Meteor. Soc. Japan*, **91A**, 195–215, <https://doi.org/10.2151/jmsj.2013-A06>.
- Rauscher, S. A., T. D. Ringler, W. C. Skamarock, and A. A. Mirin, 2013: Exploring a global multiresolution modeling approach using aquaplanet simulations. *J. Climate*, **26**, 2432–2452, <https://doi.org/10.1175/JCLI-D-12-00154.1>.
- Reed, K. A., and C. Jablonowski, 2012: Idealized tropical cyclone simulations of intermediate complexity: A test case for AGCMs. *J. Adv. Model. Earth Syst.*, **4**, M04001, <https://doi.org/10.1029/2011MS000099>.
- , —, and M. A. Taylor, 2012: Tropical cyclones in the spectral element configuration of the Community Atmosphere Model. *Atmos. Sci. Lett.*, **13**, 303–310, <https://doi.org/10.1002/asl.399>.
- Rhoades, A., X. Huang, P. Ullrich, and C. M. Zarzycki, 2016: Characterizing Sierra Nevada snowpack using variable-resolution CEM. *J. Appl. Meteor. Climatol.*, **55**, 173–196, <https://doi.org/10.1175/JAMC-D-15-0156.1>.
- Ringler, T. D., J. Thuburn, J. Klemp, and W. Skamarock, 2010: A unified approach to energy conservation and potential vorticity dynamics for arbitrarily-structured C-grids. *J. Comput. Phys.*, **229**, 3065–3090, <https://doi.org/10.1016/j.jcp.2009.12.007>.
- , D. Jacobsen, M. Gunzburger, L. Ju, M. Duda, and W. Skamarock, 2011: Exploring a multiresolution modeling approach within the shallow-water equations. *Mon. Wea. Rev.*, **139**, 3348–3368, <https://doi.org/10.1175/MWR-D-10-05049.1>.
- Roeckner, E., and Coauthors, 2003: The atmospheric general circulation model ECHAM5. Part I: Model description. Max Planck Institute for Meteorology Tech. Rep. 349, 140 pp., [https://www.mpimet.mpg.de/fileadmin/publikationen/Reports/max\\_scirep\\_349.pdf](https://www.mpimet.mpg.de/fileadmin/publikationen/Reports/max_scirep_349.pdf).
- , and Coauthors, 2006: Sensitivity of simulated climate to horizontal and vertical resolution in the ECHAM5 atmosphere model. *J. Climate*, **19**, 3771–3791, <https://doi.org/10.1175/JCLI3824.1>.
- Romps, D. M., 2008: The dry-entropy budget of a moist atmosphere. *J. Atmos. Sci.*, **65**, 3779–3799, <https://doi.org/10.1175/2008JAS2679.1>.
- Rotunno, R., and C. Snyder, 2008: A generalization of Lorenz's model for the predictability of flows with many scales of motion. *J. Atmos. Sci.*, **65**, 1063–1076, <https://doi.org/10.1175/2007JAS2449.1>.
- Russell, G. L., J. R. Miller, and D. Rind, 1995: A coupled atmosphere–ocean model for transient climate change studies. *Atmos.–Ocean*, **33**, 683–730, <https://doi.org/10.1080/07055900.1995.9649550>.
- Ryder, J., and Coauthors, 2016: A multi-layer land surface energy budget model for implicit coupling with global atmospheric simulations. *Geosci. Model Dev.*, **9**, 223–245, <https://doi.org/10.5194/gmd-9-223-2016>.
- Sakaguchi, K., and Coauthors, 2015: Exploring a multiresolution approach using AMIP simulations. *J. Climate*, **28**, 5549–5574, <https://doi.org/10.1175/JCLI-D-14-00729.1>.
- , J. Lu, L. R. Leung, C. Zhao, Y. Li, and S. Hagos, 2016: Sources and pathways of the upscale effects on the Southern Hemisphere jet in MPAS-CAM4 variable-resolution simulations. *J. Adv. Model. Earth Syst.*, **8**, 1786–1805, <https://doi.org/10.1002/2016MS000743>.
- Schluter, J. U., and H. Pitsch, 2005: Antialiasing filters for coupled Reynolds-averaged/large-eddy simulations. *AIAA J.*, **43**, 608–615, <https://doi.org/10.2514/1.4439>.
- Schmidt, F., 1977: Variable fine mesh in the spectral global models. *Beitr. Phys. Atmos.*, **50**, 211–217.

- Schmidt, G. A., C. M. Bitz, U. Mikolajewicz, and L.-B. Tremblay, 2004: Ice–ocean boundary conditions for coupled models. *Ocean Modell.*, **7**, 59–74, [https://doi.org/10.1016/S1463-5003\(03\)00030-1](https://doi.org/10.1016/S1463-5003(03)00030-1).
- Schulz, J.-P., L. Dümenil, and J. Polcher, 2001: On the land surface–atmosphere coupling and its impact in a single-column atmospheric model. *J. Appl. Meteor.*, **40**, 642–663, [https://doi.org/10.1175/1520-0450\(2001\)040<0642:OTLSAC>2.0.CO;2](https://doi.org/10.1175/1520-0450(2001)040<0642:OTLSAC>2.0.CO;2).
- Schwarz, H. A., 1870: Über einen grenzübergang durch alternierendes verfahren. *Vierteljahrsschrift Naturforschende Gesellschaft in Zürich*, **15** (3), 272–286.
- Siebesma, A. P., 2015: First workshop of the Grey Zone Project. *GEWEX News*, Vol. 25, No. 1, International GEWEX Project Office, Silver Spring, MD, 7–9.
- , P. M. M. Soares, and J. Teixeira, 2007: A combined eddy-diffusivity mass-flux approach for the convective boundary layer. *J. Atmos. Sci.*, **64**, 1230–1248, <https://doi.org/10.1175/JAS3888.1>.
- Skamarock, W. C., 2011: Kinetic energy spectra and model filters. *Numerical Techniques for Global Atmospheric Models*, P. Lauritzen et al., Eds., Lecture Notes in Computational Science and Engineering, Vol. 80, Springer, 495–512, [https://doi.org/10.1007/978-3-642-11640-7\\_14](https://doi.org/10.1007/978-3-642-11640-7_14).
- Small, R. J., and Coauthors, 2014: A new synoptic scale resolving global climate simulation using the Community Earth System Model. *J. Adv. Model. Earth Syst.*, **6**, 1065–1094, <https://doi.org/10.1002/2014MS000363>.
- Smith, G. C., and Coauthors, 2018: Impact of coupling with an ice–ocean model on global medium-range NWP forecast skill. *Mon. Wea. Rev.*, **146**, 1157–1180, <https://doi.org/10.1175/MWR-D-17-0157.1>.
- Smith, R. N. B., 1990: A scheme for predicting layer clouds and their water content in a general circulation model. *Quart. J. Roy. Meteor. Soc.*, **116**, 435–460, <https://doi.org/10.1002/qj.49711649210>.
- Staniforth, A. N., and H. L. Mitchell, 1978: A variable-resolution finite-element technique for regional forecasting with the primitive equations. *Mon. Wea. Rev.*, **106**, 439–447, [https://doi.org/10.1175/1520-0493\(1978\)106<0439:AVRFET>2.0.CO;2](https://doi.org/10.1175/1520-0493(1978)106<0439:AVRFET>2.0.CO;2).
- , and J. Thuburn, 2012: Horizontal grids for global weather and climate prediction models: A review. *Quart. J. Roy. Meteor. Soc.*, **138**, 1–26, <https://doi.org/10.1002/qj.958>.
- Sun, S., and J. E. Hansen, 2003: Climate simulations for 1951–2050 with a coupled atmosphere–ocean model. *J. Climate*, **16**, 2807–2826, [https://doi.org/10.1175/1520-0442\(2003\)016<2807:CSFWAC>2.0.CO;2](https://doi.org/10.1175/1520-0442(2003)016<2807:CSFWAC>2.0.CO;2).
- Taylor, M. A., and A. Fournier, 2010: A compatible and conservative spectral element method on unstructured grids. *J. Comput. Phys.*, **229**, 5879–5895, <https://doi.org/10.1016/j.jcp.2010.04.008>.
- , J. Edwards, and A. St. Cyr, 2008: Petascale atmospheric models for the community climate system model: New developments and evaluation of scalable dynamical cores. *J. Phys. Conf. Ser.*, **125**, 012023, <https://doi.org/10.1088/1742-6596/125/1/012023>.
- Teixeira, J., C. A. Reynolds, and K. Judd, 2007: Time step sensitivity of nonlinear atmospheric models: Numerical convergence, truncation error growth, and ensemble design. *J. Atmos. Sci.*, **64**, 175–189, <https://doi.org/10.1175/JAS3824.1>.
- Termonia, P., and Coauthors, 2018: The ALADIN system and its canonical model configurations AROME CY41T1 and ALARO CY40T1. *Geosci. Model Dev.*, **11**, 257–281, <https://doi.org/10.5194/gmd-11-257-2018>.
- Thatcher, D. R., and C. Jablonowski, 2016: A moist aquaplanet variant of the Held–Suarez test for atmospheric model dynamical cores. *Geosci. Model Dev.*, **9**, 1263–1292, <https://doi.org/10.5194/gmd-9-1263-2016>.
- Thayer-Calder, K., and Coauthors, 2015: A unified parameterization of clouds and turbulence using CLUBB and subcolumns in the Community Atmosphere Model. *Geosci. Model Dev.*, **8**, 3801–3821, <https://doi.org/10.5194/gmd-8-3801-2015>.
- Tomita, H., M. Satoh, and K. Goto, 2002: An optimization of the icosahedral grid modified by spring dynamics. *J. Comput. Phys.*, **183**, 307–331, <https://doi.org/10.1006/jcph.2002.7193>.
- Uchida, J., M. Mori, H. Nakamura, M. Satoh, K. Suzuki, and T. Nakajima, 2016: Error and energy budget analysis of a nonhydrostatic stretched-grid global atmospheric model. *Mon. Wea. Rev.*, **144**, 1423–1447, <https://doi.org/10.1175/MWR-D-15-0271.1>.
- Ullrich, P. A., and C. Jablonowski, 2011: An analysis of 1D finite-volume methods for geophysical problems on refined grids. *J. Comput. Phys.*, **230**, 706–725, <https://doi.org/10.1016/j.jcp.2010.10.014>.
- , and M. A. Taylor, 2015: Arbitrary-order conservative and consistent remapping and a theory of linear maps: Part I. *Mon. Wea. Rev.*, **143**, 2419–2440, <https://doi.org/10.1175/MWR-D-14-00343.1>.
- Valcke, S., and Coauthors, 2012: Coupling technologies for Earth system modelling. *Geosci. Model Dev.*, **5**, 1589–1596, <https://doi.org/10.5194/gmd-5-1589-2012>.
- Wacker, U., and F. Herbert, 2003: Continuity equations as expressions for local balances of masses in cloudy air. *Tellus*, **55A**, 247–254, <https://doi.org/10.3402/tellusa.v55i3.12097>.
- , T. Frisius, and F. Herbert, 2006: Evaporation and precipitation surface effects in local mass continuity laws of moist air. *J. Atmos. Sci.*, **63**, 2642–2652, <https://doi.org/10.1175/JAS3754.1>.
- Walko, R. L., and R. Avissar, 2011: A direct method for constructing refined regions in unstructured conforming triangular–hexagonal computational grids: Application to OLAM. *Mon. Wea. Rev.*, **139**, 3923–3937, <https://doi.org/10.1175/MWR-D-11-00021.1>.
- Wan, H., P. J. Rasch, K. Zhang, J. Kazil, and L. R. Leung, 2013: Numerical issues associated with compensating and competing processes in climate models: An example from ECHAM-HAM. *Geosci. Model Dev.*, **6**, 861–874, <https://doi.org/10.5194/gmd-6-861-2013>.
- , —, —, Y. Qian, H. Yan, and C. Zhao, 2014: Short ensembles: An efficient method for discerning climate-relevant sensitivities in atmospheric general circulation models. *Geosci. Model Dev.*, **7**, 1961–1977, <https://doi.org/10.5194/gmd-7-1961-2014>.
- , —, M. A. Taylor, and C. Jablonowski, 2015: Short-term time step convergence in a climate model. *J. Adv. Model. Earth Syst.*, **7**, 215–225, <https://doi.org/10.1002/2014MS000368>.
- Wang, Y., L. R. Leung, J. L. McGregor, D.-K. Lee, W.-C. Wang, Y. Ding, and F. Kimura, 2004: Regional climate modeling: Progress, challenges, and prospects. *J. Meteor. Soc. Japan*, **82**, 1599–1628, <https://doi.org/10.2151/jmsj.82.1599>.
- Wedi, N., 1999: The numerical coupling of the physical parameterizations to the “dynamical” equations in a forecast model. ECMWF Tech. Memo. 274, 37 pp., <https://www.ecmwf.int/sites/default/files/elibrary/1999/13020-numerical-coupling-physical-parametrizations-dynamical-equations-forecast-model.pdf>.
- Williamson, D. L., 2002: Time-split versus process-split coupling of parameterizations and dynamical core. *Mon. Wea. Rev.*, **130**, 2024–2041, [https://doi.org/10.1175/1520-0493\(2002\)130<2024:TSVPSC>2.0.CO;2](https://doi.org/10.1175/1520-0493(2002)130<2024:TSVPSC>2.0.CO;2).
- , 2007: The evolution of dynamical cores for global atmospheric models. *J. Meteor. Soc. Japan*, **85B**, 241–269, <https://doi.org/10.2151/jmsj.85B.241>.
- , 2008: Convergence of aqua-planet simulations with increasing resolution in the Community Atmospheric Model,

- version 3. *Tellus*, **60A**, 848–862, <https://doi.org/10.1111/j.1600-0870.2008.00339.x>.
- , 2013: The effect of time steps and time-scales on parametrization suites. *Quart. J. Roy. Meteor. Soc.*, **139**, 548–560, <https://doi.org/10.1002/qj.1992>.
- , and J. G. Olson, 2003: Dependence of aqua-planet simulations on time step. *Quart. J. Roy. Meteor. Soc.*, **129**, 2049–2064, <https://doi.org/10.1256/qj.02.62>.
- Wood, N., M. Diamantakis, and A. Staniforth, 2007: A monotonically-damping second-order accurate unconditionally stable numerical scheme for diffusion. *Quart. J. Roy. Meteor. Soc.*, **133**, 1559–1573, <https://doi.org/10.1002/qj.116>.
- Wyngaard, J. C., 2004: Toward numerical modeling in the “terra incognita.” *J. Atmos. Sci.*, **61**, 1816–1826, [https://doi.org/10.1175/1520-0469\(2004\)061<1816:TNMITT>2.0.CO;2](https://doi.org/10.1175/1520-0469(2004)061<1816:TNMITT>2.0.CO;2).
- Xu, K.-M., and D. A. Randall, 1996: A semiempirical cloudiness parameterization for use in climate models. *J. Atmos. Sci.*, **53**, 3084–3102, [https://doi.org/10.1175/1520-0469\(1996\)053<3084:ASCPFU>2.0.CO;2](https://doi.org/10.1175/1520-0469(1996)053<3084:ASCPFU>2.0.CO;2).
- Zarzycki, C. M., and C. Jablonowski, 2014: A multidecadal simulation of Atlantic tropical cyclones using a variable-resolution global atmospheric general circulation model. *J. Adv. Model. Earth Syst.*, **6**, 805–828, <https://doi.org/10.1002/2014MS000352>.
- , and —, 2015: Experimental tropical cyclone forecasts using a variable-resolution global model. *Mon. Wea. Rev.*, **143**, 4012–4037, <https://doi.org/10.1175/MWR-D-15-0159.1>.
- , —, and M. A. Taylor, 2014a: Using variable-resolution meshes to model tropical cyclones in the Community Atmosphere Model. *Mon. Wea. Rev.*, **142**, 1221–1239, <https://doi.org/10.1175/MWR-D-13-00179.1>.
- , M. N. Levy, C. Jablonowski, J. R. Overfelt, M. A. Taylor, and P. A. Ullrich, 2014b: Aquaplanet experiments using CAM’s variable-resolution dynamical core. *J. Climate*, **27**, 5481–5503, <https://doi.org/10.1175/JCLI-D-14-00004.1>.
- , C. Jablonowski, D. R. Thatcher, and M. A. Taylor, 2015: Effects of localized grid refinement on the general circulation and climatology in the Community Atmosphere Model. *J. Climate*, **28**, 2777–2803, <https://doi.org/10.1175/JCLI-D-14-00599.1>.
- , and Coauthors, 2018: DCMIP2016: The splitting supercell test case. *Geosci. Model Dev. Discuss.*, <https://doi.org/10.5194/gmd-2018-156>, in press.
- Zdunkowski, W., and A. Bott, 2003: *Dynamics of the Atmosphere: A Course in Theoretical Meteorology*. Cambridge University Press, 719 pp.
- , and —, 2004: *Thermodynamics of the Atmosphere*. Cambridge University Press, 266 pp.
- Zhang, G. J., and N. A. McFarlane, 1995: Sensitivity of climate simulations to the parameterization of cumulus convection in the Canadian Climate Centre general circulation model. *Atmos.–Ocean*, **33**, 407–446, <https://doi.org/10.1080/07055900.1995.9649539>.
- Zhang, K., and Coauthors, 2012: The global aerosol-climate model ECHAM-HAM, version 2: Sensitivity to improvements in process representations. *Atmos. Chem. Phys.*, **12**, 8911–8949, <https://doi.org/10.5194/acp-12-8911-2012>.
- Zhang, R., and T. L. Delworth, 2005: Simulated tropical response to a substantial weakening of the Atlantic thermohaline circulation. *J. Climate*, **18**, 1853–1860, <https://doi.org/10.1175/JCLI3460.1>.
- Zhao, C., and Coauthors, 2016: Exploring the impacts of physics and resolution on aqua-planet simulations from a non-hydrostatic global variable-resolution modeling framework. *J. Adv. Model. Earth Syst.*, **8**, 1751–1768, <https://doi.org/10.1002/2016MS000727>.